Compression-sensitive Magnetic Resonance Elastography

Dissertation

zur Erlangung des akademischen Grades

doctor rerum naturalium
(Dr. rer. nat.)

im Fach Physik
eingereicht an der

Mathematisch-Naturwissenschaftlichen Fakultät
an der Humboldt-Universität zu Berlin

von Dipl.-Phys. Sebastian Hirsch

Präsident der Humboldt-Universität zu Berlin
Prof. Dr. Jan-Hendrik Olbertz

Dekan der Mathematisch-Naturwissenschaftlichen Fakultät
Prof. Dr. Elmar Kulke

Gutachter/innen:
1. Prof. Dr. rer. nat. Norbert Koch
2. Prof. Dr. rer. nat. Ingolf Sack
3. Prof. Dr. rer. nat. Dr. med. Johannes Bernarding

Datum der mündlichen Prüfung: 30. April 2015

Zusammenfassung

Diese Arbeit stellt das Konzept der *kompressionssensitiven Magnetresonanzelastographie* vor. Konventionelle Magnetresonanzelastographie (MRE) regt mechanische Scherwellen im menschlichen Körper an und detektiert diese mit Hilfe der Magnetresonanztomographie (MRT). Anhand dieser Daten kann der Schermodul von Organen bestimmt werden, wodurch eine nichtinvasive Diagnose bestimmter Erkrankungen ermöglicht wird.

Im Gegensatz dazu analysiert die kompressionssensitive MRE die Ausbreitung von Kompressionswellen und liefert dadurch Erkenntnisse über die Kompressionseigenschaften eines Mediums. Forschungsergebnisse aus den letzten Jahren legen nahe, dass eine poroelastische Theorie eine bessere Beschreibung für das Deformationsverhalten von organischem Gewebe darstellt als das der konventionellen MRE zugrunde liegende einphasige viskoelastische Modell. In einem poroelastischen System kann Kompressibilität durch Interaktion der einzelnen Phasen entstehen, auch wenn jede Phase für sich inkompressibel ist.

Anomalien bei der Regulation des hydrostatischen Gewebedrucks stehen in Zusammenhang mit verschiedenen Krankheitsbildern, wie beispielsweise Normaldruck-Hydrozephalus und Pfortader-Hypertonie. Statischer Druck spielt als sogenannter Porendruck eine zentrale Rolle in den poroelastischen Gleichungen für die Druckwellenpropagation; die kompressionssensitive MRE könnte daher ein nichtinvasives Diagnoseinstrument darstellen, das die durch konventionelle Scherwellen-Elastographie gewonnenen Informationen um weitere Aspekte ergänzt.

Diese Arbeit beschreibt die Entwicklung einer schnellen Singleshot-EPI-Bildgebungssequenz, mit deren Hilfe die volumetrische Verzerrung (Ausdehnung oder Kompression) quantifiziert werden kann, die durch propagierende Druckwellen hervorgerufen wird. Die Validierung der kompressionssensitiven MRE erfolgte an verschiedenen Systemen: an porösen Gelphantomen mit gasgefüllten Einschlüssen, an der menschlichen Lunge in zwei Atemzuständen, in einer ex-vivo Schafsleber bei unterschiedlichen hydrostatischen Drücken und schließlich am menschlichen Gehirn. Die extern induzierte oszillierende volumetrische Verzerrung konnte sowohl in den Phantomen als auch in menschlichen Organen quantifiziert werden. Die Ergebnisse belegen, dass die Stärke der induzierten volumetrischen Verzerrung sensitiv gegenüber Druckänderungen zwischen verschiedenen physiologischen Zuständen ist, wohingegen die Scherverzerrung keine derartige Abhängigkeit aufweist. In einer weiteren Studie wurde die durch den Herzzyklus angetriebene Pulsation des menschlichen Hirns anstelle einer externen Vibrationsquelle ausgenutzt. Die Geschwindigkeit der lokalen Volumenänderung wurde über den Pulsationszyklus verfolgt. Dabei erzeugte die arterielle Pulswelle eine kurze lokale Expansion des Hirnparenchyms; in der sich anschließenden diastolischen Phase erfolgte eine langsame Rückkehr zum Ausgangszustand.

Aus den gemessenen volumetrischen Verzerrungen wurden durch Inversion der Druckwellengleichung numerische Werte für den *Druckwellenmodul M* berechnet; Rauschen wurde als primäre Ursache für die systematische Unterschätzung von M identifiziert.

Schlagwörter: Magnetresonanzelastographie, MRE, Poroelastizität, Gewebedruck, Kompressionsmodul.

Abstract

This thesis introduces the concept of *compression-sensitive Magnetic Resonance Elastography*. Conventional Magnetic Resonance Elastography (MRE) creates shear waves in the human body and captures magnetic resonance images of their propagation that are used to estimate the shear modulus ("stiffness") of organs, aiding in the diagnosis of certain diseases.

Compression-sensitive MRE, on the other hand, detects the propagation of pressure waves, providing insight into the compressibility of a material. Recent research has suggested that a poroelastic theory might be a more appropriate description of organic tissue than the conventional monophasic viscoelastic model. Poroelastic models incorporate compressibility through interaction of compartments, even as each individual compartment remains incompressible.

Hydrostatic tissue pressure abnormalities have been found to be associated with a number of diseases, such as normal pressure hydrocephalus or hepatic portal hypertension. Since pore pressure plays a central role in the poroelastic equations governing the propagation of pressure waves, compression-sensitive MRE could potentially serve as a diagnostic tool, providing information complimentary to shear-wave MRE data.

This thesis describes the development of a fast single-shot EPI MR sequence capable of quantifying volumetric strain induced by external vibrations. Compression-sensitive MRE was validated in porous gel phantoms containing gas-filled cavities, in the human lung at two different respiratory states, in an ex vivo sheep liver at varying levels of hydrostatic pressure, and finally in human liver and brain. Results illustrate that compression-sensitive MRE is capable of quantifying volumetric strain in phantoms and in human organs. It was found that volumetric strain was sensitive toward pressure changes associated with different physiological states, whereas shear strain remained constant.

In an additional study, pulsation of the human brain, driven by the heart cycle, was used as the actuation source instead of the external vibration generator. Volumetric strain velocity was tracked over the cardiac cycle. Results indicate local expansion of brain parenchyma upon the arrival of the arterial pulse wave, followed by a slow return to the initial state during the diastolic phase.

Numerical values for the *pressure wave modulus M* were calculated from measured volumetric strain through inversion of the pressure wave equation. Measurement noise was identified as the primary effect causing a severe underestimation of M.

Keywords: Magnetic Resonance Elastography, MRE, poroelasticity, tissue pressure, bulk modulus, compression modulus.

Acknowledgements

First and foremost I would like to thank Prof. Ingolf Sack, head of the MRE group at the Charité in Berlin, who invested his time and resources to supervise and mentor my thesis. He enabled my research and provided uncountable valuable insights and suggestions. He was always open to my proposals, and without the constant discussions and brainstorming, this thesis would definitely not exist in its current form. I would also like to thank him for giving me the freedom to pursue my own ideas, and for his trust in my skills as a scientist.

I am very grateful to Prof. Norbert Koch for accepting me as an external PhD student, for his time, his helpfulness and his continuous support. I really appreciate his help, which made many things much easier.

I am deeply grateful to many people who have contributed to the research presented in this thesis or provided guidance and advice. When I started my work at the MRE group at the Charité, I found highly motivated people who had already established a very broad theoretical and practical foundation on which I could base my own work. They all shared their specific knowledge with me, greatly helping me to understand the different aspects of MR Elastography and their complex interrelations. For that I would like to thank Jürgen Braun, Sebastian Papazoglou, Dieter Klatt, Marian Schwarz and Thomas Elgeti.

Many new colleagues have joined the group since I started my work, and some have left in the meantime. Inspiring discussions with colleagues have always been an integral part of everyday work, and I have oftentimes benefited from their comments, ideas and experience. In addition to the aforementioned persons, I would also like to thank Jing Guo, Andreas Fehlner, Heiko Tzschätzsch, Oleg Posnansky, Kaspar-Josche Streitberger, Rolf Reiter, Selcan Ipek and Florian Dittmann.

Frauke Beyer performed research regarding the production of gel phantoms with gas-filled inclusions. Her findings were the foundation of the IGC phantom study, and I

worked with her on all phantom experiments. I would like to thank her for that and for the many fruitful discussions we had, which hugely helped advance my understanding of the theoretical aspects behind the experiments.

Furthermore I would like to thank Alfonso Caiazzo from the Weierstraß-Institut in Berlin and Joaquín Mura from the Civil Engineering School at Pontificia Universidad Católica de Valparaíso in Chile for fruitful discussions about the theoretical foundations of compressible media.

Daniel Brenner and Rüdiger Stirnberg from Deutsches Zentrum für Neurodegenerative Erkrankungen patiently answered many of my questions regarding sequence programming and shared their knowledge with me. Thank you very much!

I cordially thank Joanna Gubman and Eleanor Berryman for proof-reading this thesis and providing valuable comments and suggestions for improvements.

Zu guter Letzt danke ich ganz herzlich meinen Eltern und meinen Brüdern für ihre bedingungslose Unterstützung aus der Ferne, ihre Liebe, ihren Rat und ihren Glauben an mich. Danke!

Contents

1 Introduction

Manual palpation has been used throughout human history as a means of detecting changes in tissue compliance, which can be a cause or a symptom of disease. Easily accessible organs such as the liver, the breast, and many muscles can be readily palpated by experienced physicians to detect abnormalities. Deeper-lying organs, on the other hand, or those shielded by bones, such as the brain, are inaccessible to manual palpation. Furthermore, palpation relies on the experience of the examiner and cannot provide quantitative values for transversal studies (comparisons between different individuals) or longitudinal studies (repeated examinations of the same subject at different times).

Quantitative imaging of tissue stiffness, using ultrasound as the imaging modality and externally stimulated vibrations to provide an elasticity-based image contrast, was pioneered by Lerner and Parker et al. [50, 67] and Ophir el al. [64]. Magnetic Resonance Elastography (MRE) was introduced in 1995 by Muthupillai et al [63] and Plewes et al. [73], and has since evolved into a mature imaging tool that addresses the deficiencies of manual palpation, permitting clinicians and researchers to measure and map visco-elastic properties of in vivo tissue non-invasively.

MRE deploys Magnetic Resonance Imaging (MRI) to detect the propagation of externally stimulated mechanical waves through the body. Mathematical processing of *wave images* allows one to characterize the elastic and viscous properties of tissue. The mechanical response of tissue can be modeled in different ways and at varying complexity. Every model is associated with a set of wave equations for the three Cartesian components of the oscillation field. The acquired data can be used to solve these wave equations, typically either algebraically through direct inversion, or in an iterative procedure based on a finite element model. The solution of the wave equations yields numerical values for viscoelastic parameters, such as the shear modulus and the viscosity.

Today, MRE has reached clinical relevance, with non-invasive diagnosis and staging of liver fibrosis being the most established application [37]. Further applications include prostate [39], female breast [53], brain [21, 32, 44, 60, 100], kidney [82], muscle [14, 65] and additional preclinical research on animal models.

To date, most applications of MRE were based on the assumption that biological tissue, due to its high water content, is incompressible within the precision achievable by MRE. Hence, only the shear component of the wave field was studied, whereas the compression component was considered negligible or indistinguishable from noise. However, the theory of *poroelasticity*, originally developed by Maurice Biot [6] to model the behavior of porous rocks or soil under load, predicts finite compression moduli for biphasic media under certain circumstances, even if all constituents themselves are incompressible. Application of such a model to organic tissue has been suggested [43, 49] and its feasibility was shown in tofu phantoms [4, 5, 43].

One central quantity in poroelasticity is pore pressure. Pressure anomalies can be cause or symptom of a number of diseases, such as hydrocephalus, idiopathic intracranial hypertension or hepatic portal hypertension. Currently, pressure measurements are only possible in an invasive manner, imposing discomfort and risk of complication upon the patient. A non-invasive pressure quantification method would therefore constitute a major benefit. Pressure is not directly observable by MRE; however, poroelastography relates pore pressure to the compressibility of a biphasic material. Quantification of volumetric strain induced by external forces might therefore provide a foundation on which a pressure-sensitive imaging methodology can be built.

The development of compression-sensitive MRE is the goal of this work. Interpreting compression-sensitive MRE-derived data within a poroelastic framework requires measurement of the three-dimensional displacement field induced by external mechanical vibrations at discrete locations (voxels) within a three-dimensional volume of interest. Existing data acquisition strategies used in MRE were not fast enough to perform examinations within time frames acceptable for in vivo applications. Hence, a new MRE sequence, based on the echo-planar imaging (EPI) principle, was developed as part of this work. The new technique was then employed in a number of experiments to assess the suitability of oscillating volumetric strain (e.g. local compression or dilatation) as an indicator of pressure alterations.

The scientific background of MR imaging and elasticity theory is presented in chapter 2. The technical developments that constitute the foundation for the research presented in this thesis are described in chapter 3.

Since different experiments were conducted to investigate various aspects of this new imaging modality, they will be presented separately in chapter 4. For some studies, additional theoretical background is presented, which is considered too specific to be included in the general theory chapter. Each experiment has its own discussion section. A comprehensive discussion combining the results of all studies will be presented in chapter 5.

2 Theory

2.1 Magnetic Resonance Imaging

2.1.1 Protons in a magnetic field

Magnetic resonance imaging (MRI) is based on the manipulation of the magnetic moments of hydrogen nuclei (protons) in a strong magnetic field. A static magnetic field $\mathbf{B}_0$, typically with a field strength of 1.5 or 3 Tesla in clinical MRI scanners, induces a macroscopic magnetization in the proton population inside a given object. Microscopically, $\mathbf{B}_0$ defines a quantization axis for the proton spin $\mathbf{S}$. For all following considerations, we assume that $\mathbf{B}_0$ is aligned with the z-axis of the coordinate system: $\mathbf{B}_0 = (0,0,B_0)^{\mathrm{T}}$. The proton has a spin quantum number $S = \frac{1}{2}$, meaning that $|\mathbf{S}| = \sqrt{S(S+1)}\hbar = \sqrt{\frac{3}{4}}\hbar$. The projection of $\mathbf{S}$ onto $\mathbf{B}_0$ can assume one of two possible values, $S_z = \pm\frac{1}{2}\hbar$, whereas the x- and y-components of the spin, S_x and S_y, according to the quantum mechanical uncertainty principle, remain undetermined. The proton spin is associated with a magnetic moment

$$\boldsymbol{\mu} = \gamma \mathbf{S} \tag{2.1}$$

with the *gyromagnetic ratio* $\gamma = 2\pi \cdot 42.58\,\mathrm{MHz/T}$ for protons [31]. Thus, the z-component of the magnetic moment can assume values

$$\mu_z = \pm\frac{1}{2}\gamma\hbar \tag{2.2}$$

while μ_x and μ_y form an arbitrary and undetermined transverse magnetization component in the xy-plane. For each of the two possible values of μ_z, the potential energy of the respective state is

$$E = -B_0 \cdot \mu_z, \tag{2.3}$$

indicating that the parallel alignment ($\uparrow\uparrow$) of μ_z with $\mathbf{B}_0$ has lower energy than the anti-parallel ($\uparrow\downarrow$) orientation [52]. The energy gap between the two states is there-

fore

$$\Delta E = E_{\uparrow\downarrow} - E_{\uparrow\uparrow} = 2 \cdot B_0 \cdot \mu_z = \gamma \cdot B_0 \cdot \hbar. \tag{2.4}$$

The distribution of the entire population of N protons over these two states is then governed by a Fermi statistics [33]:

$$N_{\uparrow\uparrow} = N \cdot \frac{e^{-E_{\uparrow\uparrow}/k_B T}}{e^{-E_{\uparrow\uparrow}/k_B T} + e^{-E_{\uparrow\downarrow}/k_B T}} \tag{2.5}$$

$$N_{\uparrow\downarrow} = N \cdot \frac{e^{-E_{\uparrow\downarrow}/k_B T}}{e^{-E_{\uparrow\uparrow}/k_B T} + e^{-E_{\uparrow\downarrow}/k_B T}} \tag{2.6}$$

The magnetic moments of protons in the parallel and antiparallel state cancel each other out. However, at human body temperature of 37°C, the parallel, lower energy state has a slightly larger population than the excited anti-parallel state. The excess population, with respect to the total population,

$$\Delta N = \frac{N_{\uparrow\uparrow} - N_{\uparrow\downarrow}}{N} = \frac{e^{-E_{\uparrow\uparrow}/k_B T} - e^{-E_{\uparrow\downarrow}/k_B T}}{e^{-E_{\uparrow\uparrow}/k_B T} + e^{-E_{\uparrow\downarrow}/k_B T}} \tag{2.7}$$

is in the order of 10^{-6} at typical field strengths of clinical MRI scanners of 1.5 T or 3 T. This effect causes a small net magnetization

$$\mathbf{M}_0 = \Delta N \rho |\mu_z| \hat{\mathbf{z}} \tag{2.8}$$

with the average proton density ρ and the unit vector along the z-axis, $\hat{\mathbf{z}}$. $\mathbf{M}_0$ is aligned with the static $\mathbf{B}_0$-field. The manipulation of this magnetization by means of additional time-dependent magnetic fields is the basis for all varieties of MR experiments. Despite the quantum-mechanical nature of individual protons, the macroscopic magnetization can be treated in a classical way, since individual protons are never probed in MR imaging [33]. For a single proton, the transverse component of the magnetic moment (i.e. the projection of $\boldsymbol{\mu}$ onto the xy-plane) would have to be taken into account. However, by averaging over a large number of protons (in the order of Avogadro's constant, $N_A \approx 6 \cdot 10^{23}$) these contributions cancel each other out, so that no net transverse magnetization is observed in the equilibrium state.

2.1.2 Precession of the magnetization

For an arbitrary orientation of the magnetization $\mathbf{M}$ with respect to the direction of $\mathbf{B}_0$, the time evolution of $\mathbf{M}$ is characterized by [30]

$$\frac{\partial \mathbf{M}}{\partial t} = \gamma \mathbf{M} \times \mathbf{B}_0. \tag{2.9}$$

The total magnetization $\mathbf{M}(t)$ can be decomposed into a longitudinal component $\mathbf{M}_{\parallel}(t) = M_{\parallel}(t) \cdot \hat{\mathbf{z}}$ and a transverse component $\mathbf{M}_{\perp}(t)$ so that

$$\mathbf{M}(t) = \mathbf{M}_{\parallel}(t) + \mathbf{M}_{\perp}(t). \tag{2.10}$$

This allows one to separate eq. (2.9) into

$$\frac{\partial \mathbf{M}_{\parallel}}{\partial t} = \gamma \mathbf{M}_{\parallel} \times \mathbf{B}_0 = \mathbf{0} \tag{2.11}$$

$$\frac{\partial \mathbf{M}_{\perp}}{\partial t} = \gamma \mathbf{M}_{\perp} \times \mathbf{B}_0. \tag{2.12}$$

Equation (2.12) describes the precession of the transverse magnetization about the axis defined by $\mathbf{B}_0$. The angular frequency of the precession is $\omega = \gamma B_0$, corresponding to the energetic separation $\Delta E = \gamma B_0 \hbar$ of the two states of μ_z of a single spin. If the magnetic field is solely determined by the static field $\mathbf{B}_0$, all magnetizations precess at the same frequency ω_0, which is also called *Larmor frequency*. In the presence of additional magnetic fields, $\mathbf{B} = \mathbf{B}_0 + \Delta\mathbf{B}$, eq. (2.9) becomes

$$\frac{\partial \mathbf{M}}{\partial t} = \gamma \mathbf{M} \times (\mathbf{B}_0 + \Delta\mathbf{B}) \tag{2.13}$$

$$= \gamma \mathbf{M}_{\perp} \times \mathbf{B}_0 + \gamma \mathbf{M} \times \Delta\mathbf{B}. \tag{2.14}$$

The right hand side of eq. (2.14) is a superposition of the previously mentioned precession of the transverse magnetization and a rotation of the full magnetization $\mathbf{M}$ about the axis defined by the arbitrary field vector $\Delta\mathbf{B}$. To simplify the description, a coordinate transform can be performed from the static laboratory system to a reference frame (designated by primed symbols, e.g. $\mathbf{M}'$) that rotates about the z-axis with the Larmor frequency ω_0 . Since this system rotates in synchrony with $\mathbf{M}_{\perp}$, the transverse magnetization appears static and the precession term in eq. (2.14) vanishes. If $\Delta\mathbf{B}$ is designed to rotate in the transverse plane at the Larmor frequency and to be aligned with the x'-axis, $\Delta\mathbf{B}' = \mathbf{B}_1' = B_1 \cdot \hat{\mathbf{x}}'$, the rotating-frame version of eq. (2.14)

can be formulated as

$$\frac{\partial \mathbf{M}'}{\partial t} = \gamma B_1 \left(\mathbf{M}' \times \hat{\mathbf{x}}' \right). \tag{2.15}$$

Figure 2.1 illustrates how such a magnetic field can tilt the longitudinal magnetization from its initial equilibrium state (red) by an arbitrary angle α. Since the rotation frequency of the magnetization about the direction of $\mathbf{B}_1'$ is given by $\omega_F = \gamma B_1'$, the flip angle can be calculated as $\alpha(t) = \omega_F \cdot t = \gamma B_1' \cdot t$. Arbitrary flip angles can thus be achieved by suitable combinations of the field strength and the duration for which the field is switched on.

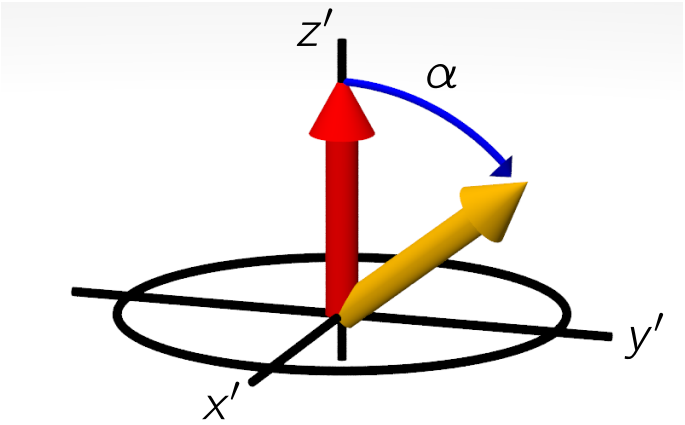

Figure 2.1: The longitudinal equilibrium magnetization (red) is tilted by the flip angle α about the x' axis in the rotating frame. The magnetic field $\mathbf{B}_1'$ is aligned with the x' axis, i.e. it rotates at the Larmor frequency ω_0 in the laboratory system.

A precessing transverse magnetization induces a sinusoidal voltage signal $S(t) = S_0 \cdot \exp(\mathrm{i}\omega t)$ in a conductor loop (usually referred to as a *receive coil*). The frequency ω of that signal is equal to the precession frequency, whereas the signal amplitude is proportional to the transverse magnetization, $S_0 \propto |\mathbf{M}_\perp|$. In an MRI scanner, heterodyne quadrature detection with respect to the Larmor frequency ω_0 is applied to the measured signal [3, pg. 371]. The result is two real-valued signals, representing the real and imaginary part of the transverse magnetization as seen in the rotating frame (i.e. at the offset frequency $\omega - \omega_0$ if the precession does not occur exactly at the Larmor frequency).

2.1.3 Relaxation

The above discussion of the precessing magnetization does not take into account dissipative interaction between spins and their environment. Since the parallel and antiparallel orientation of a magnetic moment with respect to $\mathbf{B}_0$ differs by the energy $\Delta E = \gamma \hbar B_0$, interaction of a spin with its surroundings can change the orientation of its magnetic moment. This effect gives rise to *relaxation effects*, which are crucial for MRI signal and contrast generation.

In the thermal equilibrium state, the resultant magnetization $\mathbf{M}_0$ is aligned with $\mathbf{B}_0$, which defines the z-axis of the coordinate system. At any time point t, the total magnetization $\mathbf{M}(t)$ can be decomposed into a longitudinal and a transverse component, as introduced in eq. (2.10). The presence of a transverse magnetization indicates a perturbation of the equilibrium state. Through interaction with the microscopic lattice of the medium, excess energy is dissipated over time, so that the magnetization relaxes to the initial longitudinal state. The rate of change of the longitudinal magnetization component is proportional to its deviation from the equilibrium state:

$$\frac{\partial \mathbf{M}_{\parallel}}{\partial t} = \frac{1}{T_1}\left(\mathbf{M}_0 - \mathbf{M}_{\parallel}\right). \tag{2.16}$$

T_1 is the time constant of this relaxation process. It is dependent on the magnetic field strength and on material properties. The range of T_1 in a human body at 37°C and $B_0 = 1.5$ T ranges from 50 ms (muscle) to 4500 ms (cerebro-spinal fluid) [30].

Thus far, spins were treated as non-interacting particles. This is a rough approximation, since every spin is not only exposed to the external magnetic field, but also to the magnetic moments of its immediate surroundings. These interactions overlay with $\mathbf{B}_0$, so that every spin experiences a magnetic field as a sum of those two contributions. Hence, if the field strength is variable in space, $B = B(\mathbf{r})$, ω will also become position dependent. This implies that magnetization vectors precessing at different locations will dephase over time, thus diminishing the resultant transverse magnetization. The time constant characterizing the exponential signal decay due to loss of coherence of the precession phase over a region is denoted by T_2. Locally, T_2 is an indicator of proton mobility. Mobile protons, such as those in free water, traverse through regions of increased and reduced field strength in relatively short time periods, so that opposing effects on the spin phase can partially cancel out, thus leading to a slower signal decay and increased T_2. Stationary protons, on the other hand, are

subject to the same magnetic environment for extended time periods and are therefore less likely to experience cancellation of the effect. Regions of low proton mobility are therefore characterized by small T_2 values. Inhomogeneity of the static field $\mathbf{B}_0$ constitutes another cause of signal dephasing. These deviations are caused by the magnetic material response of the tissue. The external field can be amplified or attenuated regionally, depending on the local susceptibility distribution inside the object. Surfaces (between organs or between an organ and air or fluid) and iron-rich regions induce abrupt spatial variation of the susceptibility and therefore strongly affect the magnetic field. Spatial variation of $\mathbf{B}_0$ leads to position-dependent precession frequencies, having a similar effect as the aforementioned spin-spin interactions. The decay time constant due to $\mathbf{B}_0$ inhomogeneity is denoted T_i. The compound effect of both dephasing mechanisms is quantified by $T_2^* = \left(\frac{1}{T_2} + \frac{1}{T_i}\right)^{-1}$. The decay of transverse magnetization due to dephasing is always faster than the restoration of longitudinal magnetization, $T_2 < T_1$.

2.1.4 Bloch equations

The precession of the transverse component of the magnetization and the relaxation effects are combined in the Bloch equation:

$$\frac{\mathrm{d}\mathbf{M}}{\mathrm{d}t} = \gamma \mathbf{M} \times \mathbf{B} + \frac{1}{T_1}(M_0 - M_\parallel)\hat{\mathbf{z}} - \frac{1}{T_2}\mathbf{M}_\perp. \tag{2.17}$$

$\mathbf{B}$ is the total magnetic field, which can have contributions in addition to $\mathbf{B}_0$, but it is assumed that its deviation from the z-direction (the direction of $\mathbf{B}_0$) is small. In the absence of additional fields, i.e. when $\mathbf{B} = \mathbf{B}_0$, the solution to the Bloch equation is given by [30]

$$M_x(t) = \exp\left(-\frac{t}{T_2}\right) \cdot \left(M_x(0) \cdot \cos(\omega_0 t) + M_y(0) \cdot \sin(\omega_0 t)\right) \tag{2.18}$$

$$M_y(t) = \exp\left(-\frac{t}{T_2}\right) \cdot \left(M_y(0) \cdot \cos(\omega_0 t) - M_x(0) \cdot \sin(\omega_0 t)\right) \tag{2.19}$$

$$M_\parallel(t) = M_\parallel(0) \cdot \exp\left(-\frac{t}{T_1}\right) + M_0 \cdot \left(1 - \exp\left(-\frac{t}{T_1}\right)\right). \tag{2.20}$$

For the transverse components M_x and M_y this represents a rotation about the z-axis with angular frequency ω_0 and exponentially decaying amplitude. The longitudinal component relaxes from its excited state $M_\parallel(0)$ to the equilibrium value M_0.

Additional B_1 fields are used to induce magnetization flips, as explained in section 2.1.2, usually as pulsed fields with a duration of a few milliseconds. For most imaging applications it is sufficient to assume the flips to be instantaneous, so that eqs. (2.18) to (2.20) can be used to describe the situation before and after the pulse, with an abrupt change of M_x, M_y, $M_{\|}$ (and potentially the precession phase) in between.

Maxwell's equations state that time-varying magnetic fields are always accompanied by an electric field, thus forming an electromagnetic field. Due to its frequency of 63 or 126 MHz on 1.5 and 3 Tesla scanners, respectively, a pulsed electromagnetic field is referred to as a *radio-frequency* (RF) pulse.

2.1.5 Spatial encoding

Mathematically, an image can be described as a discrete two-dimensional signal, where each pixel can be attributed a unique position in space. In order to generate images from the voltage induced by the precessing transverse magnetization in receive coils it is necessary to establish a mechanism for spatial encoding of information. The received signal $S(t)$ can then be interpreted as a superposition of the signals from isochromats (ensembles of spins with the same precession frequency) at different locations, and the image reconstruction comprises the decomposition of this compound signal into spatially resolved information.

Three distinct steps are performed to achieve spatial encoding in three-dimensional space. Each of them requires the application of a *gradient* field. Gradients generate a magnetic field parallel to the z-axis, with the magnitude being linearly dependent on one coordinate:

$$\mathbf{B}(x, y, z) = G_x\, x \cdot \hat{\mathbf{z}} \tag{2.21}$$

for an x-gradient with amplitude G_x, and analogously for y and z. These magnetic fields add to $\mathbf{B_0}$, so that the resultant magnetic field becomes

$$\mathbf{B}(x, y, z) = \big(B_0 + G_x\, x + G_y\, y + G_z\, z\big)\hat{\mathbf{z}}. \tag{2.22}$$

Subsequent application of three orthogonal gradients leads to three-dimensional spatial encoding of the MRI signal.

Slice selection

As described in section 2.1.2, a transverse rotating magnetic field $\mathbf{B}_1$ can be used to tilt the magnetization away from its longitudinal equilibrium state and generate a precessing transverse magnetization. This only works if the rotation frequency ω of $\mathbf{B}$ matches the spin precession frequency ω_p. Assuming that a z-gradient field is active while the B_1-pulse is irradiated, ω_p becomes position-dependent:

$$\omega_p(x,y,z) = \gamma B(x,y,z) = \gamma(B_0 + G_z \cdot z). \tag{2.23}$$

This implies that B_1 can only flip spins at the z-location z_0 for which the resonance condition is fulfilled, i.e. where $\omega_p(x,y,z_0) = \omega$. If, instead of being monofrequent, $\mathbf{B}$ is designed to be a superposition of oscillations with equal amplitudes over a frequency range $(\omega-\delta, \omega+\delta)$, this translates to a flip of all spins in the range $(z_0-\Delta z, z_0+\Delta z)$ with $\Delta z = \frac{\delta}{\gamma G_z}$. A waveform with uniform amplitude over the interval $(\omega-\delta, \omega+\delta)$, constituting a rectangular pulse in frequency space, corresponds to a sinc[1] in the time domain. Hence, a combination of a *slice-select* gradient and a sinc-shaped B_1-pulse can be used to excite only the spins within a slice of arbitrary orientation and thickness. This process is called *slice selection (SS)*.

Phase encoding

Phase encoding (PE)[2] is the first of two in-plane spatial encoding steps following slice-selective excitation. A phase-encoding gradient, $\mathbf{G}_{\mathrm{PE}}$, is turned on for a limited time T_{PE}. Its direction lies in the imaging plane, perpendicular to the slice-selection gradient. This introduces an in-plane dispersion of the precession frequency along the direction of the gradient. Assume that the magnetization was excited in such a way that it has zero phase offset in the rotating reference frame after the excitation. For simplicity we will assume that the imaging plane corresponds to the xy-plane (i.e. slice selection along the z-axis) and that the phase-encoding direction coincides with the y-axis, $\mathbf{G}_{\mathrm{PE}} = G_{\mathrm{PE}} \cdot \hat{\mathbf{y}}$. After application of the phase-encode gradient pulse, the off-

[1] $\mathrm{sinc}(t) = \dfrac{\sin(t)}{t}$

[2] Phase encoding in the context of MRI is not related to a technique of the same name used for digital data transmission, also known as Manchester coding.

set phase is given by

$$\begin{aligned}\phi(\mathbf{r}) &= \mathbf{r} \bullet \left(\gamma \int_0^{T_{\mathrm{PE}}} \left(\mathbf{B}(x,y,z,t) - \mathbf{B}_0 \right) \mathrm{d}t \right) \\ &= \gamma \int_0^{T_{\mathrm{PE}}} \mathbf{r} \bullet \left(G_{\mathrm{PE}} \cdot \hat{\mathbf{y}} \right) \mathrm{d}t \\ &= \gamma \cdot G_{\mathrm{PE}} \cdot y \cdot T_{\mathrm{PE}}. \end{aligned} \tag{2.24}$$

This implies that the y-position of a previously excited spin is now encoded in its precession phase.

Frequency encoding

The second in-plane encoding axis is referred to as *frequency encoding* or *read out* (*RO*) direction. After phase encoding, a readout gradient $\mathbf{G}_{\mathrm{RO}}$, perpendicular to the slice-selection and phase-encoding directions, is applied while the MR signal is sampled by means of an analog-to-digital converter (ADC) connected to the receive coil(s). If the frequency-encoding axis coincides with the x-axis and $t = 0$ denotes the time when $\mathbf{G}_{\mathrm{RO}}$ is switched on, the phase evolution can be expressed as

$$\phi(x,y,z,t) = \gamma(G_{\mathrm{PE}} \cdot y \cdot T_{\mathrm{PE}} + G_{\mathrm{RO}} \cdot x \cdot t) \tag{2.25}$$

The receive coil will "see" this signal (after quadrature detection) as a superposition of all individual signals, averaged over space:

$$\tilde{S}(t) = \int \int \int_{z_0-\Delta z}^{z_0+\Delta z} S_0(x,y,z) \cdot \exp\left(\mathrm{i}\phi(x,y,z,t)\right) \mathrm{d}z \ \mathrm{d}y \ \mathrm{d}x, \tag{2.26}$$

where $S_0(x,y,z)$ is the magnitude of the signal emitted at the location $\mathbf{r} = (x,y,z)$. If we use ϕ from eq. (2.25) and substitute $k_y = \gamma \cdot G_{\mathrm{PE}} \cdot T_{\mathrm{PE}} \cdot y$ and $k_x(t) = \gamma \cdot G_{\mathrm{RO}} \cdot t \cdot x$, this can be rewritten as

$$\tilde{S}(k_x,k_y) = \int \int \int_{z_0-\Delta z}^{z_0+\Delta z} S_0(x,y,z) \cdot \exp\left(\mathrm{i}\left(k_x \cdot x + k_y \cdot y\right)\right) \mathrm{d}z \ \mathrm{d}y \ \mathrm{d}x, \tag{2.27}$$

which is the 2D Fourier transform of the in-plane magnetization (averaged over the slice thickness $2 \cdot \Delta z$ along the z-direction). This means that $S_0(x,y,z)$ can be recovered from the signal $\tilde{S}(k_x,k_y)$ if sufficient data points in the k-space, spanned by unit vectors $\hat{\mathbf{k}}_x$ and $\hat{\mathbf{k}}_y$, are sampled and then subjected to a discrete inverse 2D Fourier

transform. Since k_x is explicitly time-dependent according to its definition, a line in k-space with fixed k_y can be sampled by recording the MR signal over time while the readout gradient is switched on. k_y is defined by the area under the phase-encoding gradient waveform prior to the signal readout, determined by its amplitude G_{PE} and duration T_{PE}. Different lines in k-space can therefore be acquired in subsequent experiments by changing the product $G_{\mathrm{PE}} \cdot T_{\mathrm{PE}}$. A more elaborate method to sample an entire k-space with a single excitation will be discussed in section 2.1.8.

If the readout of a k-space line was started immediately after the excitation of a transverse magnetization component, T_2^* relaxation would cause the signal amplitude to drop continuously along the line, so that the amplitude at one end of the line would be larger than at the opposite end. This asymmetry would inevitably cause image artefacts after Fourier transform. One technique to overcome such issues is to refocus the signal, so that its amplitude reaches a local maximum a certain time *TE* after the excitation. The local signal maximum is called an *echo*, and the interval *TE* between the excitation and the echo is referred to as *echo time*. If the readout is performed symmetrically around the echo, so that the first half of the k-space line is sampled on the rising slope of the signal envelope and the second half on the falling slope, the signal amplitude is distributed symmetrically over the line. The two principal methods for generating echos, *spin echo* and *gradient echo*, will be explained in the next two sections.

2.1.6 Spin echo

Spin echos (SE) are one of the three main principles (besides gradient echos, GE, and free induction decay, FID) applied to generate an MRI signal. The process is illustrated in fig. 2.2. In essence, a 180° RF pulse is deployed to rewind spin dephasing for generating an echo signal.

Each arrow in fig. 2.2 represents the magnetization of an isochromat (ensemble of spins with the same precession frequency) at different positions in the imaging plane. The precession frequencies of the isochromats are distinct from one another due to deviations of the magnetic field strength caused by susceptibility effects or B_0 inhomogeneity. Initially, all isochromats are in thermal equilibrium and their magnetic moments are aligned with the magnetic field along the z-axis (a). An RF pulse is irradiated (shown as a 90° pulse, but arbitrary flip angles are possible) and generates a transverse magnetization. Directly after the pulse the magnetization vectors of all

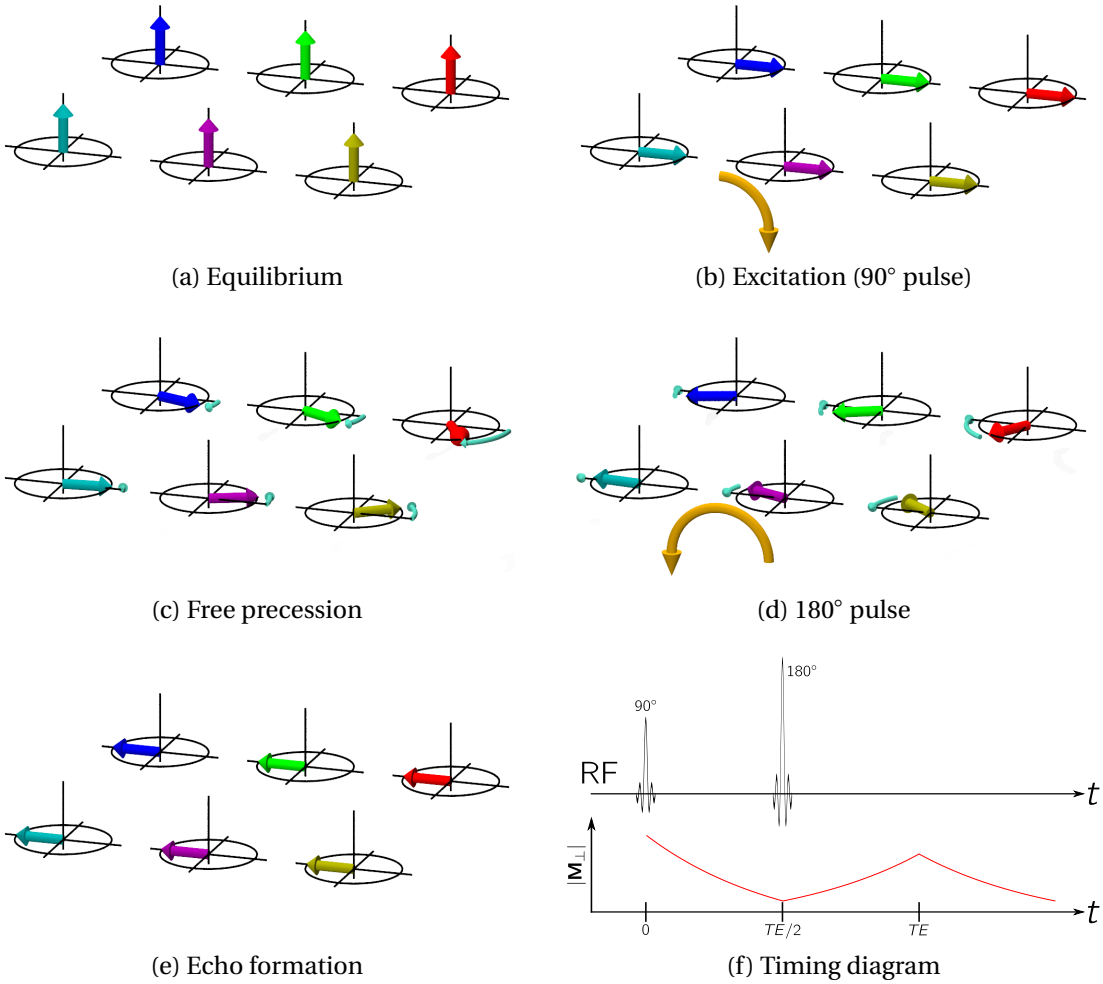

(a) Equilibrium

(b) Excitation (90° pulse)

(c) Free precession

(d) 180° pulse

(e) Echo formation

(f) Timing diagram

Figure 2.2: Illustration of the spin echo principle, from the rotating frame perspective. The arrows correspond to six isochromats at different positions within the imaging plane with different precession frequencies. The direction of the static magnetic field is upwards.

isochromats are in phase (b). The isochromats start to precess about the direction of the magnetic field at their precession frequency $\omega_p(x, y)$, indicated by the length of the circular arrows. After a certain time $t = TE/2$ of free precession, the magnetization vectors have dephased, so that their vector sum $|\mathbf{M}_\perp|$ is smaller than after the initial RF pulse (c). Next, an 180° pulse is deployed which flips the in-plane magnetization (d). During the next $TE/2$ interval, the isochromats continue to precess freely at their individual precession frequencies $\omega_p(x, y)$. Finally, at the time $t = TE$ after the excitation pulse, all isochromats are realigned, so that their magnetization vectors add up to maximum amplitude, causing a peak in the recorded MR signal.

The refocussing pulse can only reverse the effect of spatially dependent precession frequencies due to magnetic field inhomogeneities. As explained in section 2.1.3, interactions between spins lead to longitudinal (T_1) and transverse (T_2) relaxation and cause additional decoherence; hence reducing the magnitude of the transverse magnetization over time. If TE is short compared to T_1, such that T_1 relaxation during signal evolution is negligible (which is a realistic assumption for most imaging sequences), the echo amplitude can be approximated by $|\mathbf{M}_\perp(TE)| = |\mathbf{M}_\perp(0)| \cdot \exp(-TE/T_2)$.

2.1.7 Gradient echo

Gradient echos use a pair of dephaser-rephaser gradients rather than a refocussing pulse to generate an MRI echo signal. The working principle is illustrated in fig. 2.3. As in the case of a spin echo, the equilibrium longitudinal magnetization (a) is fully or partially flipped into the transverse plane by an RF pulse of arbitrary flip angle (b). Next, a dephasing gradient is applied along the readout axis (indicated by the purple cone), imposing precession frequency dispersion along that axis (c)–(d). The vector sum $|\mathbf{M}_\perp|$ of the precessing magnetization thus decreases. Eventually the dephasing gradient polarity is reversed (e), indicated by the change of the color of the cone. For every isochromat, the amplitude of the gradient-induced field strength modulation is constant, but the sign changes. Spins that experienced a strong positive field offset due to the dephaser gradient now experience a strong negative field offset. This affects the local precession frequency (in the rotating frame) in the same way; rapidly precessing spins continue to precess rapidly, but the precession direction is inverted. Finally the rephasing gradient eliminates the effect of the dephasing gradient (at the instance for which the area under the rephaser gradient waveform is equal to the area under the dephaser) and $|\mathbf{M}_\perp|$ is maximized.

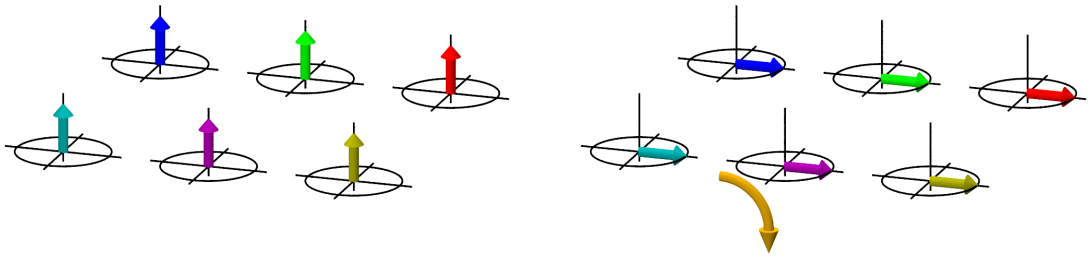

(a) Equilibrium

(b) Excitation (90° pulse)

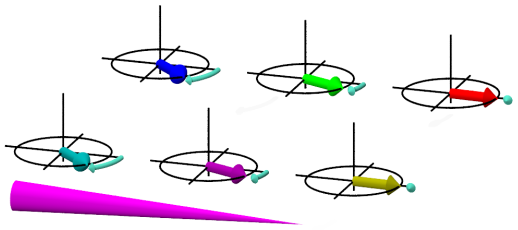

(c) Dephasing gradient

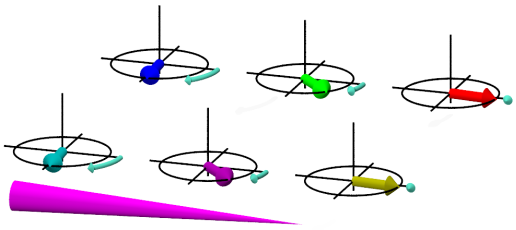

(d) Dephasing gradient

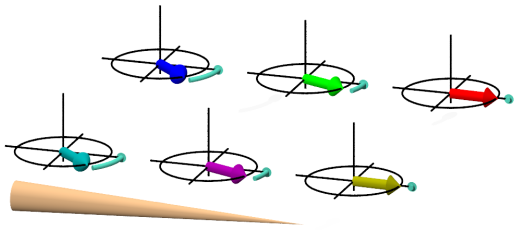

(e) Rephasing gradient

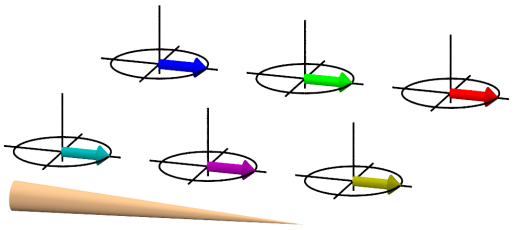

(f) Echo formation

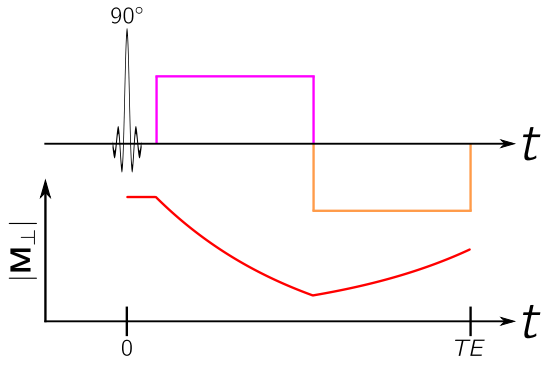

(g) Timing diagram

Figure 2.3: Illustration of the gradient echo principle, from the rotating frame perspective. The arrows correspond to six isochromats at different positions within the imaging plane with different precession frequencies. The direction of the static magnetic field is upwards. The cone indicates direction and polarity of the gradient. Further explanations are given in the text.

Spatial modulation of the precession frequency due to B_0 field inhomogeneity was neglected in fig. 2.3. However, this introduces an additional contribution to spin dephasing and cannot be compensated for by the rephasing gradient. Therefore, in contrast to a spin echo sequence, where the decay of the echo amplitude is chiefly governed by T_2, the gradient echo amplitude reduces as $|\mathbf{M}_\perp(TE)| = |\mathbf{M}_\perp(0)| \cdot \exp(-TE/T_2^*)$, with $T_2^* < T_2$ (see section 2.1.3). For a fixed TE, the gradient echo will thus have lower signal amplitude (and hence lower signal-to-noise ratio) than a spin echo.

2.1.8 Echo-planar imaging (EPI)

Echo-Planar Imaging (EPI, [54]) is an extremely fast MR imaging strategy that allows for the acquisition of an entire 2D image with a single RF excitation. In contrast to other techniques that are constrained to the acquisition of a single or several k-space lines, EPI is capable of acquiring a full 2D k-space following an excitation pulse. An oscillating readout gradient is combined with short phase-encode gradient pulses ("*blips*") to sample k-space in a zig-zag pattern. EPI can be implemented as either a gradient echo or spin echo pulse sequence. Since for this work only the latter is relevant, the following discussion focuses on the spin echo case.

As explained in section 2.1.6, an excitation pulse followed by an 180° pulse after a delay $TE/2$ will cause the formation of a spin echo signal at the time TE. Figure 2.4 depicts the basic principles of the EPI sequence. For sake of clarity, minor details are omitted from the figure. A full description can be found in [3] or [89].

The 90° pulse flips the longitudinal magnetization into the transverse $(x\,y)$ plane. Due to the *slice-select gradient* Ⓑ, only a slice of a certain thickness rather than the full volume is excited. The negative lobe of the slice-select gradient rewinds the phase dispersion that was caused by the gradient, so that after the end of the waveform all spins in the $x\,y$-plane precess in phase (neglecting dephasing effects such as B_0 inhomogeneities and dipole interaction). The *prephasing gradients* Ⓐ create an in-plane phase dispersion that will later cause the k-space sampling to begin in one corner of the 2D k-space. The 180° refocussing pulse flips the transverse magnetization, thus leading to the formation of a spin echo at the time TE with respect to the 90° pulse. The crusher gradients Ⓒ surrounding the refocussing pulse serve to compensate for imperfect inversion (i.e. spatial deviations from the expected nominal flip angle

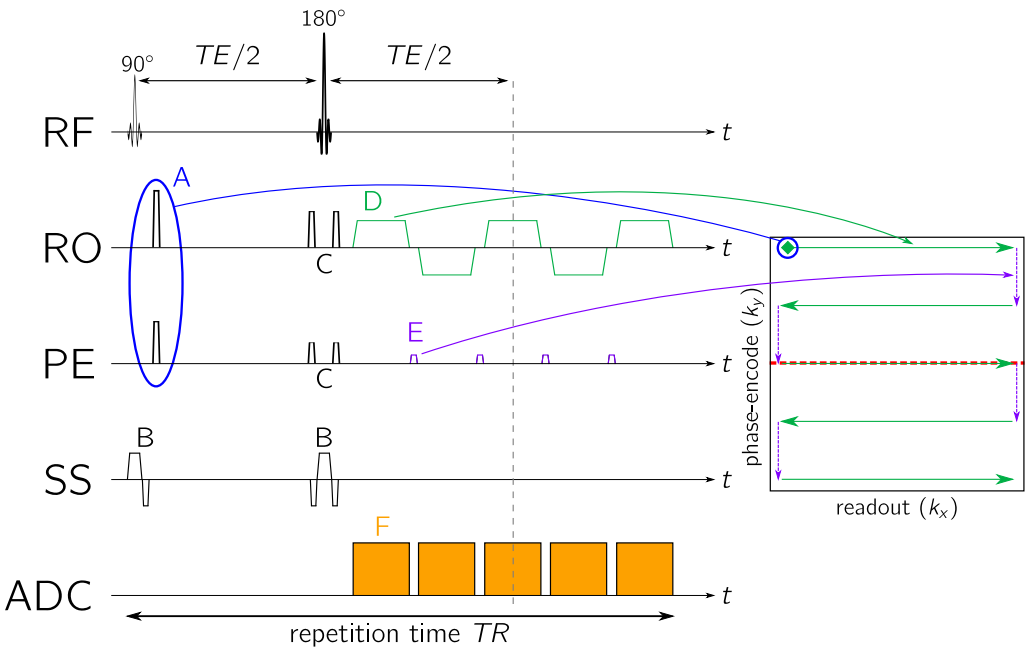

Figure 2.4: Schematic representation of the EPI sequence and its k-space trajectory. An explanation is given in the text. RF denotes radio frequency pulses. RO, PE and SS refer to readout, phase-encode and slice-select, the three orthogonal gradient directions used for spatial encoding. ADC (analog-to-digital converter) indicates recording of a radio-frequency signal. The repetition time (*TR*) is the duration of the acquisition of one slice.

of 180° due to B_0 or B_1 inhomogeneities) and to suppress an undesirable *free induction decay* (*FID*, [3]) signal that would otherwise interfere with the spin echo signal. To understand this concept it is important to note that the effect of two gradients with the same polarity before and after an 180° pulse will have opposite effects on the spins, i.e. if the first gradient causes dephasing, the second one will rephase the signal.

Signal sampling starts immediately after the refocussing pulse. A trapezoidal readout gradient Ⓓ is applied while the analog-to-digital converter samples the resultant gradient echo signal, acquiring a single line in k-space[3] (indicated by the uppermost green arrow on the right-hand side of fig. 2.4). Once the line has been recorded, the readout gradient is turned off and a short phase-encode gradient pulse Ⓔ (a *blip*) is deployed, shifting the following readout to the next line in k-space (purple dashed arrow on the right-hand side of fig. 2.4). Then the next readout gradient is deployed

[3]Sampling of a k-space line is shown here as a continuous process, whereas in reality the signal is temporally binned into typically 64–256 discrete data points.

with inverse polarity, sampling the second line of k-space in the opposite direction. This pattern of phase-encode blips and alternating readout gradients is repeated until the full k-space has been sampled. A two-dimensional FFT can be used to convert the measured signal into an image of that slice. For the sake of clarity, fig. 2.4 illustrates the acquisition of only five lines. Typically, however, a train of 64 to 256 lines is sampled after a single excitation within about 20–100 ms. This highly efficient sampling scheme makes EPI one of the fastest MRI techniques available.

After acquisition of a 2D k-space, a different slice can be acquired by repeating the same process and shifting the center frequency of the RF pulses so that they excite a different region. Alternatively, the same slice could be acquired again, either with some parameter changed or with identical parameters for signal averaging. The time required for the acquisition of a single slice is called *repetition time* and denoted by TR. Since the main part of the magnetization is in the transverse plane after the first image acquisition, one has to wait for it to return to the longitudinal state before it can be flipped again by the next 90° pulse. This limits the minimum time between acquisitions of the same slice to the order of $1-1.5$ seconds at 1.5 Tesla. However, while the magnetization in one slices relaxes back toward thermal equilibrium, a different slice can be scanned to reduce total scanning time.

The oscillating readout gradient effects a series of gradient echos. Meanwhile, the RF refocussing pulse generates a spin echo signal, which acts as the envelope for the amplitude of the individual gradient echos. Because of the symmetry property of the spin echo discussed in section 2.1.6, the spin echo amplitude is largest at the time $TE/2$ after the refocussing pulse. The sequence timing exploits this by adapting the readout train, such that the center line of k-space (the dashed red line in fig. 2.4) is sampled at that time. This guarantees maximum *signal-to-noise ratio* (SNR) for the low spatial frequencies that constitute the center of k-space and ultimately determine the overall image contrast. Conversely, the k-space periphery is sampled at lower signal amplitudes, thus imposing a limitation on the maximum attainable image resolution.

In the standard implementation of EPI, the time slot between the two RF pulses (the first $TE/2$ interval) is basically unused, with the exception of the acquisition of some auto-calibration data, which has been omitted from fig. 2.4. The overall timing is determined by the duration of the readout train. The second $TE/2$ interval is the duration between the refocussing pulse and the readout of the center of k-space and

is thus determined by the number of k-space lines to be sampled and the gradient performance. The temporal separation of the 90° and the 180° pulse is set to be equal to this required $TE/2$ interval. The empty time slot between the two RF pulses is used for MRE-relevant motion encoding, as described in section 2.2.

2.2 MR Elastography

MR Elastography was introduced in 1995 as a non-invasive method for imaging and quantifying viscoelastic properties of living biological tissue [63, 73]. It employs adapted MR imaging methods to detect mechanical waves, which are introduced into the body by an external vibration generator. Since the wave-induced displacement amplitudes are typically 1–2 orders of magnitude smaller than the spatial resolution of the image (tens to hundreds of micrometers versus ~2 mm), a highly efficient mechanism for motion detection is required. The MR sequence uses a *motion encoding gradient (MEG)* to sense wave fields. Displacement information is stored in the phase of the complex MR signal, thus decoupling motion sensitivity from image resolution. However, the signal phase is also sensitive to inhomogeneities of $\mathbf{B}_0$ and modulations of the magnetic field due to a spatially varying susceptibility distribution. The resulting phase image is therefore a superposition of information from different sources. A separation of the wave information from the other contributions is not possible with only a single image.

Magnetic field inhomogeneities and susceptibility effects are static (time-independent). Wave propagation, on the other hand, is an intrinsically dynamic process with well-defined behavior in the time domain. The key to isolating wave information is the acquisition of several images at different phases of the wave oscillation cycle. Temporal Fourier transform then separates static from dynamic effects. This requires synchrony between the vibration and the image acquisition. The general principle is outlined in fig. 2.5. A trigger signal is sent by the scanner to the vibration generator to initiate the vibration. After a certain delay τ to allow for wave propagation into the region of interest, the imaging sequence is started and a single image is acquired. Different wave phases can be measured by repeating the process with different delays τ. If the mechanical frequency is f and N wave phases are acquired, τ is reduced N times in steps of $\Delta\tau = \frac{1}{f \cdot N}$, so that one vibration cycle is sampled with N equidistant data points. Section 2.2.1 will explain how displacement information is recovered from these points.

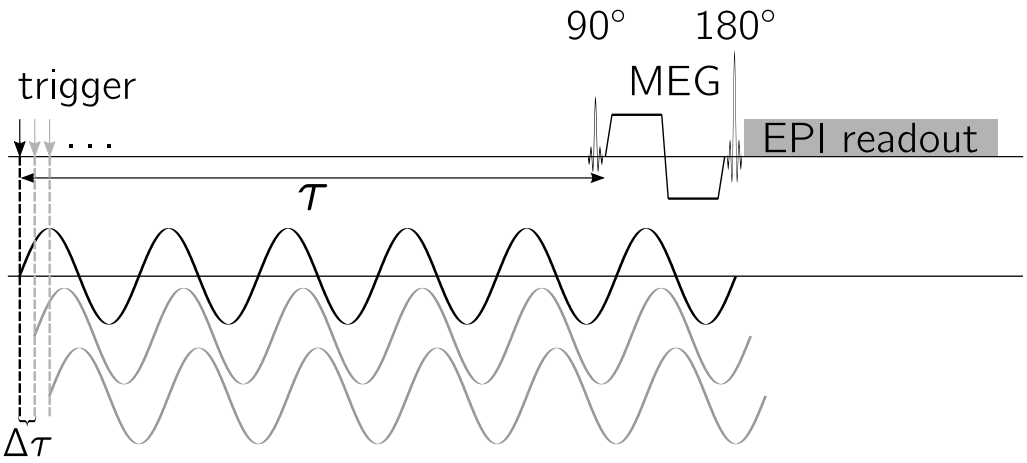

Figure 2.5: Schematic diagram of the MRE sequence used to acquire an image of a single slice. At the start of the sequence, the trigger marked by the black arrow is sent from the scanner to the vibration generator to initiate the mechanical vibration. The following delay is calculated in such a way that the offset τ between the trigger and the MEG is exactly 100 ms. In the next repetition, τ is decreased by $\Delta\tau$ (first gray arrow), so that the MEG encodes a slightly shifted wave propagation phase. Each acquisition is performed in about 150–200 ms, depending on the desired image size and resolution.

2.2.1 Motion encoding

In the rotating frame, in the presence of a gradient field $\mathbf{G}(t)$, a spin with trajectory $\mathbf{x}(t)$ accumulates a phase

$$\phi(t) = \phi(t_0) + \gamma \int_{t_0}^{t} \mathbf{G}(t') \bullet \mathbf{x}(t') \, \mathrm{d}t'. \tag{2.28}$$

For the following discussion we will set $t_0 = 0$ and $\phi(0) = 0$. We assume that the spin undergoes harmonic oscillation about its equilibrium position $\mathbf{x}_0$,

$$\mathbf{x}(t) = \mathbf{x}_0 + \mathbf{u}_0 \cdot \sin(\Omega t + \varphi).$$

We will further require that $\mathbf{G}(t)$ is zero everywhere outside the interval $[0, T]$, and that its direction does not change over time, so that it can be factorized into $\mathbf{G}(t) = \hat{\mathbf{G}}_0 \cdot g(t)$. If we are only interested in the total accumulated phase after the gradient, $\phi(t \geq T)$, eq. (2.28) can be simplified to

$$\phi(\varphi) = \gamma \left(\mathbf{x}_0 \bullet \hat{\mathbf{G}}_0 \int_0^T g(t) \, \mathrm{d}t + \mathbf{u}_0 \bullet \hat{\mathbf{G}}_0 \int_0^T g(t) \sin(\Omega t + \varphi) \, \mathrm{d}t \right). \tag{2.29}$$

Note that on the left-hand side the reference to T has been dropped and replaced with a dependence on the oscillation phase φ. $g(t)$ is usually chosen in such a way that the area under the waveform is zero, so that the first integral in eq. (2.29) vanishes. $\phi(\varphi)$ is a sinusoidal function with period 2π with respect to φ (see appendix A.1 for a proof). The phase and amplitude of $\phi(\varphi)$ are determined by the gradient waveform $g(t)$, the oscillation frequency Ω, the oscillation amplitude $|\mathbf{u}_0|$ and the angle between the gradient and the oscillation polarization, represented by the scalar product $\hat{\mathbf{G}}_0 \bullet \mathbf{u}_0$. If $\varphi(\phi)$ is sampled at N points, $\varphi_i = 2\pi\frac{i-1}{N}$, $i = 1 \ldots N$, the amplitude of $\phi(\varphi_i)$ can be obtained either from a fit of a sinusoidal function $f(A,\xi) = A \cdot \sin(x+\xi)$ or from a one-dimensional FFT of $\phi(\varphi_i)$ (see fig. 2.6). In an experiment, the sampling points φ_i are realized through repeated measurements with different delays $\tau - (i-1)\Delta\tau$, $i = 1 \ldots N$, as explained in section 2.2. By comparing the amplitude of $\phi(\varphi_i)^{(\mathrm{exp})}$ from an experiment to the amplitude of $\phi(\varphi_i)^{(\mathrm{calc})}$ simulated for a unit amplitude $|\mathbf{u}_0| = 1$, the projection of the actual displacement amplitude onto the direction of the gradient, $\mathbf{G}_0 \bullet \hat{\mathbf{u}}_0$, can be recovered. If the direction of $\hat{\mathbf{G}}_0$ is switched in successive measurements, so that projections of $\mathbf{u}_0$ onto three orthogonal axes are acquired, the full displacement vector $\mathbf{u}_0$ can be reconstructed.

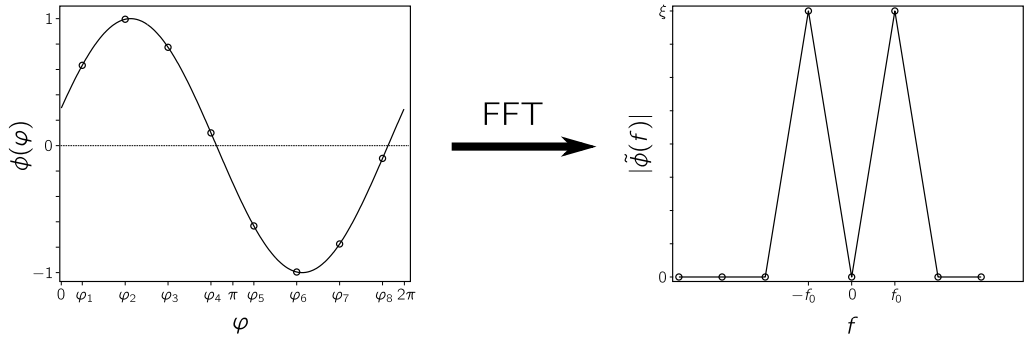

Figure 2.6: Illustration of the conversion from sampled signal phases, representing displacement amplitudes, to physical wave amplitudes. $N = 8$ sampling points $\phi(\varphi_i)$ for eq. (2.29) with unit amplitude $|\mathbf{u}_0| = 1$ are shown on the left. A fast Fourier transform (FFT) of these points yields the figure on the right. The height ξ of the two peaks at the fundamental frequencies $\pm f_0$ is the conversion factor between measured signal phases and displacements.

In practice, the gradient waveform $g(t)$ and vibration frequency Ω are chosen to meet the demands of wave mechanics, image resolution and hardware performance. A balanced waveform is used for $g(t)$, so that the $\mathbf{x}_0$-dependent term in eq. (2.29) is nulled. Wave images are then recorded as illustrated in fig. 2.5. $\hat{\mathbf{G}}_0$ is applied on three orthog-

onal axes in repeated measurements. For each direction of $\mathbf{G}_0$, N wave phases (typically $N = 4$ or $N = 8$) are recorded by gradually decreasing the delay τ. $\phi(\varphi_i)^{(\mathrm{calc})}$ is calculated according to eq. (2.29) for a unit amplitude $\hat{\mathbf{u}}_0$ parallel to $\hat{\mathbf{G}}_0$. The conversion factor ξ is obtained by numerically or analytically calculating the amplitude of the fundamental frequency of $\tilde{\phi} = \mathrm{FFT}[\phi(\varphi_i)]$, as shown in fig. 2.6. The displacement field $\mathbf{u}^{(\mathrm{exp})}$ can then be derived as

$$\tilde{u}_i^{(\mathrm{exp})}(\mathbf{r}) = \xi \tilde{\phi}_i(\mathbf{r}), \tag{2.30}$$

where $\tilde{\phi}_i$ is the Fourier-transformed signal phase (evaluated at the vibration frequency Ω) that was recorded as a projection of $\mathbf{u}$ onto the i-th Cartesian axis, i.e. with $\hat{\mathbf{G}}_0 = \hat{\mathbf{e}}_i$.

2.2.2 Gradient moment nulling

Any smooth trajectory $\mathbf{x}(t)$ of a signal-generating particle can be expanded into a Taylor series at t_0:

$$\mathbf{x}(t) = \sum_{k=0}^{\infty} \frac{1}{k!} \left. \frac{\partial^k \mathbf{x}(t)}{\partial t^k} \right|_{t=t_0} \cdot (t - t_0)^k. \tag{2.31}$$

Substituting eq. (2.31) into eq. (2.28) yields [3, pg. 336]

$$\begin{aligned}
\phi(t) &= \phi(t_0) + \sum_{k=0}^{\infty} \frac{1}{k!} \int_{t_0}^{t} \mathbf{G}(t') \bullet \left. \frac{\partial^k \mathbf{x}(\vartheta)}{\partial \vartheta^k} \right|_{\vartheta=t_0} \cdot (t' - t_0)^k \, \mathrm{d}t' \\
&= \phi(t_0) + \sum_{k=0}^{\infty} \frac{1}{k!} \left. \frac{\partial^k \mathbf{x}(\vartheta)}{\partial \vartheta^k} \right|_{\vartheta=t_0} \bullet \int_{t_0}^{t} \mathbf{G}(t') \cdot (t' - t_0)^k \, \mathrm{d}t' \\
&= \phi(t_0) + \sum_{k=0}^{\infty} \frac{1}{k!} \left. \frac{\partial^k \mathbf{x}(\vartheta)}{\partial \vartheta^k} \right|_{\vartheta=t_0} \bullet \mathbf{M}_k(t)
\end{aligned} \tag{2.32}$$

with the k-th *gradient moment*

$$\mathbf{M}_k(t) = \int_{-\infty}^{t} \mathbf{G}(t') \cdot t'^k \, \mathrm{d}t'. \tag{2.33}$$

Shifting the lower integration limit from t_0 to $-\infty$ is permissible, since in the previous section we required that $\mathbf{G}(t)$ be zero for $t < t_0$. The translation invariance

$$\int_{-\infty}^{t} \mathbf{G}(t') \cdot (t' - t_0)^k \, \mathrm{d}t' = \int_{-\infty}^{t} \mathbf{G}(t') \cdot t'^k \, \mathrm{d}t'$$

that was implicitly used in the last step of eq. (2.32) is only true if all gradient moments $0 \ldots (n-1)$ vanish. This is the case for all MEG waveforms considered in this work. Because of this time translation invariance we will henceforth use a time axis that is defined by the start ($t_0 = 0$) and end ($t = T$) of the gradient waveform. Since we are only interested in the total effect of the MEG on the signal phase of a particle, $\phi(T)$ is the relevant quantity.

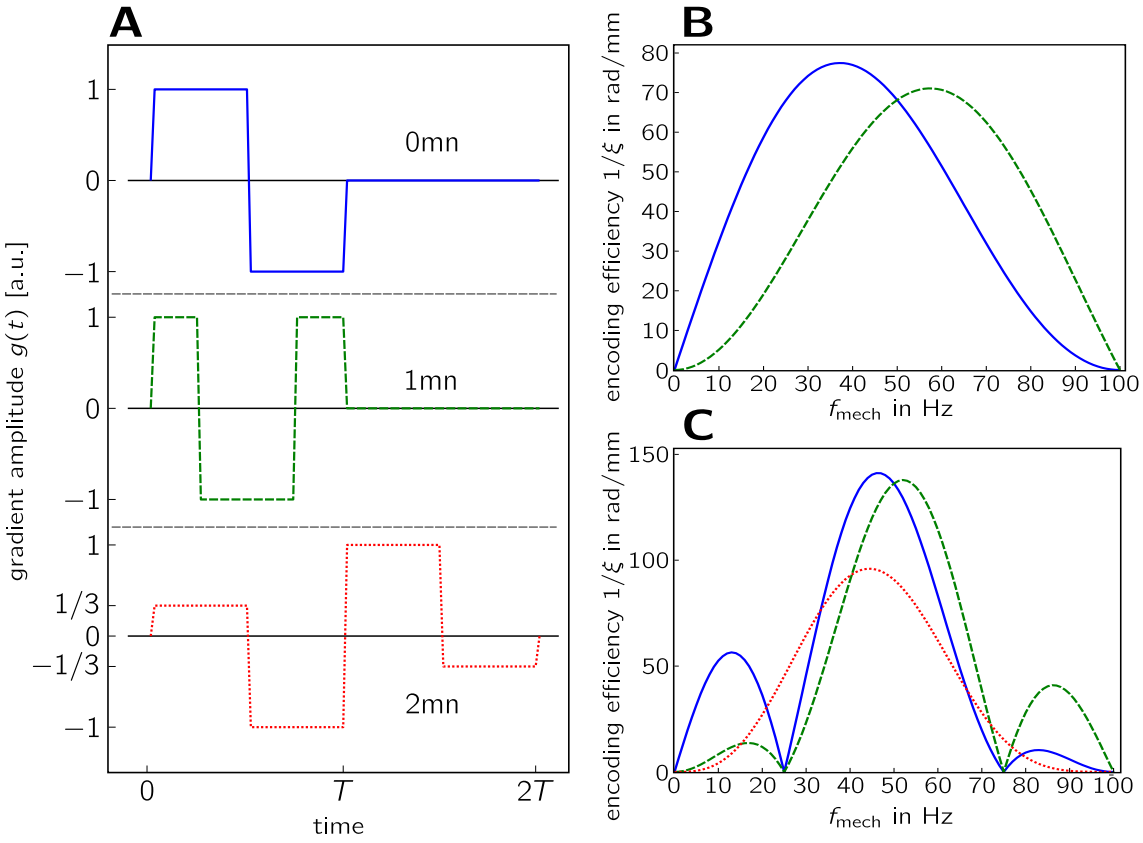

Figure 2.7: Different orders of gradient moment nulling. **A:** Waveforms with 0^{th} (solid), 1^{st} (dashed) and 2^{nd} (dotted) moment nulling (mn), composed of individual trapezoidal shapes. For 0^{th} and 1^{st} mn, one cycle with period T is shown. 2^{nd} mn can only be implemented with an even number of cycles, each with period T. **B:** Encoding sensitivity for one cycle with 0^{th} and 1^{st} mn with $T = 20$ ms and gradient amplitude 20 mT/m in the mechanical vibration frequency range $0 - 100$ Hz. **C:** Encoding sensitivity for two cycles with $T = 20$ ms.

$\mathbf{M}_0 = \mathbf{0}$ is the prerequisite for stationary spins not accumulating a position-dependent phase by nulling the term $\mathbf{x}(0)$ in the series expansion of $\mathbf{x}(t)$. This implies that the total area under the gradient waveform has to be zero. A commonly used waveform with this property is a sine or its trapezoidal approximation. Higher-order

gradient moment nulling can be employed to suppress artifacts induced by laminar, turbulent or pulsatile flow of blood or cerebro-spinal fluid. Typical gradient waveforms to achieve moment nulling of orders up to 2 are shown in fig. 2.7, along with their motion sensitivity profiles.

If the first gradient moment is also nulled ($\mathbf{M}_0 = \mathbf{0}$ and $\mathbf{M}_1 = \mathbf{0}$), the constant-velocity term $t \cdot \frac{\partial \mathbf{x}}{\partial t}\Big|_{t=0}$ is eliminated in addition to the static position-dependent contribution. Particles moving at constant speed, as in constant-velocity flow, will not acquire an additional phase from the motion encoding gradient. A cosine or its rectangular approximation constitutes a suitable waveform.

Second-order gradient moment nulling ($\mathbf{M}_0 = \mathbf{0}$, $\mathbf{M}_1 = \mathbf{0}$, and $\mathbf{M}_2 = \mathbf{0}$) can be implemented as a train of four trapezoids of equal duration with relative amplitudes (+1/3, −1, +1, −1/3), constituting two cycles. In addition to the effects of first-order moment nulling, $\mathbf{M}_2 = \mathbf{0}$ suppresses the constant-acceleration term $t^2 \cdot \frac{\partial^2 \mathbf{x}}{\partial t^2}\Big|_{t=0}$ in eq. (2.31), so that particles accelerating at a constant rate will not accumulate a signal phase. This effect becomes relevant in the presence of pulsating or turbulent flow.

These three gradient waveforms possess different sensitivities for sinusoidal mechanical vibration, as illustrated in fig. 2.7 B and C. Figure 2.7 B corresponds to the encoding efficiency of a 20 ms waveform with 0^{th} (0mn) and 1^{st} (1mn) moment nulling, i.e. one cycle at an MEG frequency of 50 Hz. The sensitivity maximum for 1mn is shifted towards higher frequencies. While the peak values for the two curves are similar, the 1mn waveform exhibits significantly lower sensitivity toward low mechanical vibration frequencies, implying that it is less susceptible to distortions induced by cardiac motion (~1 Hz).

In fig. 2.7 C the sensitivity profiles for 40 ms waveforms are shown. For 0mn and 1mn this corresponds to two cycles of the configuration shown in fig. 2.7 A, whereas in the case of 2mn only one cycle of the compound waveform is employed. 2mn provides even more robustness against low-frequency artifacts than 1mn at the cost of a lower peak sensitivity and a broader frequency spectrum. For 0mn and 1mn, peak encoding efficiency and spectral selectivity (width of the central peak) are better if two cycles are employed. However, the sensitivity nulls at odd multiples of the first subharmonic frequency have to be taken into account, especially in measurements with multiple simultaneous mechanical vibration frequencies [42, 83]

These sensitivity profiles indicate that the vibration frequency and the MEG frequency do not necessarily have to be equal. Encoding schemes with $f_{\mathrm{mech}} \neq f_{\mathrm{MEG}}$ were conceived by Rump et al. [83] and termed *fractional encoding*. In general, longer motion encoding periods with multiple MEG cycles offer superior sensitivity characteristics, but they also require longer echo times, thus causing lower signal quality due to T_2 decay and longer total measurement durations. Selecting a suitable MEG waveform is therefore oftentimes a compromise between sensitivity and signal quality.

2.3 Viscoelastic theory

Elasticity and viscosity are two physical concepts used to describe the response of a solid body to an external force. Both cases include a deformation of the body as a consequence of that force. Initially, the body will exert an opposing force, i.e. a resistance to deformation. In the fully elastic case, this opposing force will restore the initial shape of the body after the external force has been removed. The resistance of a viscous medium decreases over time as it "flows" into a new shape that is in equilibrium with the external forces. After the removal of the force, the body will stay in its new shape and will not return to the original pre-deformation state. Real materials will usually have intermediate characteristics, exhibiting both viscous and elastic properties at the same time.

2.3.1 Stress and strain

The description of the response of a medium to deformation is given in terms of *strain* and *stress*. Strain represents the deflection of a mass point from its original position in the undeformed body. Stress quantifies the forces counteracting deformation throughout the medium. Both stress and strain are physical quantities which can – at least in principle – be measured directly, whereas the relationship between them is subject to physical modeling.

In the following section, a continuous medium will be represented as a number of discrete masses arranged on a rectangular lattice. This formalism is useful to illustrate the key concepts of elasticity; however, it is not limited to highly ordered systems such as perfect crystals. All findings are also applicable to more unstructured systems, such as biological tissue. The following sections follow the presentation in [47] and [1].

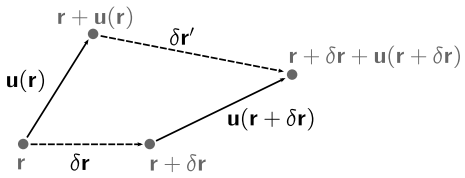

Figure 2.8: Nomenclature used for positions and displacements in a solid body. The two points $\mathbf{r}$ and $\mathbf{r}+\delta\mathbf{r}$ are subject to a displacement $\mathbf{u}$. Dashed lines represent connections between points before and after a deformation. Solid lines correspond to displacements. Points and their position vectors before and after the deformation are shown in gray.

The deformation of a three-dimensional object can be described in terms of its associated *displacement field* $\mathbf{u}$ in the sense that every point $\mathbf{r}$ is shifted to a different position $\mathbf{r}+\mathbf{u}(\mathbf{r})$. A deformation can change the distance between two points. In the undisturbed state, the distance between the points $\mathbf{r}$ and $\mathbf{r}+\delta\mathbf{r}$ is $D=|\delta\mathbf{r}|$. The deformation shifts these points to $\mathbf{r}+\mathbf{u}(\mathbf{r})$ and $\mathbf{r}+\delta\mathbf{r}+\mathbf{u}(\mathbf{r}+\delta\mathbf{r})$, respectively, as shown in fig. 2.8. The variation $\delta\mathbf{u}=\mathbf{u}(\mathbf{r}+\delta\mathbf{r})-\mathbf{u}(\mathbf{r})$ for infinitesimal distances $\delta\mathbf{r}$ is then

$$\delta u_i = \sum_{j=1}^{3} \frac{\partial u_i}{\partial r_j} \delta r_j. \tag{2.34}$$

In appendix A.2 it will be shown that this can equally be expressed as [1, pg. 13]

$$\delta u_i = \frac{1}{2}\left(\frac{\partial u_i}{\partial r_j} + \frac{\partial u_j}{\partial r_i}\right) + \frac{1}{2}\left((\nabla \times \mathbf{u}) \times \delta\mathbf{r}\right)_i \tag{2.35}$$

The first term on the right-hand side of eq. (2.35) is referred to as an *infinitesimal strain tensor*:

$$\epsilon_{ij} = \frac{1}{2}\left(\frac{\partial u_i}{\partial r_j} + \frac{\partial u_j}{\partial r_i}\right) = \frac{1}{2}\left(\nabla\mathbf{u} + (\nabla\mathbf{u})^{\mathrm{T}}\right). \tag{2.36}$$

$\boldsymbol{\epsilon}$ is a symmetric ($\epsilon_{ij}=\epsilon_{ji}$) tensor of rank 2 which can be expressed as a 3×3 matrix. Due to its symmetry, only six of nine entries are independent. The second term in eq. (2.35) corresponds to an infinitesimal rotation in the vicinity of the point $\mathbf{r}$.

The trace of the strain tensor, $\mathrm{tr}(\boldsymbol{\epsilon}) = \nabla \bullet \mathbf{u}$, quantifies a change of volume according to $V' = V\cdot(1+\mathrm{tr}(\boldsymbol{\epsilon}))$ for a small volume element V. The off-diagonal elements of $\boldsymbol{\epsilon}$ parametrize shear strain. If two position vectors $\mathbf{v}_1$ and $\mathbf{v}_2$ are orthogonal in the undistorted state ($\theta = \measuredangle(\mathbf{v}_1,\mathbf{v}_2) = \frac{\pi}{2}$), the angle $\theta' = \measuredangle(\mathbf{v}_1',\mathbf{v}_2')$ between them after the

deformation can be calculated according to

$$\cos\theta' = \frac{\mathbf{v}_1' \bullet \mathbf{v}_2'}{|\mathbf{v}_1'| \cdot |\mathbf{v}_2'|}.$$

It is shown in [46, pg. 100] that this can be equally represented as

$$\cos\theta' = \frac{2}{|\mathbf{v}_1| \cdot |\mathbf{v}_2|} \mathbf{v}_1 \cdot \boldsymbol{\epsilon} \cdot \mathbf{v}_2.$$

Thus, θ is changed by an angle $\gamma = \theta' - \theta = \theta' - \frac{\pi}{2}$ and hence

$$\cos\theta' = \cos(\frac{\pi}{2} + \gamma) = -\sin(\gamma) = \frac{2}{|\mathbf{v}_1| \cdot |\mathbf{v}_2|} \mathbf{v}_1 \cdot \boldsymbol{\epsilon} \cdot \mathbf{v}_2. \tag{2.37}$$

By selecting $\mathbf{v}_1 = \hat{\mathbf{n}}_i$ and $\mathbf{v}_2 = \hat{\mathbf{n}}_j$, $i \neq j$, eq. (2.37) reduces to

$$-\sin\gamma = 2 \cdot \hat{\mathbf{n}}_i \cdot \boldsymbol{\epsilon} \cdot \hat{\mathbf{n}}_j = 2\epsilon_{ij}.$$

For small angles γ, the approximation $\sin\gamma \approx \gamma$ can be used, so that $\gamma = -2\epsilon_{ij}$ can be understood as the angle by which the i-th and j-th Cartesian axes are rotated away from each other under deformation.

The strain tensor is a purely phenomenological description of the deformation of the body; it contains no information about the cause of the deformation. The forces acting at a point in a solid body can be fully represented by a decomposition into force components parallel and perpendicular to the faces of a small cubic volume element around that point. This yields three forces for each of the three pairs of mutually parallel faces of the cube, resulting in a total of nine components. In the following discussion we will assume that the cube is aligned with a Cartesian coordinate system and we will identify the axes according to $x = 1,\ y = 2,\ z = 3$. Figure 2.9 illustrates this concept for two sides of the cube.

The forces, normalized to the area A of one face of the cube, are termed *stresses*. The nine stress components are summarized in the *stress tensor* $\boldsymbol{\sigma}$, where the element σ_{ij}, $i, j \in \{1,2,3\}$ represents the stress along the j-th Cartesian axis on the surface orthogonal to the i-th axis. Consequently, the diagonal components σ_{ii} act orthogonally on the three surfaces. In other words, these forces are directed either towards or away from the center of the cube, and act to either compress or expand it. The off-diagonal entries σ_{ij}, $i \neq j$ characterize stresses tangential to their respective sur-

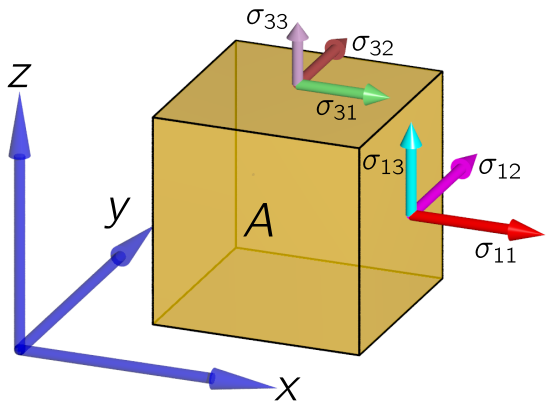

Figure 2.9: Definition of the nomenclature for the stress tensor elements σ_{ij}. The same convention is also used for the strain tensor elements ϵ_{ij}.

faces. They exert a torque on the volume element, causing shear deformation while conserving volume. If the resultant torque of all stresses does not vanish, the cube will rotate. Therefore, the necessary and sufficient condition for a static (equilibrium) configuration is that $\sigma_{ij} = \sigma_{ji}$ for all pairs $(i \neq j)$, so that all torque components cancel. In fig. 2.9 this is shown for the stresses σ_{31} and σ_{13}, which act on the same edge and with the same strength, and therefore balance one another. The same must be true for all other pairs of tangential stress components. This condition implies that only six out of the nine entries of the stress tensor are independent as long as a bulk rotation of the object is prevented.

The diagonal elements σ_{ii}, on the other hand, compress or expand the volume. Since they act orthogonally on the surfaces of the cube rather than tangentially, they do not cause rotation.

Stress and strain are not independent of one another. The link between the two depends on the material type and its characteristics. Hooke's law models the relationship between the two tensors in a linear way:

$$\sigma_{ij} = \sum_{k,l=1}^{3} c_{ijkl}\,\epsilon_{kl} \tag{2.38}$$

According to this relationship, every single stress σ_{ij} is a function of the full strain field $\boldsymbol{\epsilon}$. If eq. (2.38) is an accurate description of the stress-strain relation of a given medium, that medium is classified as *linear elastic*. $\mathbf{c}$ is a fourth-order tensor with $3^4 = 81$ elements. The symmetries of $\boldsymbol{\sigma}$ and $\boldsymbol{\epsilon}$ impose some constraints on the elements of

c, namely $c_{ijkl} = c_{jikl}$, $c_{ijkl} = c_{ijlk}$ and $c_{ijkl} = c_{klij}$, so that only 21 of its elements are independent. If the medium is isotropic, the number of constants reduces further, so that **c** can be parametrized as

$$c_{ijkl} = \lambda\delta_{ij}\delta_{kl} + \mu\left(\delta_{ik}\delta_{jl} + \delta_{il}\delta_{jk}\right),$$

with the shear modulus μ and the first Lamé parameter λ, both being scalar parameters. In this case, eq. (2.38) reduces to

$$\begin{aligned}\sigma_{ij} &= \sum_{k,l=1}^{3}\left(\lambda\delta_{ij}\delta_{kl} + \mu(\delta_{ik}\delta_{jl} + \delta_{il}\delta_{jk})\right)\epsilon_{kl} \\ &= \delta_{ij}\lambda\sum_{k=1}^{3}\epsilon_{kk} + \mu\underbrace{(\epsilon_{ij} + \epsilon_{ji})}_{\epsilon_{ij}=\epsilon_{ji}} \\ &= \delta_{ij}\lambda\cdot\mathrm{tr}(\boldsymbol{\epsilon}) + 2\mu\epsilon_{ij}.\end{aligned}$$

2.3.2 Mechanical waves

The balance of momentum in a homogeneous, isotropic elastic solid is represented by Navier's equation [26, pg. 274]:

$$(\lambda+\mu)\,\nabla(\nabla\bullet\mathbf{u}) + \mu\,\nabla^2\mathbf{u} + \rho\mathbf{f} = \rho\ddot{\mathbf{u}}. \tag{2.39}$$

ρ is the bulk material density and **f** is the body force density in the material, e.g. due to gravitational effects. The square of the nabla operator can be rewritten according to the vector calculus identity

$$\nabla^2\mathbf{X} = \nabla(\nabla\bullet\mathbf{X}) - \nabla\times\nabla\times\mathbf{X}. \tag{2.40}$$

In the following we will neglect any body forces. According to Helmholtz's theorem, an arbitrary vector field can be decomposed into a divergence-free and a curl-free field:

$$\mathbf{X} = \mathbf{X}_T + \mathbf{X}_L \tag{2.41}$$

$$\text{with}\quad \nabla\times\mathbf{X}_L = \mathbf{0}\quad\text{and} \tag{2.42}$$

$$\nabla\bullet\mathbf{X}_T = 0. \tag{2.43}$$

The indices L and T refer to "longitudinal" and "transverse", respectively. The linearity of eq. (2.39) allows for separation into two components by applying the curl or divergence operator. Taking the curl and divergence of eq. (2.39) and exploiting eq. (2.40) and the general relations $\nabla \bullet (\nabla \times \mathbf{X}) = 0$ and $\nabla \times (\nabla \chi) = \mathbf{0}$ for arbitrary scalar functions χ and vector functions $\mathbf{X}$, one obtains:

$$\begin{aligned} \nabla \bullet \big((\lambda+\mu)\,\nabla(\nabla \bullet \mathbf{u})\big) + \mu\,\nabla \bullet (\nabla(\nabla \bullet \mathbf{u})) &= \rho \nabla \bullet \ddot{\mathbf{u}} \\ \Rightarrow \quad (\lambda+2\mu)\,\nabla \bullet (\nabla(\nabla \bullet \mathbf{u})) &= \rho \nabla \bullet \ddot{\mathbf{u}} \\ \Leftrightarrow \qquad (\lambda+2\mu)\,\nabla^2(\nabla \bullet \mathbf{u}) &= \rho\,\frac{\partial^2}{\partial t^2}\nabla \bullet \mathbf{u} \end{aligned} \tag{2.44}$$

and

$$\begin{aligned} \nabla \times \big(-\mu\,\nabla \times \nabla \times \mathbf{u}\big) &= \rho\,\nabla \times \ddot{\mathbf{u}} \\ \Rightarrow \qquad \mu\,\nabla^2(\nabla \times \mathbf{u}) &= \rho\,\frac{\partial^2}{\partial t^2}\nabla \times \mathbf{u}. \end{aligned} \tag{2.45}$$

In these derivations, λ and μ are assumed to be close to constant, so that all of their spatial derivatives can be neglected in accordance with the assumption of a homogeneous medium. Equations (2.44) and (2.45) constitute wave equations for the fields $\nabla \bullet \mathbf{u}$ and $\nabla \times \mathbf{u}$, respectively. By comparing them to the general wave equation

$$\nabla^2 \chi = \frac{1}{c^2}\frac{\partial^2 \chi}{\partial t^2} \tag{2.46}$$

with propagation velocity c, we see that the two wave fields propagate at different velocities:

$$c_L = \sqrt{\frac{2\mu+\lambda}{\rho}} \tag{2.47}$$

$$c_T = \sqrt{\frac{\mu}{\rho}}. \tag{2.48}$$

The longitudinal wave therefore travels faster than the transverse wave. A vector solution to eq. (2.46) has the form

$$\boldsymbol{\chi}(\mathbf{r}, t) = \boldsymbol{\chi}_0 \cdot \exp(\pm \mathrm{i} \cdot (\mathbf{k} \bullet \mathbf{r} - \Omega t))$$

with polarization $\boldsymbol{\chi}_0$, wave vector $\mathbf{k}$ and angular frequency Ω. Taking the divergence yields

$$\nabla \bullet \boldsymbol{\chi} = \pm \mathrm{i} \mathbf{k} \bullet \boldsymbol{\chi}_0 \cdot \exp(\pm \mathrm{i} \cdot (\mathbf{k} \bullet \mathbf{r} - \Omega t)).$$

For the transverse wave, the requirement $\nabla \bullet \boldsymbol{\chi} = 0$ can only be fulfilled if the oscillation is orthogonal to the propagation direction, so that $\mathbf{k} \bullet \boldsymbol{\chi}_0 = 0$. The longitudinal wave is characterized by the condition

$$\nabla \times \boldsymbol{\chi} = \pm \mathrm{i} \boldsymbol{\chi}_0 \times \mathbf{k} \cdot \exp(\pm \mathrm{i} \cdot (\mathbf{k} \bullet \mathbf{r} - \Omega t)) = \mathbf{0},$$

implying that $\boldsymbol{\chi}_0 \times \mathbf{k} = \mathbf{0}$, so that the polarization must be parallel to the propagation direction.

In practice, any time-harmonic displacement field $\mathbf{u}(\mathbf{r}, t)$ will be a superposition of a longitudinal and a transverse wave field. According to eqs. (2.41) to (2.43), the curl and divergence operators can be used to separate the compound field into its two constituents. As stated in section 2.3.1, $\nabla \bullet \mathbf{u} = \mathrm{tr}(\boldsymbol{\epsilon})$ quantifies volumetric strain, i.e. local dilatation or compression, whereas the off-diagonal elements $\epsilon_{ij} = \frac{1}{2}\left(\frac{\partial u_i}{\partial r_j} + \frac{\partial u_j}{\partial r_i}\right)$ relate to shear strain.

2.3.3 Inversion of the wave equation

The solutions of the unattenuated wave equations (2.44) and (2.45) are time-harmonic displacement fields:

$$\mathbf{u}(\mathbf{r}, t) = \mathbf{u}_0(\mathbf{r}) \cdot \exp(-\mathrm{i}\Omega t). \tag{2.49}$$

With this information, eq. (2.44) can be inverted:

$$\begin{aligned} &(2\mu + \lambda)\nabla^2(\nabla \bullet \mathbf{u}) = -\rho \Omega^2 \nabla \bullet \mathbf{u} \\ \Rightarrow \quad &M = 2\mu + \lambda = -\rho \Omega^2 \frac{\nabla \bullet \mathbf{u}}{\Delta(\nabla \bullet \mathbf{u})}, \end{aligned} \tag{2.50}$$

where M is the *P-wave modulus* (which will be discussed in section 2.3.4) and $\Delta = \nabla^2$ is the 3-dimensional Laplacian.

The shear wave equation eq. (2.45), in contrast, is a vector equation and therefore cannot be inverted in the same fashion. One solution would be to perform the inversion component-wise, which would yield three values for μ. Those could then be either

averaged, assuming isotropy of the material, or be treated as three distinct characteristic quantities of an anisotropic medium. Alternatively, eq. (2.45) can be converted into a scalar equation by multiplying both sides with a 3-component vector. By defining $\mathbf{c} \equiv \nabla \times \mathbf{u}$ and multiplying both sides of the equation by $\nabla^2\mathbf{c}$, one obtains a solution that minimizes the sum of least squares:

$$\begin{aligned} & \mu \nabla^2(\nabla \times \mathbf{u}) = -\rho \Omega^2 \nabla \times \mathbf{u} \\ \underset{(\mathbf{c}=\nabla\times\mathbf{u})}{\Longrightarrow} \quad & \mu \left(\nabla^2\mathbf{c}\right) \bullet \left(\nabla^2\mathbf{c}\right) = -\rho \Omega^2 \mathbf{c} \bullet \left(\nabla^2\mathbf{c}\right), \end{aligned}$$

which in turn can be solved for μ:

$$\mu = -\rho \Omega^2 \frac{\mathbf{c} \bullet \left(\nabla^2\mathbf{c}\right)}{(\nabla^2\mathbf{c}) \bullet (\nabla^2\mathbf{c})} \tag{2.51}$$

Multiplication by $\nabla^2\mathbf{c}$ introduces a weighted average of the Cartesian displacement field components based on the curvature of their respective fields. Two implications have to be considered. Firstly, curvature is proportional to the displacement amplitude along each direction, so components with large amplitudes (and hence potentially higher signal-to-noise ratio) contribute more to the calculated modulus value. Secondly, at constant amplitude, curvature is larger if the wavelength is shorter, so that components with a shorter wavelength are given a larger weight. However, averaging over the Cartesian field components is only permissible if isotropy of the medium is assumed. In that case, no significant direction-dependent variability of the moduli is to be expected.

2.3.4 Compression modulus and oscillating volumetric strain

In MRE experiments, the compression modulus K, like the shear modulus μ, is not a directly measurable quantity; it can only be calculated from stress and strain. This section discusses a simple relationship that can be used to detect changes in K between different physiological states by quantifying induced oscillating strain.

The volume V of a compressible medium is not constant; it changes as a function of the external pressure P. For a linear medium, the relation between a pressure change

ΔP and volume change ΔV is linear:

$$\Delta P = -K\frac{\Delta V}{V}. \tag{2.52}$$

The proportionality constant K is called *compression modulus* or *bulk modulus*. Since ΔP and ΔV have to be of opposite sign (a pressure increase leads to a decrease of volume and vice versa), K is always positive. It is related to the previously introduced *shear modulus* μ and the *first Lamé parameter* λ [47, pg. 10]:

$$K = \lambda + \frac{2}{3}\mu.$$

With this relation, the expression for the compression wave propagation speed, eq. (2.47), can be reformulated as

$$c_L = \sqrt{\frac{K + \frac{4}{3}\mu}{\rho}} = \sqrt{\frac{M}{\rho}}$$

with the *pressure wave modulus* (or *P-wave modulus*) $M = K + \frac{4}{3}\mu$.

Equation (2.52) is not restricted to a static context, but it is also valid in a dynamic setting. If an oscillating pressure $\tilde{P} = P_0 \exp(-\mathrm{i}\Omega t)$ acts on the medium, the relation can be stated as

$$\tilde{P} = -K\frac{\Delta\tilde{V}}{V}, \tag{2.53}$$

where $\Delta\tilde{V}$ denotes the oscillation of the volume about its equilibrium value V at angular frequency Ω. In the general case of a viscoelastic medium, K is a complex number, with the real and imaginary part representing elastic and viscous behavior, respectively. Taking the magnitude of both sides of the equation leads to

$$\left|\tilde{P}\right| = |K| \cdot \frac{\left|\Delta\tilde{V}\right|}{V}.$$

The normalized volume change $\frac{\left|\Delta\tilde{V}\right|}{V}$ is equivalent to the divergence of the pressure-induced displacement field, i.e the volumetric strain:

$$\left|\tilde{P}\right| = |K| \cdot |\nabla \bullet \mathbf{u}|. \tag{2.54}$$

This implies that a measurement of the magnitude of the oscillating volumetric strain

is representative of the oscillating pressure magnitude.

2.4 Poroelasticity

Human tissue typically has a water content of approximately 70–85 % [20, 88]. With a compression modulus of 2.2 GPa, water is considered incompressible in most experimental settings. Consequently, MR Elastography usually makes the assumption that tissue can undergo shear deformation but does not permit compression.

The theory of poroelasticity was derived by Maurice Biot in the 1940s and 50s, originally for modeling the behavior of soil and rocks under pressure [6, 7] in a static context. Later Biot extended his theory to the dynamic regime, analyzing wave propagation using this framework [8, 9].

Poroelastic behavior arises from the interaction of the two compartments of a biphasic medium, in which a solid but porous matrix is fully permeated by an incompressible fluid. The pores form a contiguous and interconnected space, so that fluid motion through the matrix is possible (fig. 2.10a). The matrix is incompressible (in the sense that a solid block of the matrix material has an extremely high compression modulus), but can undergo shear deformation. Deformation can change the volume of the pore space, and since the fluid can flow through the matrix, it may be squeezed out of the system as a consequence of deformation. Analogously, if the external pressure on the fluid compartment is increased, fluid will flow into the matrix; in order to accommodate this influx, the matrix must deform (fig. 2.10b). Since the fluid content within a given volume is subject to change under deformation or pressure changes, the material as a whole exhibits characteristics of compressibility despite the incompressibility of both its constituents. Typical examples for poroelastic materials include sponges, soil and rocks.

Application of this concept to biological tissue was suggested by Leiderman et al. [49]. Berry et al. demonstrated poroelastic behavior of a tofu phantom under uniaxial compressive stress via ultrasound elastography [5]. Perriñez et al. demonstrated the feasibility of MR poroelasticity (MRPE) in tofu phantoms [70, 71].

In a biphasic poroelastic medium with incompressible constituent, compressibility only arises through the interaction of the two phases and their relative motion. It can therefore only be observed if the medium is given time to react to external forces. This means that poroelasticity only occurs at low vibration frequencies, whereas medical

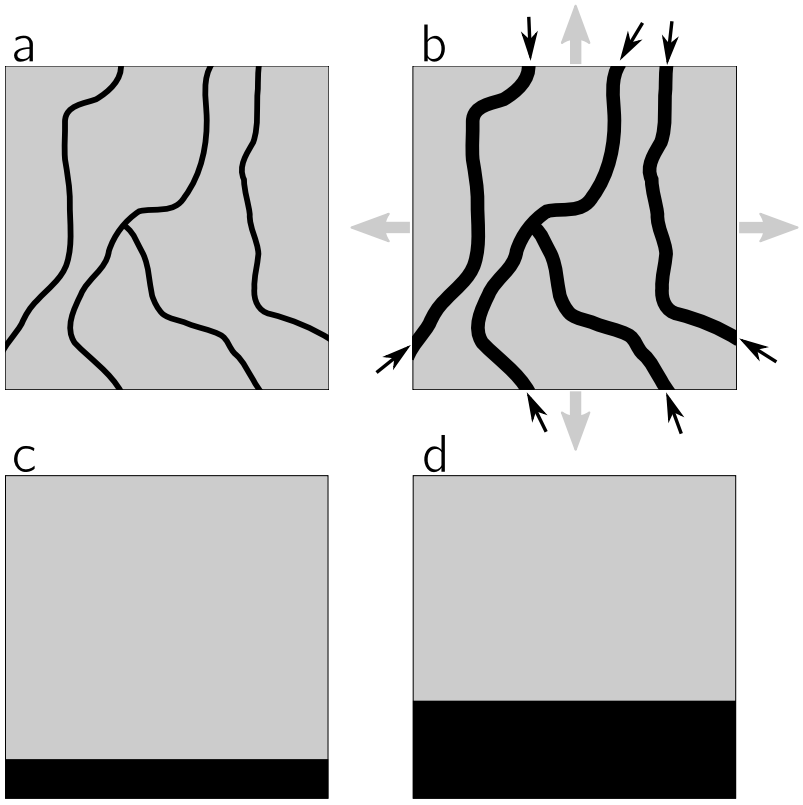

Figure 2.10: Illustration of the poroelastic tissue model. **a**: Equilibrium condition. A volume of brain parenchyma (gray) is permeated by blood vessels (black). **b**: If the pressure inside the vessels increases, fluid is squeezed into the vessels (black arrows), which in turn expand. The constraint of incompressibility of both constituents requires displacement of parenchyma, so that the bulk density remains constant. **c**: MRI cannot resolve structures on sub-voxel length scales; therefore, the model is reduced to the volume fractions of fluid and solid in a given volume element. **d**: An increase in fluid pressure increases the fluid volume fraction and decreases the solid volume fraction.

ultrasound, with frequencies in the megahertz range, is unsuitable to detect poroelastic tissue behavior.

Biot derived equations characterizing the propagation of waves through such a biphasic material [8, 9]. However, the number of independent and unknown parameters of this model renders the numerical solution of the poroelastic wave equation with data obtained from MRE measurements infeasible. However, the the crucial point in Biot's theory is the existence of two distinct longitudinal (pressure) wave modes. These corresponds to in-phase and opposed-phase oscillation of the two compartments. The in-phase mode is the equivalent of a pressure wave in a monophasic medium, which is characterized by high propagation velocity and hence very long wavelengths. The opposed-phase mode propagates at significantly lower velocity and has therefore a much shorter wavelength.

To surmount this challenge, a simplified model can be conceived for the inversion of the wave field. The displacement field can be thought of as the superposition of the solid and the fluid displacement field,

$$\mathbf{u} = f_{\mathrm{M}}\boldsymbol{\sigma}_{\mathrm{M}} + f_{\mathrm{F}}\boldsymbol{\sigma}_{\mathrm{F}}, \tag{2.55}$$

where indices F and M relate to the fluid and the matrix, respectively, and f_S and f_M refer to their volume fractions (the ratios of fluid and matrix volume to the bulk volume). The same superposition then holds for the strain tensor,

$$\boldsymbol{\epsilon} = f_{\mathrm{M}}\boldsymbol{\epsilon}_{\mathrm{M}} + f_{\mathrm{F}}\epsilon_{\mathrm{F}}\,\mathbf{I}, \tag{2.56}$$

with the 3×3 identity matrix $\mathbf{I}$. The solid phase is characterized by a 3×3 tensor

$$\boldsymbol{\epsilon}_{\mathrm{M}} = \frac{1}{2}\left(\nabla\mathbf{u}_{\mathrm{M}} + (\nabla\mathbf{u}_{\mathrm{M}})^{\mathrm{T}}\right) - \frac{1}{3}\nabla\bullet\mathbf{u}_{\mathrm{M}}\,\mathbf{I}, \tag{2.57}$$

whereas the fluid does not support shear strain, so that it is fully characterized by the scalar quantity $\epsilon_{\mathrm{F}} = \nabla\bullet\mathbf{u}_{\mathrm{F}}$.

The total stress in the medium is a weighted superposition of the stresses in the two

phases:

$$\boldsymbol{\sigma} = f_{\mathrm{M}}\boldsymbol{\sigma}_{\mathrm{M}} + f_{\mathrm{F}}\boldsymbol{\sigma}_{\mathrm{F}} \tag{2.58}$$

$$\text{with} \quad \boldsymbol{\sigma}_{\mathrm{M}} = 2\mu\boldsymbol{\epsilon}_{\mathrm{M}} \tag{2.59}$$

$$\text{and} \quad \boldsymbol{\sigma}_{\mathrm{F}} = K\epsilon_{\mathrm{F}}\mathbf{I}. \tag{2.60}$$

μ is the shear modulus of the material, while K is the compression modulus (also referred to as bulk modulus). The stress can be equated with the stress described by Hooke's law in a solid body [47]:

$$\boldsymbol{\sigma} = \mu \cdot \left(\nabla\mathbf{u} + (\nabla\mathbf{u})^{\mathrm{T}} - \frac{2}{3}(\nabla \bullet \mathbf{u})\,\mathbf{I} \right) + K \cdot (\nabla \bullet \mathbf{u})\,\mathbf{I}. \tag{2.61}$$

By substituting the right hand side of eq. (2.61) into the continuous-body formulation of Newton's second law,

$$\rho \frac{\partial^2 \mathbf{u}}{\partial t^2} = \nabla\boldsymbol{\sigma},$$

the dynamic relation between strain and displacement can be expressed as [47, pg. 87]

$$\rho \frac{\partial^2 \mathbf{u}}{\partial t^2} = \mu\left(\nabla^2\mathbf{u} + \frac{1}{3}\nabla(\nabla \bullet \mathbf{u}) \right) + K\nabla(\nabla \bullet \mathbf{u}). \tag{2.62}$$

Note that in the derivation of eq. (2.62) all spatial derivatives of μ and K were neglected, in accordance with the assumption of a homogeneous medium with slow spatial variations of the elastic properties.

For time-harmonic displacements $\mathbf{u} = \mathbf{u}_0(\mathbf{r}) \cdot \exp(\mathrm{i}\Omega t)$, eq. (2.62) can be expressed in matrix form:

$$-\rho\Omega^2\mathbf{u} = \mathbf{A}\begin{pmatrix} \mu \\ K \end{pmatrix}$$

with

$$\mathbf{A} = \begin{pmatrix} \frac{1}{3}\frac{\partial(\nabla\bullet\mathbf{u})}{\partial x} + \nabla^2 u_1 & \frac{\partial(\nabla\bullet\mathbf{u})}{\partial x} \\ \frac{1}{3}\frac{\partial(\nabla\bullet\mathbf{u})}{\partial y} + \nabla^2 u_2 & \frac{\partial(\nabla\bullet\mathbf{u})}{\partial y} \\ \frac{1}{3}\frac{\partial(\nabla\bullet\mathbf{u})}{\partial z} + \nabla^2 u_3 & \frac{\partial(\nabla\bullet\mathbf{u})}{\partial z} \end{pmatrix}.$$

The elastic moduli μ and K can then be recovered by calculating the left pseudo-inverse of $\mathbf{A}$:

$$\begin{pmatrix} \mu \\ K \end{pmatrix} = -\rho\Omega^2 (A^*A)^{-1} A^*\mathbf{u}, \tag{2.63}$$

where the asterisk denotes the conjugate transpose of a matrix. This procedure will

be referred to as *direct inversion*.

The term within the outer parentheses in eq. (2.61) has a vanishing trace, since $\mathrm{tr}(\nabla\mathbf{u}) = \mathrm{tr}\left((\nabla\mathbf{u})^{\mathrm{T}}\right) = \nabla \bullet \mathbf{u}$ and $\mathrm{tr}((\nabla \bullet \mathbf{u})\mathbf{I}) = 3\nabla \bullet \mathbf{u}$. Hydrostatic pressure, on the other hand, is given by $P = -\frac{1}{3}\mathrm{tr}(\boldsymbol{\sigma})$ [47, pg. 6], so that by combining eqs. (2.58), (2.59) and (2.61) we obtain

$$P = -\frac{1}{3}\mathrm{tr}(\boldsymbol{\sigma}) = -K \cdot \nabla \bullet \mathbf{u} = -\frac{1}{3} f_{\mathrm{F}} \cdot \mathrm{tr}(\boldsymbol{\sigma}_{\mathrm{F}}). \tag{2.64}$$

Equation (2.64) states that the pressure caused by dynamic loading of a poroelastic medium is proportional to the volumetric strain of the bulk material, with the compression modulus K as the proportionality constant. All parameters related to internal interaction between the two phases can therefore be replaced with the two effective quantities K and μ. This approach reduces the poroelastic tissue model to an effective medium model that is entirely characterized by those two (potentially complex-valued) quantities, in contrast to the large number of unknown parameters in Biot's original model. The two phases are replaced with a monophasic medium that has both finite μ and K and which will respond to applied oscillating external pressure by adapting its volume, as predicted by eq. (2.53).

2.4.1 Signal equation

The MRI signal is a superposition of all hydrogen atoms within an excited volume, and a decomposition into partial signals from the fluid and solid phase of a poroelastic model is intractable. However, an analysis of the signal equation will reveal that it is possible to garner information about local expansion or compression, assuming that the bulk density of the medium remains constant.

If equal densities $\rho_{\mathrm{M}} = \rho_{\mathrm{F}} = \rho$ for both the matrix (M) and the fluid (F) phase are assumed for a poroelastic model, fluid displacement or influx does not lead to a change of the bulk density, since one material is merely replaced with the other material of the same density. The continuity equation

$$\frac{\partial \rho}{\partial t} + \nabla \bullet \mathbf{j} = 0 \tag{2.65}$$

with mass flux $\mathbf{j}$ therefore reduces to

$$\frac{\partial \rho}{\partial t} = 0 \quad \Rightarrow \quad \nabla \bullet \mathbf{j} = 0. \tag{2.66}$$

MRI does not detect bulk material densities, as it is only sensitive to the proton signal from hydrogen atoms. In the biphasic poroelastic tissue model, each hydrogen atom belongs either to the matrix or to the fluid compartment. Because water content differs between interstitial water and the surrounding tissue matrix, the MRI-relevant partial hydrogen densities ρ_F^{MRI} and ρ_M^{MRI} are distinct. The continuity equation

$$\frac{\partial}{\partial t}\left(\rho_{\mathrm{F}}^{\mathrm{MRI}}+\rho_{\mathrm{M}}^{\mathrm{MRI}}\right)+\nabla\bullet\left(\mathbf{j}_{\mathrm{F}}^{\mathrm{MRI}}+\mathbf{j}_{\mathrm{M}}^{\mathrm{MRI}}\right)=0 \tag{2.67}$$

therefore cannot be simplified to the form of eq. (2.66).

In this model, the total hydrogen density, $\rho^{\mathrm{MRI}}=\rho_{\mathrm{F}}^{\mathrm{MRI}}+\rho_{\mathrm{M}}^{\mathrm{MRI}}$, is not constant with respect to time. Rather, it will change as fluid is squeezed out or drawn into the matrix, changing the relative volumes of matrix and fluid in the overall material. The motion-encoding mechanism deployed in MR Elastography is only sensitive to motion, not to hydrogen density, hence only the hydrogen fluxes $\mathbf{j}_{\mathrm{M}}^{\mathrm{MRI}}$ and $\mathbf{j}_{\mathrm{F}}^{\mathrm{MRI}}$ are detectable. The hydrogen signal from a voxel is measured as a superposition of all spins contained in that voxel and no separation into contributions from the matrix and the fluid is possible. Given this constraint, MRE quantifies the overall hydrogen flux $\mathbf{j}^{\mathrm{MRI}}=\mathbf{j}_{\mathrm{F}}^{\mathrm{MRI}}+\mathbf{j}_{\mathrm{M}}^{\mathrm{MRI}}$ and the continuity equation reads

$$\frac{\partial}{\partial t}\rho^{\mathrm{MRI}}+\nabla\bullet\mathbf{j}^{\mathrm{MRI}}=0. \tag{2.68}$$

This implies that finite hydrogen fluxes are observable if the two compartments possess different hydrogen densities, such that $\frac{\partial\rho^{\mathrm{MRI}}}{\partial t}\neq 0$. In that case, signals from inward and outward mass fluxes – even though perfectly balanced in terms of mass density – will not fully cancel out, resulting in a phase signal indicative of the motion of the compartment with the higher hydrogen density. The divergence of the hydrogen flux is therefore an indicator of local compression or dilatation. Time-harmonic pressure fields will be used in this work to generate oscillating displacement fields, and the magnitude $\left|\nabla\bullet\mathbf{j}^{\mathrm{MRI}}\right|$ will be analyzed as a measure of local compressibility. To be consistent with the nomenclature established in the MRE community, $\mathbf{j}^{\mathrm{MRI}}$ will be referred to as the *displacement field* $\mathbf{u}$.

In general, the MRI signal measured by the receive coil(s) is a complex function of time and space and can therefore be expressed as $S(\mathbf{r},t)=S_0(\mathbf{r})\cdot\exp(\mathrm{i}\phi(t))$. We will now analyze the signal equation for the signal from the spins within one given voxel

at position $\mathbf{r} = \mathbf{r}_0$ at the time of the signal readout, $t = t_0$, and will therefore drop the explicit references to $\mathbf{r}$ and t.

The signal from the voxel can be described as the superposition of the signals $S_c = |S_c| \cdot \exp(\mathrm{i}\phi_c)$, where $c \in \{1,2\}$ iterates over the two compartments of the poroelastic model. The compound signal is therefore

$$S = |S| \cdot \exp(\mathrm{i}\phi) = S_1 + S_2 = |S_1| \cdot \exp(\mathrm{i}\phi_1) + |S_2| \cdot \exp(\mathrm{i}\phi_2). \tag{2.69}$$

A trigonometric analysis of these vectors (fig. 2.11) yields

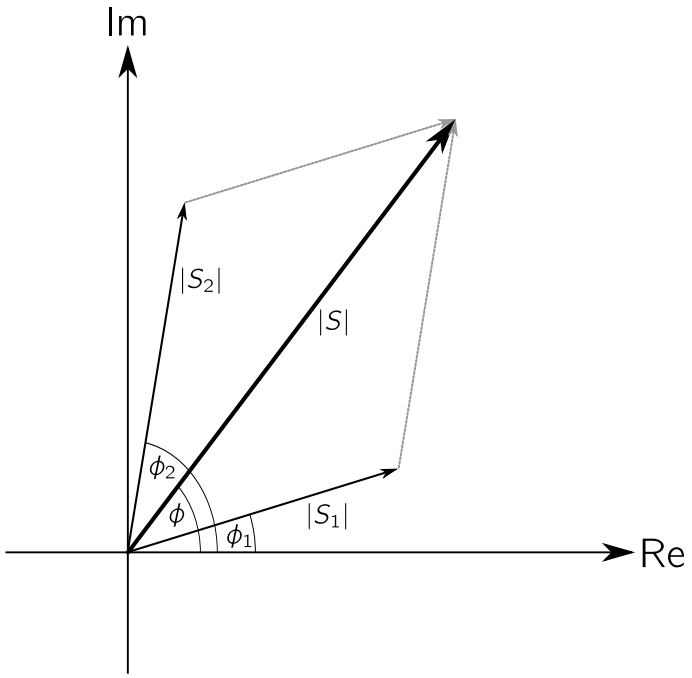

Figure 2.11: The detected MRE signal in a biphasic poroelastic model. The contributions $S_1 = |S_1| \cdot \exp(\mathrm{i}\phi_1)$ and $S_2 = |S_2| \cdot \exp(\mathrm{i}\phi_2)$ from the two compartments sum to form the combined signal $S = |S| \cdot \exp(\mathrm{i}\phi)$.

$$|S| = \sqrt{|S_1|^2 + |S_2|^2 - 2|S_1||S_2| \cdot \cos(\phi_2 - \phi_1)} \tag{2.70}$$

$$\phi = \phi_1 + \arcsin\left(\frac{|S_2|}{\sqrt{|S_1|^2 + |S_2|^2 - 2|S_1||S_2| \cdot \cos(\phi_2 - \phi_1)}} \right). \tag{2.71}$$

The signal amplitudes $|S_1|$ and $|S_2|$ are determined by three factors: the hydrogen densities ρ_c^{MRI} in the two compartments, the volume fraction f_c that each compartment occupies in a voxel, and the signal decay between excitation and readout. The former

two are intrinsic properties of the medium and differ between parenchyma, blood and cerebro-spinal fluid. Signal decay is characterized by the T_2 decay constant of the respective compartment and the echo time TE of the MR sequence. The signal amplitudes can therefore be expressed as

$$|S_c| \propto \rho_c^{\mathrm{MRI}} f_c \cdot \exp\left(-\frac{TE}{T_{2,c}}\right). \tag{2.72}$$

The requirement that bulk tissue density remain constant (a consequence of the assumption of equal densities of the two phases and their incompressibility) dictates that displacement of one phase is compensated by an opposite displacement of the other phase. However, this displacement can only be detected if the two phases differ in their signal intensities. This is the case if the compartments have dissimilar water content, so that $\rho_1^{\mathrm{MRI}} \neq \rho_2^{\mathrm{MRI}}$, or if their T_2 relaxation times differ significantly. In that case, parts of the measured signal phase cancel out, and the resultant signal is representative of the motion of the phase with the higher signal intensity.

This motion (influx or efflux) may take place in any of the three Cartesian directions, as the displacement field divergence combines information about motion in all directions. For example, matrix motion along one axis can be compensated by fluid motion in the orthogonal plane. It is therefore crucial to acquire three linearly independent projections of the displacement field $\mathbf{u}$.

3 Technical developments

3.1 Overview

All experiments described in this work were performed on a Siemens Magnetom Sonata 1.5 Tesla clinical MR scanner (Siemens Healthcare, Erlangen, Germany). Two different custom-built setups were employed for the generation of mechanical vibrations. The first setup was comprised of a waveform generator (AFG 3021, Tektronix, Beaverton, OR, USA), a commercial audio amplifier (PA-1600-X, LD Systems, Neu-Anspach, Germany) and a car subwoofer. The second layout consisted of an actuator (SPL Spindel und Präzisionslager GmbH, Ebersbach, Germany) driven by a piezoceramic stack (Piezosystem Jena GmbH, Jena, Germany) and an integrated waveform generator/amplifier (CGC instruments, Chemnitz, Germany). Both setups were capable of providing oscillation amplitudes on the order of 2 mm in the frequency range between 20 and 70 Hz.

The MR sequence controls all steps and components involved in the acquisition of images on the MR scanner[1]. Additionally, it communicates with the mechanical actuation hardware to guarantee synchrony between vibration and image acquisition. Prior to the developments described in this work, MR sequences based on FLASH (fast low angle shot, [86,95]) and bSSFP (balanced steady state free precession, [41,84]) were utilized. These approaches all require several excitation → motion-encoding → readout cycles to obtain an image of a single slice. Given the high demands of compression-sensitive MRE (multiple slices, three projections of the displacement field, preferably eight wave phases), those sequences would lead to measurement times unacceptably long for studies on volunteers or patients. A faster imaging method was therefore required. Uses of single-shot EPI sequences for MRE had been published before [32,45,79], but they were limited to low spatial resolutions (or small

[1] In the context of MRI, "sequence" can refer either to the timing of events (RF pulses, gradients, signal sampling, etc.), or to the software implementing the execution of such a timing on the scanner. In this section, the latter meaning is implied.

fields of view) and were not widely adapted for diagnostic purposes. Therefore, the development of a new and improved version of a motion-sensitized single-shot EPI sequence was the first part of the work described in this thesis.

Since its first clinical application in 1983 [85], single-shot EPI has become an indispensable instrument in clinical imaging routine [75]. Its major advantage over most other MR sequences is its capability to acquire a full image within a few tens of milliseconds. Typical applications include demand for short scan times, imaging of moving organs (for example in cardiac imaging) and high-temporal-resolution imaging (functional MRI). Compression-sensitive MRE requires 3D coverage of the volume of interest. A typical protocol comprises 30 slices, three projections of the displacement field and eight vibration phases, amounting to 720 wave images per vibration frequency. The following section describes an EPI sequence designed specifically for this MRE application; it could also be adapted to future studies or to clinical applications requiring the fast detection of compression-related displacements.

3.2 EPI sequence

The Siemens MRI scanners used in this work implement an MRI sequence[2] as a compiled binary library file containing machine-readable instructions to control the scanner gradient system, the radiofrequency system, and the analog-to-digital converters. The user can interact with the sequence on the scanner console (“host”) via a graphical user interface (GUI) and modify a number of measurement parameters. The sequence calculates the timing of RF pulses, gradient pulses, data acquisition, and idle times. The corresponding instructions are executed on the scanner CPU, which in turn addresses the hardware components. These sequences are written in C++ and implement a set of standardized interface functions. Due to nondisclosure agreements, implementations details and code excerpts cannot be presented in this thesis. However, the principles of the sequence implementation developed for compression-sensitive MRE are outlined below.

The standard Siemens general-purpose spin echo EPI sequence was used as the starting point for the development that forms the basis of this work. It was then modified to include motion-encoding gradients (MEGs) with 0^{th}, 1^{st} and 2^{nd} order moment nulling, initial TTL (transistor-transistor logic) trigger pulses to start the vibration,

[2]The piece of software implementing a timing sequence is also referred to as a "sequence".

and user-selectable settings for the motion-encoding gradient amplitude and duration, motion-encoding directions, and the number of wave phases to acquire. The number of MEG cycles is set according to the following algorithm: First, the shortest possible sequence timing is calculated, based on the desired EPI readout duration, as shown in fig. 2.4. This duration is primarily dependent on the desired image size, resolution, and readout gradient performance. The readout train starts immediately after the 180° RF pulse, and the time from this refocusing pulse to the readout of the central k-space line defines the second half of the echo time, $TE/2$. Due to the inherent symmetry of spin echo sequences, the initial 90° and 180° pulses must also have a temporal separation of $TE/2$. This leaves an empty time slot between those two pulses. The duration t_{MEG} of that time slot is queried after the sequence timing has been calculated. The number of MEG cycles is then calculated as the maximum number of MEG repetitions (at the user-defined MEG period T) fitting into the slot:

$$n_{\mathrm{cycles}} = \mathrm{floor}\left(\frac{t_{\mathrm{MEG}}}{T}\right) \tag{3.1}$$

If second-order gradient moment nulling is selected by the user, n_{cycles} has to be an even number, so n_{cycles} is reduced by one if it is odd. The number of MEG cycles is automatically indicated in the graphical user interface.

3.2.1 SmartTrigger

To facilitate measurements at different vibration frequencies, a TTL-based communication protocol was developed in cooperation with the manufacturer of the integrated waveform generator/amplifier (CGC instruments, Chemnitz, Germany). The waveform generator can store up to 100 *measurements*. Each measurement is defined by its vibration waveform (usually a sinusoid, but arbitrary waveforms are possible), the amplification level, the duration of the waveform and the number of repetitions of the waveform after each trigger pulse (*number of bursts*). The measurements are identified by a numerical index between 0 and 99.

The MR sequence can select any of these measurements by means of a specifically designed trigger pulse. A conventional TTL trigger pulse to initiate a vibration burst has a duration of 10 microseconds. The waveform generator measures the duration Θ of the TTL pulse before reacting to it. If the pulse duration exceeds a threshold of 15 µs, it is interpreted as a *SmartTrigger* pulse. The waveform generator decodes the

index n of the measurement from the duration Θ according to

$$n = \text{floor}\left(\frac{\Theta - 15\,\mu\text{s}}{10\,\mu\text{s}}\right) \tag{3.2}$$

and loads the corresponding settings into its memory. On the sequence side, the index is encoded into the SmartTrigger pulse duration as

$$\Theta = 20\,\mu\text{s} + n \cdot 10\,\mu\text{s}. \tag{3.3}$$

Note that the offsets are different in eqs. (3.2) and (3.3) (15 µs vs. 20 µs), adding tolerance for error. For example, the scanner would encode the measurement index $n = 1$ as $\Theta = 20\,\mu\text{s} + 1 \cdot 10\,\mu\text{s} = 30\,\mu\text{s}$, whereas any pulse duration $25\,\mu\text{s} \leq \Theta < 35\,\mu\text{s}$ would be decoded to $n = 1$ by the amplifier, adding an error margin of 5 µs in both directions. In the graphical user interface on the MR scanner, the user can select up to eight different MEG and vibration frequencies that are measured in succession, and *SmartTrigger* pulses are deployed to toggle the pre-configured measurements on the waveform generator. This mechanism allows for automated acquisitions at different vibration frequencies and reduces the likelihood of user errors, particularly in more time-constrained clinical settings.

4 Experiments

4.1 Overview

Two different models were contrived to elucidate different aspects of compressibility of organic tissue. The first model, *isolated gas-filled cavities* (IGC), comprises small spherical gas-filled cavities that are embedded in a stiff matrix. Although this is not a true poroelastic system due to the pore space not being interconnected, the gas allows for compression of the system, thus facilitating the evaluation of the displacement field divergence as a marker of volumetric strain. The second model, *vascular soft tissue* (VST), was inspired by the architecture of many biological organs, with liquid-filled vessels (blood or cerebro-spinal fluid) permeating a bulk of soft parenchyma. Biot's poroelastic theory is fully applicable to this model.

A number of experimental studies were conducted as part of this work in order to assess the feasibility and the diagnostic potential of compression-sensitive MR Elastography. Since no earlier work existed on that topic, the first experiments to assess the newly developed EPI sequence and the displacement field divergence as a compression-sensitive entity were performed on phantoms. In medical imaging terminology, phantoms are simple model systems devised to isolate a certain aspect of the characteristics of a biological system to evaluate the feasibility of a novel method. Once initial phantom experiments are considered successful, experiments on more complex model systems or on living tissue can be carried out.

The most common type of phantom in MR Elastography comprises water with an addition of small amounts of agarose (on the order of 0.5–5 percent by mass). Agarose powder dissolved in hot water solidifies into a stiff gel upon cooling and can be cast into arbitrary forms. Such phantoms are widely used as elastic systems with low viscosity, rendering them suitable for shear wave Elastography experiments. However, due to their high water content and the strongly restricted mobility of water

molecules resulting from the tight agarose network, solid agarose gel is almost incompressible. To convert agarose gel into a compressible medium of the IGC model type, gas-filled cavities were introduced. Two studies were performed on such compressible gel phantoms. The first study examined the behavior of volumetric strain in a phantom at different levels of external air pressure. The second study focused on analyzing the effect of gas content on compressibility and comparing MRE results with data obtained from rheometer experiments.

Results from the phantom studies were found to be encouraging, therefore the next step was to perform a similar set of experiments on healthy volunteers. The human lung was considered to be the organ with the closest structural resemblance to the phantoms, with a stiff but deformable matrix and interconnected air-filled spaces. However, the lung is among the most challenging organs in terms of MR imaging. Firstly, the low bulk density of lung parenchyma provides only a very low signal-to-noise ratio (SNR), often requiring extensive signal averaging to obtain acceptable image quality. Secondly, the large tissue-air surface area gives rise to severe distortions of the static magnetic field due to discontinuities of the susceptibility distribution, causing very short apparent relaxation times. Despite these difficutlies, the aim of the study was to to assess whether alterations of tissue elastics induced by different respiratory states would be reflected in MRE-derived oscillating volumetric strain amplitudes.

Since the IGC model is not an appropriate description for organs other than the lung, the VST model was used as a more realistic approximation in a series of phantom and in vivo experiments. The human liver became the next organ of interest for compression-sensitive MRE. Conventional MRE of the liver has become an important clinical procedure and can replace biopsy as a non-invasive diagnostic tool for liver fibrosis. In addition, hepatic portal hypertension (elevated blood pressure in the portal vein supplying the liver) is another indicator for risk of complications and can thus far only be quantified intra-surgically via a catheter. It can cause severe or even fatal complications as a consequence of internal bleeding. It originates from pressure regulation abnormalities in the liver, often caused by liver fibrosis. Any correlation between portal pressure and MRE-derived parameters would be highly valuable as a method for non-invasive pressure assessment. To investigate this potential application of compression-sensitive MRE, an excised sheep liver was used as a phantom, and portal pressure was simulated by attaching a tube to the portal vein and applying

varying levels of water pressure.

The measurement of brain stiffness is another important application of MRE. While shear-wave based MRE has been applied in numerous studies to elucidate pathological changes associated with different neurological diseases, compressibility of the brain has thus far been of minor interest.

The transit of the cardiac pulse wave through the large blood vessels in the human brain causes a periodic macroscopic shifting motion of brain parenchyma. According to poroelastic theory, an expansion of blood vessels would have to be compensated by a displacement of brain parenchyma. Based on this assumption, a study was carried out to assess the feasibility of intrinsic excitation, with the external vibration being replaced by the cardiac pressure wave traveling through the brain and causing local volumetric strain in healthy volunteers.

4.2 Determination of the gradient coordinate system

Calculation of spatial derivatives of the displacement field requires knowledge of the polarity of the motion-encoding gradients (MEGs). The direction of the MEGs is determined by the geometry of the imaging slice. However, if the slice-select gradient is aligned with the z-axis, it remains to be clarified if that gradient causes an increase or a decrease of the total magnetic field strength along the positive z direction.

Image data is represented in a patient-centered coordinate system defined by the DICOM (Digital Imaging and Communications in Medicine) standard as follows:

- x-axis: right $\rightarrow$ left
- y-axis: anterior (front) $\rightarrow$ posterior (back)
- z-axis: inferior (feet) $\rightarrow$ superior (head)

These directions constitute a right-handed coordinate system aligned with the patient inside the scanner and information about image orientation can be obtained from the header of the DICOM files produced by the scanner. However, the actual gradient polarity is not evident from these data. Assuming an incorrect MEG polarity

for one Cartesian axis will produce an incorrect sign for spatial derivatives along that axis. The divergence of the displacement field is calculated according to

$$\nabla \bullet \mathbf{u} = \frac{\partial u_x}{\partial x} + \frac{\partial u_y}{\partial y} + \frac{\partial u_z}{\partial z}. \tag{4.1}$$

If one or two of the spatial derivatives have an incorrect sign, a physically meaningless quantity will be calculated instead of volumetric strain.

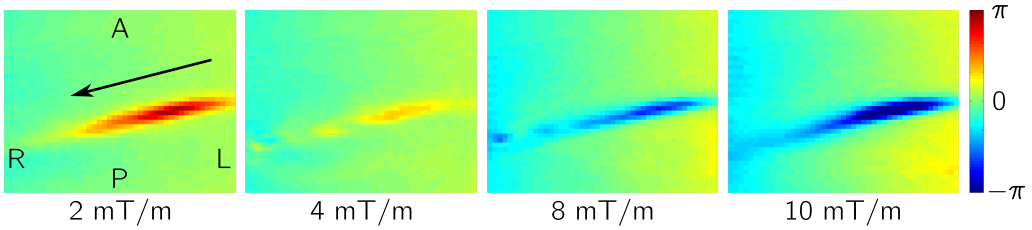

Figure 4.1: Phase images of a flow phantom at different strengths of the motion-encoding gradient. The imaging plane is transverse, i.e. orthogonal to the z-axis of the scanner. Following radiological practice, the directions are indicated as perceived by a subject lying on the back with the feet pointing toward the observer. A: anterior (front), P: posterior (back), L,R: left/right (note that these are relative to the subject, not to the observer). The black arrow indicates the direction of flow.

To determine gradient polarities, a calibration experiment was performed on a flow phantom. A one liter PE bottle was equipped with hose fittings at the top and bottom to which a flexible tube could be attached. The tube was connected to a centrifugal pump capable of providing constant and pulsating flow (Zentrifugalpumpe MultiFlow, GAMPT mbH, Merseburg, Germany), such that a closed circuit was formed. The bottle and tube were filled with water and care was taken to remove any residual air from the system. The bottle was placed inside the MRI scanner in such a way that the direction of flow inside the bottle (from the cap to the outlet close to the bottom) was aligned with the z-axis (head–feet) of the scanner. The pump was operated in constant flow mode and MRE images were acquired with the motion-encoding gradients parallel to the flow direction. The MEG amplitude was increased in four steps from 2 to 10 mT/m. The resulting phase images are shown in fig. 4.1. For a low MEG amplitude of 2 mT/m, the positive phase in the flow region is an effect of the imaging gradients, which are not flow-compensated. As the MEG amplitude increases, its effect becomes stronger and finally dominates over the other gradients. It is obvious that flow from left to right is encoded with a negative phase. Similar experiments were

conducted with flow along the other two axes (anterior→posterior and feet→head) by rotating the bottle.

4.3 Isolated gas-filled cavities model: Phantoms

The content of this chapter was published in [34].

4.3.1 Background

As a first assessment of the sensitivity of MRE to volumetric strain, experiments were performed on a set of phantoms consisting of agarose gel interspersed with gas-filled cavities. Whereas a solid slab of agarose gel would have a compression modulus comparable to that of water (in the range of 2.2 GPa and hence far beyond the detectability limit of MRE), gas-filled inclusions with elastic walls are compressible and therefore cause a reduction of the compression modulus of such a biphasic material. However, Biot's theory of poroelasticity is based on the assumption of an interconnected pore space, through which the fluid phase can flow as the medium is deformed. Consequently, an alternative model is necessary for the description of gas bubbles trapped in a stiff matrix. Such models were suggested by Woods [101] and Chambré [12]. According to their works, a mixture of two phases, 1 and 2, with compression moduli K_1 and K_2 and volume fractions β and $1-\beta$, respectively, possesses a compression modulus

$$\frac{1}{K} = \frac{\beta}{K_1} + \frac{1-\beta}{K_2}. \tag{4.2}$$

If we associate phase 1 with the gas and phase 2 with the gel, the parameter β, i.e. the ratio of the gas volume to the total volume of the medium, is referred to as *porosity*, and, according to the ideal gas law, the compression modulus of the gas is equal to its internal pressure, $K_1 = P$.

For practical purposes, it is advantageous to replace the porosity with the bulk density ρ, since this quantity is more readily accessible in experiments. Assuming the gas density to be negligible compared to the density of the pure matrix material, ρ_M, the bulk density is given by $\rho = (1-\beta)\rho_\mathrm{M}$. Equation (4.2) can thus be re-parametrized as

$$K = \frac{K_\mathrm{M} \cdot P}{\left(1-\frac{\rho}{\rho_\mathrm{M}}\right) K_\mathrm{M} + \frac{\rho}{\rho_\mathrm{M}} P}, \tag{4.3}$$

where K_M is the compression modulus of the pure matrix material. K quantifies the response of the effective medium to deformation in a static (or quasi-static) setting,

whereas dynamic stress is governed by $M = K + \frac{4}{3}\mu$ with shear modulus μ (see section 2.3.4).

4.3.2 Materials and methods

Gel phantoms with gas-filled spherical inclusions were created for a series of experiments. The matrix comprised a mixture of a water-agarose solution (1–1.5 % agarose by mass) with 25 % ultrasound gel. The latter is a highly viscous gel that is usually applied to the patient's skin to improve the coupling of ultrasonic waves into the body during clinical examinations. It retains its physical properties even at elevated temperatures and served as a thickening agent to trap gas bubbles in the medium during solidification of the agarose gel. Water and ultrasound gel were first heated above 90°C. Agarose was then added, and the mixture was stirred until the agarose was fully dissolved. The solution was poured into appropriately shaped vessels and left to cool. Two different methods of introducing gas were employed. In the first experiment, air was injected through a syringe into the viscous fluid and dispersed by manual stirring. For the second experiment, sodium bicarbonate ($NaHCO_3$) and citric acid ($C_6H_8O_7$) were added to the gel once the mixture had reached 50°C in order to produce carbon dioxide (CO_2) according to the following reaction:

$$3\,NaHCO_3 + C_6H_8O_7 \longrightarrow C_6H_5Na_3O_7 + 3\,H_2O + 3\,CO_2.$$

The carbon dioxide was trapped in the viscous gel and formed homogeneously dispersed small bubbles. Phantoms were left to solidify over night and experiments were performed the next day. Rheometer and MRE experiments were performed on such phantoms to assess their mechanical properties.

Rheometer experiments

A total of 23 phantoms with bulk densities in the range from 0.69 to 1.0 g/cm^3 were cast in a cylindrical PVC vessel 5 cm in diameter and 8 cm in height. The rheometer (Physica MCR 301, Anton Paar, Vienna, Austria) was operated in uniaxial strain mode. Pressure was applied to the top surface of the phantoms via a circular plate. The counterforce exerted by the phantom during compression was recorded as a function of the volumetric strain. The compression modulus could then be calculated from linear fits to the resultant force versus strain data.

MRE experiments

The MRE experiment comprised two parts. Firstly, a single phantom was produced in a cylindrical container 6 cm in diameter by the air injection method . The container was sealed to be air-tight and positioned in the head-rocker unit of the human MRE setup. The container was connected to an air pressure system capable of delivering up to 4.8 bar of pressure. The phantom was vibrated at a frequency of 50 Hz. A total of 25 transverse slices were acquired at a spatial resolution of $1.5 \times 1.5 \times 1.5$ mm^3 with an echo time of 75 ms and a repetition time of 210 ms. Signal averaging over two identical measurements was performed to improve the signal-to-noise ratio. An MEG with first gradient moment nulling, an amplitude of 20 mT/m and a period of 20 ms was deployed, and eight phases of the vibration cycle were recorded. Between measurements, the air pressure was increased from 0 to 4.8 bar in steps of 0.5 bar and then reduced in steps of 1 bar back to atmospheric pressure. In the post-processing, phase data from each measurement was temporally Fourier-transformed and the 50 Hz component was filtered with a $5 \times 5 \times 5$ Gaussian kernel. Finally, the displacement field divergence was calculated and averaged over a region of interest encompassing the cross-section of the phantom without its boundaries.

For the second part of the MRE experiment, three larger phantoms (6 cm diameter, 20 cm length) were prepared using the CO_2-producing reaction. They were placed side-by-side in a tray, which was inserted into the head rocker unit built for cerebral MRE examinations, as illustrated in fig. 4.2.

The setup was placed inside the head coil of a clinical 1.5 Tesla MR scanner. The head cradle was connected to the piezo-based vibration generator at the end of the patient table via a carbon fiber rod. The phantoms were subjected to 50 Hz vibrations at different amplitudes. MRE images were acquired using the motion-sensitized EPI sequence discussed in section 3.2. The spatial resolution was $2 \times 2 \times 2$ mm^3. Thirty adjacent slices, eight wave phases and three orthogonal projections of the displacement field were measured. The field of view was 128×80 mm^2 with an echo time and repetition time of 55 ms and 176 ms, respectively. The vibration amplitude was increased from 5 % to 30 % amplifier output level in steps of 5 % in successive measurements. The motion-encoding gradient comprised one cycle of a waveform with first-order gradient moment nulling, a duration of 11.6 ms, corresponding to a frequency of 86 Hz and an amplitude of 8 mT/m. Each measurement was repeated with inverted MEG and vibration waveforms to suppress motion-encoding contributions

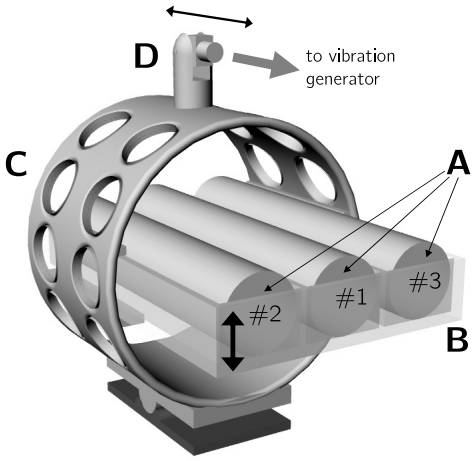

Figure 4.2: Setup of the MRE experiment on IGC-type phantoms with varying gas content. The three cylindrical phantoms (A) were placed in a tray (B), which in turn was inserted into the head rocker unit (C). The vibration generator was mounted at the end of the patient table (not shown) and connected via a carbon fiber rod to the cylinder (D) on top of the rocker. The direction of the motion produced by the vibration generator is indicated by the thin arrow, and the resultant vibratory excitation of the phantoms by the thick black arrow.

from the imaging gradients. The imaging gradients retained their original polarity in the second scan, such that their motion-encoding contribution changed sign as the vibration was inverted. On the other hand, inverting both the vibration and the MEG polarity had no effect on the MEG contribution to the phase images. Therefore, taking the average of two such scans canceled out all effects that were not caused by the MEG.

Volumetric strain $|\nabla \bullet \mathbf{u}|$ was calculated as the sum of the three axial derivatives according to eq. (4.1). Spatial derivatives of the raw MRI phases were calculated by

$$\frac{\partial \phi_j}{\partial r_j} = -\mathrm{Im}\left\{\exp(-\mathrm{i}\phi_j)\cdot\frac{\partial}{\partial r_j}\exp(\mathrm{i}\phi_j)\right\}, \tag{4.4}$$

where Im denotes the imaginary part of a complex number and ϕ_j is the MR signal phase accumulated through projection of the oscillation onto the j^{th} Cartesian axis. To increase noise robustness of the calculation, a three-dimensional averaging differ-

ence scheme [2] was used:

$$\frac{\partial \phi_1(\mathbf{r})}{\partial r_1} = \frac{1}{p(2p+1)^2} \sum_{m=-p}^{p} \sum_{n=-p}^{p} \sum_{k=1}^{p} \frac{\phi_1(\mathbf{r}+k\cdot\mathbf{v}_1+m\cdot\mathbf{v}_2+n\cdot\mathbf{v}_3)-\phi_1(\mathbf{r}-k\cdot\mathbf{v}_1+m\cdot\mathbf{v}_2+n\cdot\mathbf{v}_3)}{2k\cdot|\mathbf{v}_1|}, \tag{4.5}$$

where $\mathbf{r}$ is the discrete voxel location and $\mathbf{v}_i$ $(i = 1,2,3)$ are the vectors connecting adjacent voxels along the Cartesian axes. Equation (4.5) prescribes averaging central differences with a maximum distance of $2p+1$ along the x-axis, with additional averaging of those central differences along the other two axes. Derivatives along the y- and z-direction can be calculated correspondingly. Since discrete derivatives are known to be sensitive to noise, numerical simulations were performed to quantify the impact of noise in the recorded displacement field data on the reconstructed compression moduli.

4.3.3 Results

MRE air pressure experiment

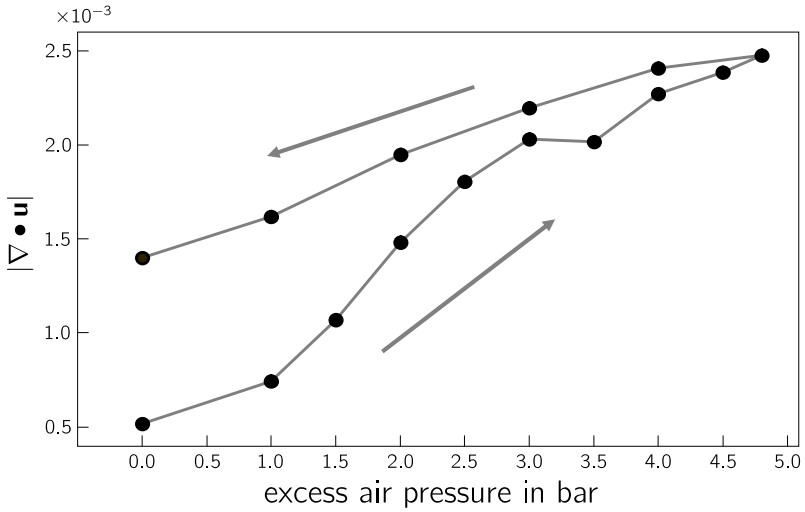

Figure 4.3: Average volumetric strain in the IGC-type phantom at different levels of external air pressure. The arrows indicate the course of the experiment.

As shown in fig. 4.3, volumetric strain $|\nabla \bullet \mathbf{u}|$ increased with increasing air pressure. Arrows indicate the temporal course of the experiment, during which the air pressure was first increased in steps from atmospheric pressure to 4.8 bar excess pressure, followed by a series of steps with decreasing pressure. As the pressure was reduced, $|\nabla \bullet \mathbf{u}|$ decreased, but at a slower rate than on the rising path. As a result, volumetric

strain at atmospheric pressure in the last measurement was larger than in the first measurement of the experiment.

Rheometer experiments

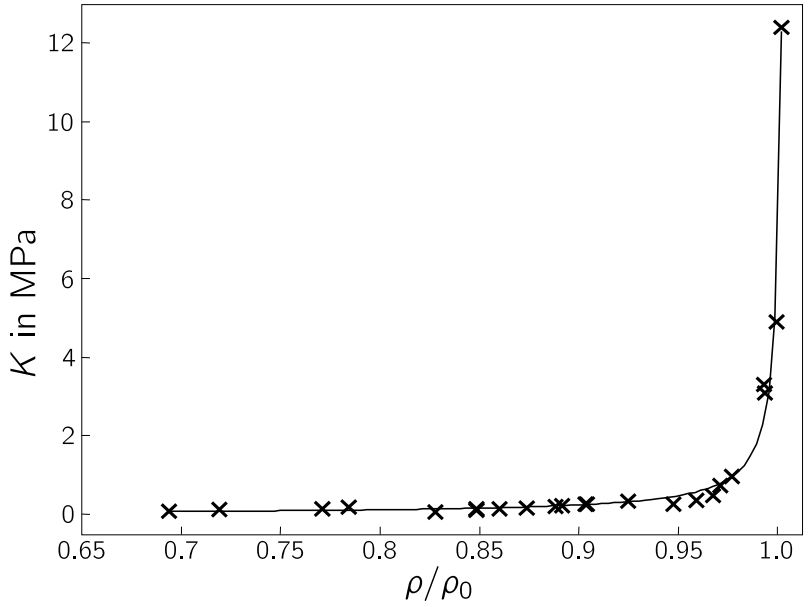

Figure 4.4: Rheometer-derived compression moduli K in 23 IGC-type phantoms as a function of density. The solid line is a fit of eq. (4.3) to the data.

The compression moduli of the 23 phantoms examined with the rheometer are plotted in fig. 4.4 as a function of the phantom density. A least-squares fit of eq. (4.3) yielded the following values: $P = 26 \pm 2$ kPa for the intra-cavity gas pressure, $K_M = 6.5 \pm 0.2$ MPa for the compression modulus, and an additive offset of -10 kPa to account for a noise-induced shift of the baseline.

MRE porosity experiment

The three phantoms used in the second part ot the MRE experiment had bulk densities of 0.95 g/cm^3 (#1), 0.94 g/cm^3 (#2) and 0.89 g/cm^3 (#3). Using eq. (4.3) and the material parameters obtained from the rheometer study, the predicted values of the compression modulus K of the three phantoms are 472 ± 9 kPa (#1), 397 ± 9 kPa (#2) and 217 ± 8 kPa (#3).

Figure 4.5 shows transverse slices through the phantoms with proton density (PD) and T_2-weighted contrast, as well as maps of the shear and volumetric strain amplitudes. Dark spots in the PD and T_2-weighted images indicate reduced signal intensity due to the presence of gas. Bright spots in the T_2 image designate regions with free

water, thereby suggesting that some of the cavities were partially or completely filled with water drained from the surrounding matrix, especially in phantom #2. These images illustrate the porosity increasing from phantom #1 to #3. The maps of volumetric strain, $|\nabla \bullet \mathbf{u}|$, clearly show a correlation between phantom stiffness and strain amplitude. Furthermore, the spatial correlation between porosity and volumetric strain amplitude can be observed clearly in phantom #3, where high strain occurred in regions of high porosity (i.e. with low signal levels in PD and T_2-weighted images). Similar findings are not reproduced by the shear strain maps ($\nabla \times \mathbf{u}$), where patterns emerge that do not appear to be correlated with the porosity distribution.

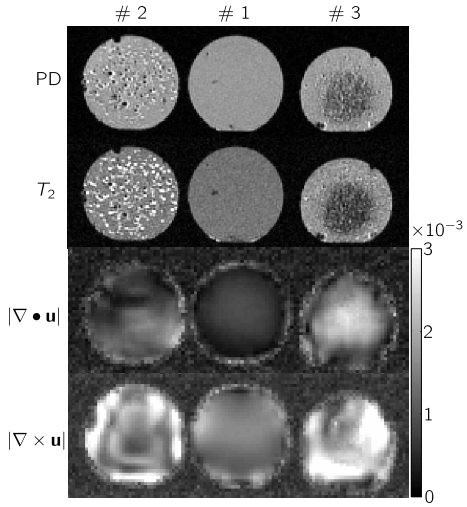

Figure 4.5: Transverse slice through the three IGC-type phantoms examined with MRE. The upper two rows present proton density (PD) and T_2 contrast. Gas-filled cavities are visible as hypointense spots. Bright speckles in the T_2-weighted images indicate the presence of free water, suggesting that some of the cavities are partially or completely filled with water drained from the surrounding gel. The two bottom rows show the shear ($|\nabla \times \mathbf{u}|$) and volumetric strain ($|\nabla \bullet \mathbf{u}|$) induced by harmonic vibrations.

Averaged volumetric and shear strain amplitudes as a function of the amplifier output level are shown in fig. 4.6. Volumetric strain increased monotonously with amplifier amplitude and was always higher in the softer phantoms than in the stiffer ones. This permits a clear delineation of the three phantoms based on their porosity. In the case of shear strain, on the other hand, an increase in strain amplitudes with the vibration strength is observable, but the correlation with phantom porosity is not present.

Quantitative assessments of the P-wave modulus $|M|$ and shear modulus $|\mu|$ was performed by taking the absolute value of eqs. (2.50) and (2.51). The nominator and

Phantom #	Density ρ in g/cm^3	$\|K\|$ in kPa (predicted)	$\|\mu\|$ in kPa	$\|M\|$ in kPa
1	0.95	472 ± 9	8.6 ± 0.3	10.3 ± 0.3
2	0.94	397 ± 9	2.8 ± 0.5	7.0 ± 0.9
3	0.89	217 ± 8	3.4 ± 0.4	5.1 ± 0.5

Table 4.1: Compilation of the results from the MRE experiment on IGC-type phantoms with varying gas content. The compression modulus $|K|$ was predicted from the results of the rheometer experiments, using phantom density ρ as the predictor. Shear modulus $|\mu|$ and P-wave modulus $|M|$ were calculated from the MRE displacement data.

denominator of these equations, averaged over a region of interest, are plotted in fig. 4.7. $|M|$ and $|\mu|$ were obtained by scaling the slope of linear fits to the data with $\rho\Omega^2$ ($\Omega = 2\pi \cdot 50$ Hz). $|\mu|$ was calculated as 8.6 ± 0.3 kPa (#1), 2.8 ± 0.5 kPa (#2) and 3.4 ± 0.4 kPa (#3) for the three phantoms. The corresponding values for $|M|$ were 10.3 ± 0.3 kPa (#1), 7.0 ± 0.9 kPa (#2) and 5.1 ± 0.5 kPa (#3). All measured and calculated properties of the three phantoms are summarized in table 4.1.

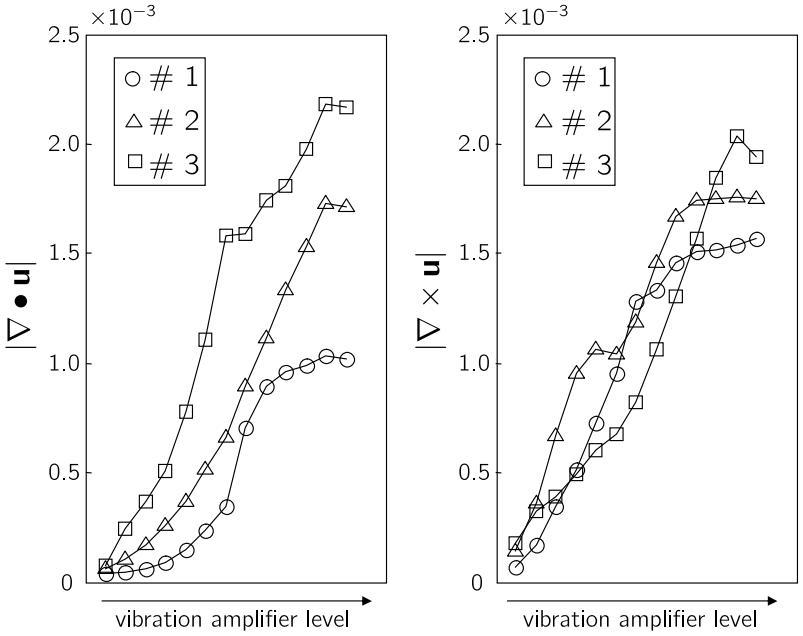

Figure 4.6: Volumetric (left) and shear strain (right) amplitudes in the three IGC-type phantoms as a function of the amplifier output level.

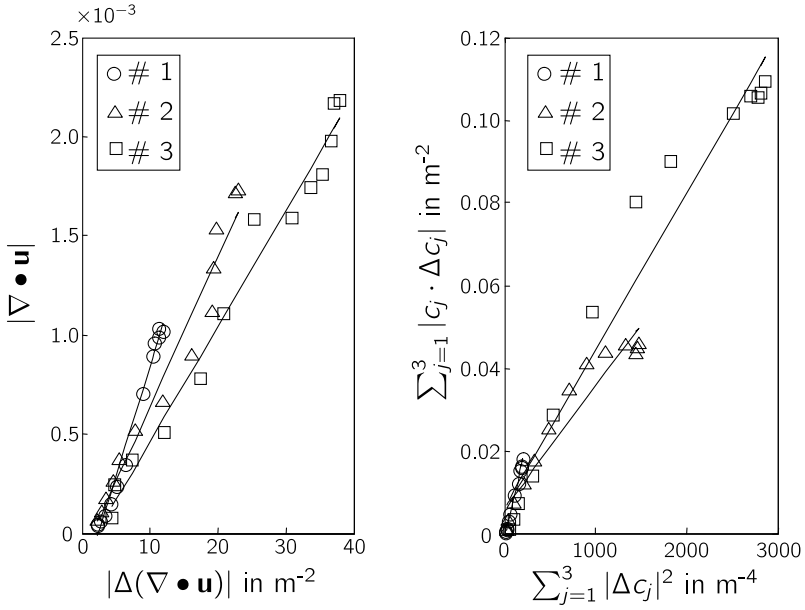

Figure 4.7: The averaged magnitudes of the nominator and denominator of eq. (2.50) (pressure wave, left) and eq. (2.51) (shear wave, right) for the three IGC-type MRE phantoms at different amplifier output levels. The absolute values of the elastic moduli $|M|$ and $|\mu|$ can be calculated from linear fits to the data.

4.3.4 Discussion

MRE air pressure experiment

When interpreting the air pressure dependence of volumetric strain, it is important to keep in mind that eq. (2.53) relates oscillating strain to oscillating pressure. Static pressure or deformation is invisible to MRE since it does not cause oscillating strain. Therefore, conclusions about static pressure can only be drawn indirectly from its effect on oscillating strain amplitudes. If the mechanical excitation amplitude is kept constant, two mechanisms can influence strain amplitudes: firstly, the static pressure can alter the properties of the medium in such a way that its compression modulus changes; secondly, higher static pressure can increase friction between the phantom and the container wall, which in turn reduces slip and improves the efficiency with which waves can be transferred into the phantom.

According to eq. (4.2) the compressibility (inverse compression modulus) of a biphasic medium corresponds to the weighted sum of the compressibilities of the two constituents. On the other hand, the compressibility of the gas phase is equal to the inverse gas pressure. The external air pressure acts on the phantom and compresses

the gas, thereby increasing its internal pressure. This in turn causes the compressibility of the gas to decrease. Concurrently, due to compression of the gas, the gas volume fraction β is also reduced. As a result, the weights in the sum in eq. (4.2) change in favor of the matrix compressibility, which is much smaller than the gas compressibility. In total, both effects lead to a reduction of the bulk compressibility and hence an increase of the compression modulus. This contradicts the observation of larger volumetric strain at elevated pressure levels.

However, improved vibration transfer into the phantom can explain the rise of wave amplitudes. Friction between the phantom and the container walls is proportional to the normal contact force between them, which in turn is determined by the static pressure, as illustrated in fig. 4.8. The hysteresis observed in fig. 4.3 suggests that once established, the contact forces decrease at a lower rate than the air pressure, possibly due to adhesive interaction between the two surfaces.

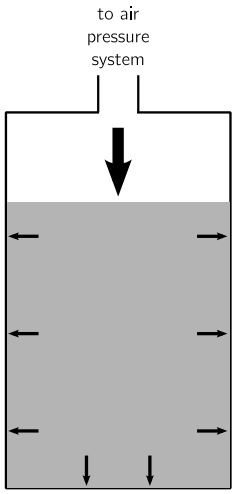

Figure 4.8: Cross-sectional schematic diagram of the air pressure within the IGC-type phantom. External air pressure (large black arrow) acts on the phantom (gray). As a consequence, the normal contact force between the phantom and the vessel walls, indicated by the small black arrows, increases.

This experiment highlights the importance of boundary conditions for compression-sensitive MRE. In the case of in vivo applications, the mechanical excitation is not transferred to the organ of interest directly through coupling to a rigid surface, but the pressure wave has to traverse several layers of soft tissue (fat, muscle, connective tissue). Consequently, boundary conditions become extremely complicated and cannot be measured directly. As a result, volumetric strain values in different phan-

toms can only be compared if attention is paid to keeping boundary conditions as constant as possible. In humans, this condition cannot be fulfilled, and strain comparisons are only feasible between repeated measurements in the same subject and not between individuals.

Rheometer experiments

The match between the rheometer-derived compression moduli of the 23 phantoms and the fit of eq. (4.3), as shown in fig. 4.4, is remarkable. However, the values obtained from the fit for the matrix compression modulus K_{M} (6.5 ± 0.2 MPa) and the intra-cavity gas pressure P (26 ± 2 kPa) are both much lower than anticipated. Since the phantoms were created under normal atmospheric conditions, gas pressure was expected to be comparable to the exterior air pressure of approximately 101.3 kPa. Due to the high solubility of carbon dioxide in water it is possible that the CO_2 in the bubbles was partially dissolved in the water at the boundaries between cavities and the matrix, thus leading to a pressure decrease. The compression modulus of water is in the order of 2.2 GPa and a similar value was expected for the solid matrix. However, since displacements were much larger in the rheometer experiment (several millimeters) than in the MRE (hundreds of micrometers), the compression could have had irreversible effects on the matrix, for example, by crushing thin walls between cavities in regions with high gas concentrations. Both these effects could have contributed to the underestimation of phantom compression moduli, which in turn could have affected the parameters extracted from the fit.

MRE porosity experiment

The increase in volumetric strain with porosity at any fixed amplifier output level is in good agreement with theoretical predictions. For the shear strain no such clear trend is observed. This suggests that volumetric strain is a more sensitive marker of structural changes that accompany variation of porosity in a biphasic medium.

While the reconstructed shear moduli of the phantoms are in the same order of magnitude as previously published data on similar solid gel phantoms [66], the values obtained for $|M|$ are much smaller than expected. Since pressure waves have a significantly larger wavelength than shear waves, their curvature (the magnitude of their second spatial derivative) is closer to zero. Noise in the displacement field data, however, is the same for shear and pressure waves. As a result, the signal-to-noise ratio in the second spatial derivative for volumetric strain is worse than for shear strain.

Since the derivative operator acts as a high-pass filter, the presence of noise increases the magnitude of the spatial derivatives. Hence, when the magnitude of the nominator and denominator of eqs. (2.50) and (2.51) are averaged for the reconstruction of $|\mu|$ and $|M|$, the third-order spatial derivative $\nabla^2(\nabla \bullet \mathbf{u})$ in the denominator causes a reduction of $|M|$. This effect is weaker for $|\mu|$, since $\nabla \times \mathbf{u}$ has larger curvature and thus a better signal-to-noise ratio than $\nabla \bullet \mathbf{u}$. This can also explain why the values of $|M|$ were two orders of magnitude smaller than the predicted values of K, even though $M = K + \frac{4}{3}\mu$ should always be larger. Measurement noise is therefore the limiting factor for numerical modulus reconstruction. However, the volumetric strain of induced oscillation fields appears to be a promising indicator of the underlying mechanical properties. Although the shear modulus has been proven to be a highly relevant parameter in the diagnosis of disease, it did not prove to be sensitive towards structural changes in the case of variation of porosity. Volumetric strain-sensitive MRE is therefore considered an extension to "classical" shear-wave based MRE, providing additional information to the shear elastic properties of tissue.

4.4 Isolated gas-filled cavities model: Lung

The content of this chapter was published in [36].

4.4.1 Background

During respiration, the lung undergoes cyclic deformation including shear, compression and expansion. Inspiration is actively performed through contraction of the thoracic diaphragm and the intercostal muscles, whereas expiration is mainly a passive process driven by gravitation and elastic recoil forces emanating from the deformation of the thorax and the lungs [81]. A loss of pulmonary elasticity can therefore compromise respiratory function. *Chronic obstructive pulmonary disease* (*COPD*) is a common condition that is characterized by a breakdown of lung tissue (*emphysema*) and inflammation originating from the smallest airways (bronchioles) [13]. Repair mechanisms counteracting these effects lead to a thickening of the walls of the pulmonary airways, thus reducing airway diameters and increasing air flow resistance. The combined effect of a reduction of elasticity due to a loss of structural integrity and the higher flow resistance limits the maximum exhalable volume and oxygen uptake per breath. Typically, the symptoms associated with COPD worsen over time and can ultimately lead to disability or death. Even though there is no effective treatment

for COPD, early diagnosis might help to slow down the progress of the disease, for example by adapting the life style (reduction of exposure to tobacco smoke or other irritants) or suitable therapies.

The human lung is one of the most challenging organs in terms of MR imaging. Its low bulk density generates a much smaller signal amplitude than other types of tissue. The microscopic structure of the lung, which is characterized by a large surface area (~80 m^2, [25]) between air filled and interconnected *alveoli* and the surrounding lung parenchyma gives rise to magnetic field discontinuities at the air-tissue boundaries. Fast imaging sequences are required to mitigate the effect of short transverse signal decay times and to reduce image distortions introduced by those $\mathbf{B}_0$ inhomogeneities.

To investigate whether previous findings from phantom experiments could also be confirmed in real organs, the first application of compression-sensitive MRI was performed on the lungs of healthy volunteers. The objective of this study was to investigate whether a change of lung elasticity between two distinct respiratory states is reflected in the amplitudes of oscillating volumetric strain induced by external mechanical vibrations. An earlier study by Mariappan et al. [57] found higher shear stiffness at *total lung capacity* (TLC, maximum voluntary inhalation) compared to *residual volume* (RV, maximum voluntary exhalation).

4.4.2 Materials and methods

Nine healthy male volunteers (mean age: 32.1 ± 6.7 years, range 25–41 years) were investigated in two distinct respiratory states. The volunteers were in supine position, with a wooden transducer plate positioned slightly inferior to their sternum, and 50 Hz vibrations were transmitted from a loudspeaker to the plate through a wooden bar, as previously used in cardiac MRE [18]. Due to the short T_2^* decay constant of lung tissue, emphasis was placed on short echo times, such that only 7 ms were used for motion encoding. A single cycle of a waveform with 0^{th} gradient moment nulling, corresponding to a frequency of 143 Hz, and an amplitude of 20 mT/m was used. Seven adjacent slices with a thickness of 10 mm and 3.1×3.1 mm^2 in-plane resolution were acquired. Six wave phases, equidistantly distributed over one vibration period, were recorded. Signal averaging over 12 identical measurements had to be performed to achieve sufficiently high image quality. With these imaging parameters, a single slice image could be measured in 140 ms (including a delay of 100 ms

to allow for wave propagation into the lung), with an echo time of 23 ms. The volunteers were instructed to find two reproducible respiratory states as close as possible to maximum inspiration and maximum expiration, respectively. Those two states are comparable to *total lung capacity* and *resdiual volume*, which have been studied by Mariappan et al. with shear-wave based MRE [57]. Measurements of each of these states were distributed over nine breath-hold periods of 24 seconds each, separated by short periods of free breathing.

Data processing

Wrapped phase images $\phi(\mathbf{r})$ were converted into complex data as $\exp\big(\mathrm{i}\phi(\mathbf{r})\big)$. Noise suppression was performed through convolution with a $7\times7\times7$ boxcar kernel. First-order spatial derivatives were calculated according to eq. (4.4). After temporal Fourier transform of the derivatives, the axial components oscillating at the fundamental frequency (50 Hz) were added to yield the displacement field divergence. Its magnitude, $|\nabla\bullet\mathbf{u}|$, was averaged over the right lobe of the lung. The left lobe of the lung was excluded from the study due to its proximity to the heart, which can induce motion artifacts.

4.4.3 Results

Propagating waves at the excited mechanical frequency were detected in all nine volunteers. Waves images from one volunteer are shown in fig. 4.9. Wavelengths are visibly shorter in expiration than in inspiration.

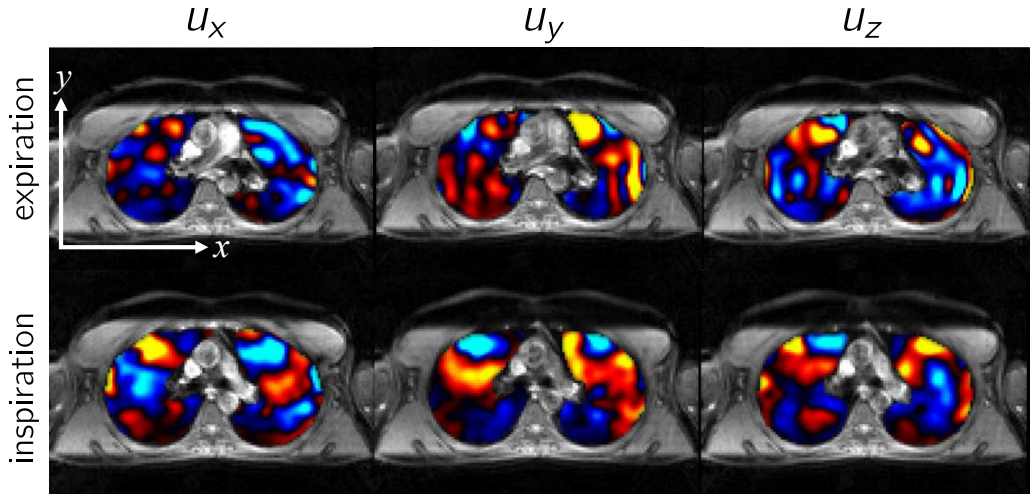

Figure 4.9: Deflection field in a central slice through the lung of one volunteer.

The magnitude of the divergence is shown for one volunteer in fig. 4.10. The mag-

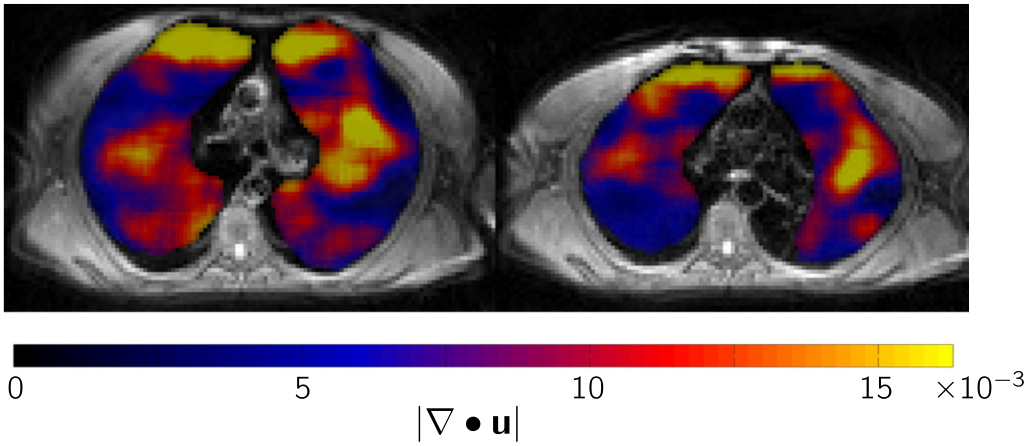

Figure 4.10: Volumetric strain magnitude $|\nabla \bullet \mathbf{u}|$ in the lung of one volunteer. Inspiration is shown on the left, expiration on the right. Averaging was performed only over the right lobe of the lung (shown as the left lobe in the image, due to radiological viewing conventions, looking at a person from the feet toward the head), since the left lobe is more susceptible to heart-induced motion artifacts.

nitude of the divergence and the three axial derivatives $\frac{\partial u_i}{\partial r_i}$ were averaged in each subject over the right lung lobe and the central five slices. To compare inspiration and expiration, per-subject averages of those four quantities ($|\nabla \bullet \mathbf{u}|$, $\frac{\partial u_i}{\partial r_i}$) were calculated in both states. The ratio "inhalation/exhalation" is shown for each of those in fig. 4.11. These ratios were first averaged over each of the five central slices. The error bars in fig. 4.11 correspond to the standard deviation of those five slice averages. The horizontal line at ordinate value 1 represents the case that no difference between inspiration and expiration was measurable. Single-variable Student's t-test was employed to assess whether the data points were significantly distinct from 1. In all but one case ($\frac{\partial u_z}{\partial z}$ for volunteer #5), the test was positive at the 5 % level. For 11 out of the 36 data points, significance at the 0.1 % level was observed.

The five slice averages of $|\nabla \bullet \mathbf{u}|$ for each volunteer are presented in fig. 4.12. The boxes extend from the 25$^{\text{th}}$ to the 75$^{\text{th}}$ percentile, whereas the whiskers indicate the total data range. Wilcoxon rank-sum tests were performed to analyze if the two physiological states were statistically significant on a per-subject basis. Results were positive in seven out of nine cases at the 5 % level; these are marked with stars in fig. 4.12.

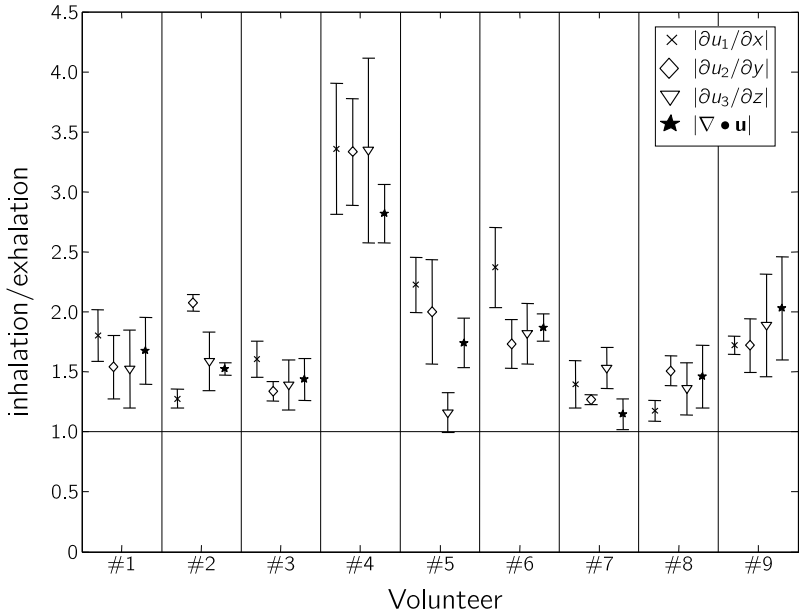

Figure 4.11: Ratios "inhalation/exhalation" of the averaged magnitude of the axial derivatives and the divergence in the lungs of all nine volunteers.

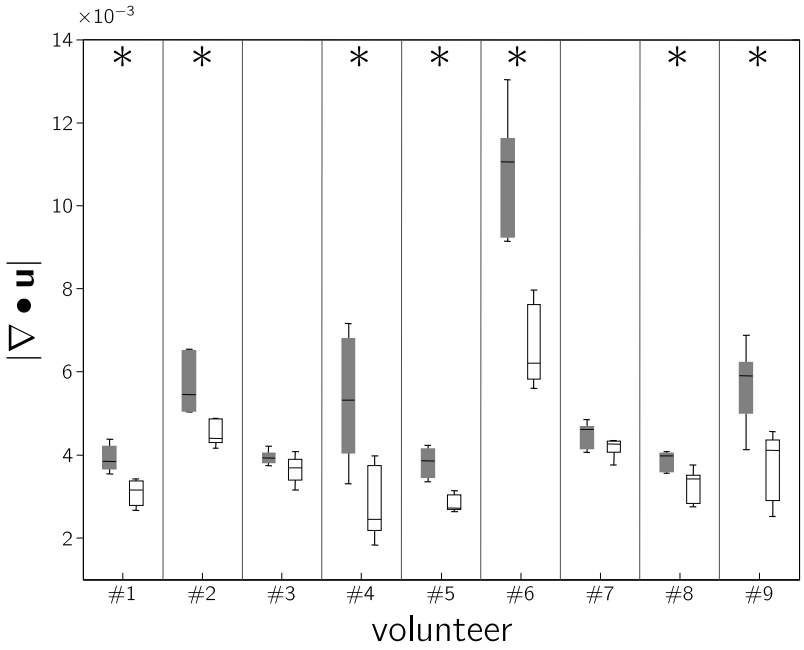

Figure 4.12: Averaged values of $|\nabla \bullet \mathbf{u}|$ in the lung of each volunteer during inspiration (gray) and expiration (white). Stars indicate statistically significant different mean values at the 5 % level.

4.4.4 Discussion

Results from the lung study indicate that externally stimulated volumetric strain changes with respiratory state. Strain amplitudes were higher during inspiration, which, according to eq. (2.54), corresponds to a reduction of the compression modulus K. This contrasts the findings presented in [57], in which a higher shear modulus was detected in inspiration. While any conversion between the shear modulus μ and the compression modulus K requires knowledge of another independent parameter (e.g. the Lamé parameter λ), it appears reasonable to assume that a state of elevated μ is associated with an increase in K, and vice versa. Inversion of the wave equation was considered infeasible due to the high noise level, which is further exacerbated if third-order spatial derivatives of $\mathbf{u}$ are required.

Actual strain amplitudes vary strongly between volunteers, as illustrated in fig. 4.12. In MR Elastography based on the inversion of a wave equation, the actual wave amplitude cancels out, since all terms in the unattenuated wave equation are linear in the oscillation amplitude $|\mathbf{u}|$. However, this is not the case if volumetric strain, $|\nabla \bullet \mathbf{u}|$, is used as an absolute quantity. Factors such as the amplifier output level and the physique of the volunteer can vary, thus preventing direct comparison of numerical values across subjects. Since inspiration and expiration in each volunteer were probed in subsequent measurements with identical parameters, averaged strain values between those two states are considered comparable in every subject individually, and their ratios, as presented in fig. 4.11, are then independent of the actual wave amplitudes.

While the data in fig. 4.11 indicate that volumetric strain is systematically higher during inspiration, the large variability of the ratios prompted further investigation. It was found that the volunteers had adapted different ways of implementing the inspiration state. Some reported that they had held their breath but kept the glottis open, so that intra-pulmonary pressure was equal to atmospheric pressure, while others had performed a *Valsalva maneuver*, during which exhalation is attempted against a closed glottis, leading to an intrathoracic pressure build-up. This was only discovered several weeks after the examinations had been performed, and not all volunteers were able to recall confidently how they had attained the inspiration state, so that they could not be separated into subgroups retrospectively.

Volunteer #4 was the only smoker in the cohort. While his inspiration/expiration ratio is much higher than for all other subjects, the absolute strain levels, as shown in

fig. 4.12, are in the normal range.

For future studies, several modifications to the experimental routine are suggested to minimize systematic bias. Firstly, volunteers or patients should be trained prior to the measurement to ensure that the physiological states are more comparable between volunteers. This could be further aided by using feedback hardware, as suggested in [56]. Furthermore, plethysmographic methods could be employed to obtain quantitative values characterizing the different respiration states, which in turn could be correlated with changes in volumetric strain. Alternatively, MR-based volumetry could be used as a regressor. Nevertheless, the reported study is the first in vivo application of compression-sensitive MRE and corroborates previous findings obtained using phantoms.

4.5 Vascular soft tissue model: Liver

The experiments and results presented in this chapter were published in [35].

4.5.1 Background

The experiments discussed so far were performed on organs or phantoms with isolated gas-filled cavities, which is a valid model system for the lung, but not readily applicable to other organs or biological tissue in general. Soft biological tissue is saturated with interstitial fluid and blood and does not generally contain gas cavities. To assess the potential of externally stimulated volumetric strain in a solid organ comprising vasculature and soft tissue, an experiment was performed on an excised ovine liver. The vasculature formed an interconnected pore space, while the parenchyma acted as the matrix of the poroelastic model.

The liver fulfills a variety of vital tasks, including the synthesis of hormones, bile and plasma proteins, the detoxification of blood, and the destruction of red blood cells at the end of their life cycle. While manual palpation of the liver is possible, shear-waved based MRE has become a reliable clinical tool for the diagnosis and staging of liver fibrosis [55]. The liver is supplied with blood by two independent systems, the hepatic arteries and the portal vein, whereas the hepatic vein receives the outflowing blood. The blood in the portal vein is drained from the spleen and the gastrointestinal tract. If flow resistance in the hepatic blood vessels increases, for example as a consequence of fibrosis, the hepatic portal blood pressure may rise. Elevated portal pressure is

considered a predictor for liver cirrhosis [78] and, if left untreated, can cause severe complications or death, due to rupture of the gastrointestinal varices (dilated small veins) [23].

To date there exists no non-invasive method for the measurement of the hepatic portal blood pressure. Since pore pressure is a central quantity in Biot's poroelastic theory, this study intended to verify that a change in hepatic portal pressure leads to a change in the amplitude of induced volumetric strain in the liver. Non-invasive assessment of hepatic portal pressure could aid in the early detection of disease and facilitate treatment of the condition before the onset of clinical symptoms.

4.5.2 Materials and methods

A freshly excised sheep liver was obtained from a butcher and investigated within 28 hours after death. The hepatic artery and the hepatic vein were sealed with agarose-based WiroGel M (BEGO, Bremen, Germany) and a flexible hose connected to a water reservoir was attached to the portal vein. Variations in the hepatic portal pressure could be emulated by adjusting the height at which the reservoir was mounted.

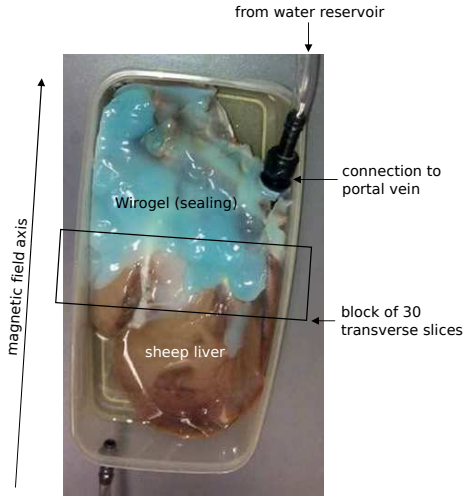

Figure 4.13: Setup for the ovine liver MRE experiment. The blue substance is WiroGel M used to seal the hepatic arteries and veins. The hose from the water reservoir is visible in the top right corner. The setup as shown was placed in the head cradle inside the MR scanner.

After preparation of the liver, the setup shown in fig. 4.13 was placed inside the head cradle which is normally used for cerebral MRE measurements in humans. The cradle was positioned inside the 4-channel head coil of a 1.5 T scanner (Siemens Sonata).

Imaging was performed with the following parameters: 30 transverse slices; three orthogonal projections of the displacement field; spatial resolution $2 \times 2 \times 2$ mm^3; matrix size: 96×88; field of view: 192×176 mm^2; echo time: 99 ms; repetition time: 240 ms; vibration frequencies: 25 and 50 Hz; eight wave phases. The height of the water column applied to the portal vein was set to 0 cm, 20 cm, 40 cm, 60 cm and 77 cm in successive measurements, corresponding to hydrostatic pressures between 0 and 7.6 kPa. The sealing of blood vessels with WiroGel did not render them perfectly watertight, and a constant flow of water through the liver was observed.

Volumetric strain $|\nabla \bullet \mathbf{u}|$ and shear strain $|\nabla \times \mathbf{u}|$ amplitudes were calculated from the acquired complex displacement fields using the Anderssen-Hegland averaging gradient scheme (see eqs. (4.4) and (4.5)). Following temporal Fourier transform, oscillating strain amplitudes at the vibration frequency were averaged over a manually selected region of interest devoid of large blood vessels. Strain amplitudes were averaged over the two vibration frequencies to mitigate geometric effects and boundary conditions. The same analysis was also performed at the second harmonic of the vibration frequency (which had not been mechanically excited, thus no oscillation was to be expected) to assess whether the constant flow of water through the liver interfered with strain amplitude calculations.

4.5.3 Results

Averaged volumetric strain amplitudes decreased monotonously as the hydrostatic pressure increased, from $2.87 \cdot 10^{-4}$ at 0 kPa to $1.40 \cdot 10^{-4}$ at 7.6 kPa, as illustrated in fig. 4.14. Over the same pressure range, shear strain amplitudes were consistently larger than those of volumetric strain, but did not show a dependence on hydrostatic pressure. Volumetric strain in the second harmonic of the vibration frequency was considerably smaller than in the first harmonic and displayed a less pronounced dependence on hydrostatic pressure.

4.5.4 Discussion

In contrast to shear strain, volumetric strain amplitudes appear to be sensitive to intra-vascular pressure changes. A decrease in strain amplitudes with increasing pressure is associated with an increase in stiffness, according to the proportionality $|\Delta\tilde{P}| = K|\nabla \bullet \mathbf{u}|$ (see eq. (2.54)). Here, it is important to note that $\Delta\tilde{P}$ is the amplitude of the *oscillating* pressure induced by the external vibration, which is not directly

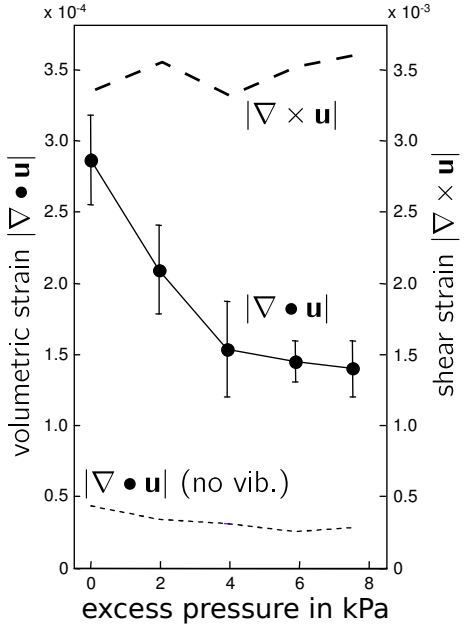

Figure 4.14: Spatially averaged strain amplitudes from the ovine liver experiment. The lowest curve (labeled "no vib.") corresponds to strain values extracted from the FFT spectrum at the second harmonic of the vibration frequency to assess whether flow of water through the liver had a measurable influence on the volumetric strain.

correlated with the hydrostatic pressure. $|\Delta\tilde{P}|$ is determined by the vibration amplitude and the efficiency with which vibrations can be transferred into the liver. Both parameters did not change over the course of the experiment. Therefore, $|\Delta\tilde{P}|$ was considered constant throughout all measurements. These results suggest that the compression modulus K is not a material constant, but that it rather depends on the hydrostatic pressure. This effect can be explained by Biot's theory of poroelasticity as follows: In a biphasic material with incompressible constituents, volumetric deformation can only be achieved by displacement of one phase relative to the other. In this work, it is assumed that the matrix is immobile, whereas inter-cellular water can be squeezed out of the system. Hydrostatic pressure acts primarily on the fluid component, hindering its mobility and thus increasing its resistance against displacement. Macroscopically, this is reflected in reduced displacement field amplitudes. However, it has to be noted that an ex vivo organ is deprived of all potential self-regulation and feedback mechanisms that might exist in living organs, such as dilation or constriction of blood vessels. A direct translation from ex vivo results to in vivo is therefore not always possible, and additional validation has to be

performed in living organs.

Once the ovine liver study had demonstrated the feasibility of compression-sensitive MRE in detecting different pressure levels, Jing Guo, Rolf Reiter and Thomas Kröncke performed a study on thirteen patients with clinical symptoms of hepatic hypertension [35]. The standard treatment of hepatic hypertension is termed *TIPS* (transjugular intrahepatic portosystemic shunt) and comprises the surgical creation of an artificial channel connecting the inflow portal vein to the outflow hepatic vein, thus permitting a fraction of the blood from the hepatic vein to bypass the liver and alleviating pathological hypertension in the liver. The patients were examined before and after the intervention with a protocol similar to the one used for the ovine liver. A catheter-mounted pressure sensor was inserted into the portal vein to measure the portal pressure during surgery. The study found an increase in volumetric strain after the intervention in twelve patients whose hepatic venous pressure gradient (HVPG, the pressure gradient over the liver between inflow and outflow vessels) had been in the pathological range ($>$ 10 mmHg), as shown in fig. 4.15a. One patient with a pressure gradient close to the healthy range (6 mmHg; healthy range: $\leq$ 5 mmHg) displayed a decrease in volumetric strain after surgery.

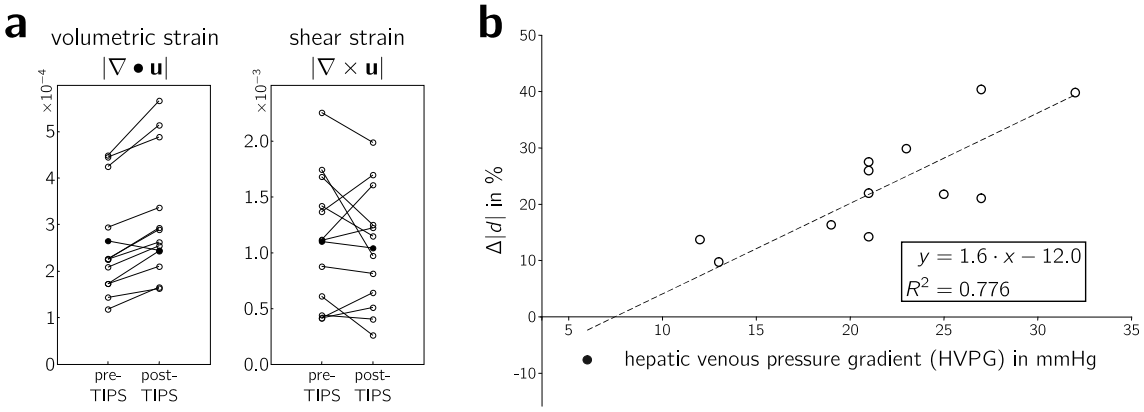

Figure 4.15: Results from the TIPS study by Guo, Reiter and Kröncke published in [35]. **a**: Spatial averages of shear strain and volumetric strain in the liver before and after TIPS. Each pair of circles connected by a line corresponds to one patient. Hollow circles represent patients with actual portal hypertension (HVPG $>$ 10 mmHg), whereas the solid circles designate one patient with unpathological HVPG. **b**: Correlation between the relative change of volumetric strain $\Delta|d|$ and the intra-surgically measured HVPG. The dashed line is a linear fit to the data with the parameters listed in the box.

These results are consistent with the findings in the ovine liver. As TIPS relieves the pressure build-up, post-intervention pressure gradients are expected to be smaller. On average, volumetric strain increased by (21 ± 13) % after TIPS in the twelve patients with pathological pressure gradients. No such trend was observed for shear strain with an average increase of (−2 ± 32) %. Furthermore, a linear relation between the HVPG before TIPS and the relative change of volumetric strain, $\Delta|d| = \frac{|\nabla\bullet\mathbf{u}|^{\text{after}} - |\nabla\bullet\mathbf{u}|^{\text{before}}}{|\nabla\bullet\mathbf{u}|^{\text{before}}} \cdot 100\,\%$, was found with a slope of 1.6 %/mmHg, a correlation coefficient $R^2 = 0.776$ and $p = 6.95 \cdot 19^{-5}$ (fig. 4.15b). A second weaker correlation was found between pre-TIPS portal venous pressure and $\Delta|d|$ (slope: 0.99 %/mmHg, $R^2 = 0.50$, $p = 0.0016$). No correlation could be established between strain quantities and any of the post-TIPS pressure measurements. However, post-TIPS hepatic pressure was quantified immediately after TIPS placement, whereas MRE was performed three days after the intervention. It is not known whether the post-TIPS pressure values remained constant, or if they were subject to slow change due to homeostatic processes or structural adaptations in liver parenchyma.

In conclusion, compression-sensitive MRE was found to be sensitive to changes in the hepatic portal pressure both in an ex vivo model and in human patients. Further research will be necessary to develop the technique into a clinically applicable diagnostic instrument and to enable absolute pressure quantification.

4.6 Vascular soft tissue model: Brain

The content of this chapter was published in [36].

4.6.1 Background

Being the largest energy consumer in the human body, the brain receives on average 14 % of the cardiac output [97]. The brain is suspended in cerebro-spinal fluid (CSF), which provides buoyancy, protects the brain from injury due to striking the cranium, and contributes to supplying nutrients and draining metabolic waste [77]. The *Kellie-Monro hypothesis* states the total intra-cranial volume, comprising brain parenchyma, CSF and blood, is constant [61]. As a consequence, there has to be an interaction between cerebral blood and CSF volumes and various pressure-related parameters, such as the hydrostatic parenchyma pressure, arterial pulsation pressure, venous pressure, and CSF pressure [22, 29, 99]. Any distortion or imbalance in

the regulation of these parameters puts the brain at risk of receiving damage or developing disorders, such as normal pressure hydrocephalus[1] (NPH) [28, 94].

Numerous studies have utilized MRI to investigate patterns of cerebral fluid flow and the displacement of brain parenchyma driven by cardiac pulsation [19, 29, 48, 74, 90, 91, 98]. According to these works, the brain responds to the arrival of the cardiac pulse wave by a cranio-caudal[2] motion, accompanied by a simultaneous medio-lateral[3] shift [29], as sketched in fig. 4.16. However, little information is available regarding the volumetric strain within brain parenchyma related to these pulsation effects. Therefore, recording brain tissue motion patterns and applying the divergence operator to the resulting displacement fields can help to achieve new insights into this matter.

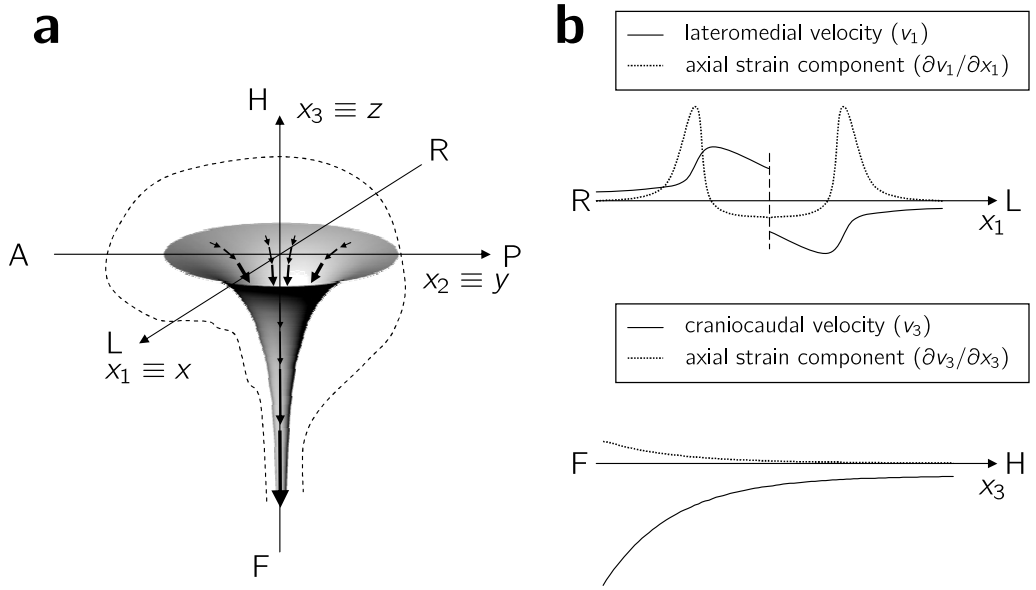

Figure 4.16: **a**: Schematic depiction of brain motion during the arrival of the systolic pressure wave. Directions are designated as A: anterior (front), P: posterior (back), L/R: left/right, H/F: head/feet. The principal motion-component is towards the feet, causing a funnel-shaped flow pattern. The figure is based on data published in [29], which are in agreement with data presented in this work. **b**: Motion velocity (solid line) and its spatial derivative (dashed line) for the right→left (top) and feet→head (bottom) components. Note that the curves are schematic representations of line profiles analyzed in the measured data.

Previous work that applied poroelastic theory to brain parenchyma was focused on

[1] Despite its name, normal pressure hydrocephalus is characterized by elevated intracranial pressure.
[2] Along the head-feet axis.
[3] From the ears toward the center of the brain

hydrocephalus [38, 51, 69, 93]. In this study, the properties of the slow compression wave predicted by the Biot model [8] in the low-frequency range (< 70 Hz) were analyzed in healthy volunteers to assess and quantify volumetric strain effects in the brain with and without external mechanical stimulation, following pioneering work on poroelastic data analysis of cerebral MRE by Perriñez et al. [71, 72] and Pattison et al. [68].

A set of three experiments was performed to assess the change of volumetric strain under different physiological conditions in healthy volunteers. In the first experiment, intrinsic pulsation of the cerebral blood vessels, caused by the cardiac cycle, was exploited as the driving force. In the second and third experiment, 25 Hz vibrations were induced, similar to the previously discussed experiments. In the second experiment, compression-sensitive MRE was performed at different time points of the cardiac cycle to quantify the modulation of brain elasticity by the arterial pulse wave (APW). In the third experiment, induced volumetric strain amplitudes were compared between a relaxed state and a state of abdominal muscle contraction (AMC), in which the venous blood flow from the brain to the heart was hindered, such that intracranial pressure increased. These experiments extend research on 3D displacement MRI [90] and 3D cerebral MRE [27, 62, 80].

Encoding of non-harmonic motion

Motion sensitivity can be introduced into any MRI sequence by inserting a balanced gradient waveform between the excitation pulse and the signal readout. This general principle is known as *phase-contrast MRI* (PC-MRI). Its applications include flow quantification [11, 96] and MR angiography [15, 16].

The conversion between the MR signal phase ϕ and the displacement $\mathbf{u}$ according to eq. (2.30) is applicable only if the waveform of the motion field is known. If brain pulsation with no additional external vibration is used as the actuation force, no such linear relationship between motion displacement amplitude and accumulated signal phase can be established. Instead, the more general eq. (2.32) has to be used:

$$\phi(t) = \phi(t_0) + \sum_{k=0}^{\infty} \frac{1}{k!} \left. \frac{\partial^k \mathbf{x}(\vartheta)}{\partial \vartheta^k} \right|_{\vartheta=t_0} \bullet \mathbf{M}_k(t) \tag{4.6}$$

with spin trajectory $\mathbf{x}(t)$ and the k-th gradient moment $\mathbf{M}_k(t)$ (see eq. (2.33) for the definition). The motion-encoding gradient is active only for $t_0 \le t \le t_0 + T$. The value

of $\phi(t)$ is not measured continuously, but only the final value $\phi(t_0+T)$ is sampled once the motion-encoding gradient has ended. Since the MEG is balanced, its zeroth moment $\mathbf{M}_0(t_0+T)$ equals $\mathbf{0}$. Consequently, ϕ is independent of the initial spin position $\mathbf{x}(0)$. As a first-order approximation, the motion can be considered constant over the duration T of the motion-encoding gradient: $\mathbf{x}(t)\approx\mathbf{x}(t_0)+\mathbf{v}\cdot(t-t_0)$. Equation (4.6) then reduces to

$$\phi(t_0+T)=\phi(t_0)+\mathbf{v}\bullet\mathbf{M}_1(t_0+T) \tag{4.7}$$

In the case of rectangular MEG waveforms comprising N cycles with 0^{th} gradient moment nulling (as depicted in fig. 2.7A), amplitude A and duration T, the accumulated phase ϕ_i acquired as a projection of the displacement velocity field $\mathbf{v}$ onto the i-th Cartesian axis is

$$\phi_i=-\frac{\gamma T^2 N A}{4}v_i+\phi_0. \tag{4.8}$$

The additive constant ϕ_0 is a superposition of two effects: phase offsets from an inhomogeneous susceptibility distribution and residual flow encoding of the imaging gradients. The former effect is static and does not depend on the time point during the cardiac cycle at which the image is acquired. The latter effect is stronger if the EPI readout coincides with a cardiac phase with high-velocity flow, and weaker during the diastolic phase. However, since the imaging gradients are much weaker than the motion-encoding gradients, their effect on ϕ_i is much smaller than the desired flow-encoding effect of the MEGs. The sign of the velocity field divergence $\nabla\bullet\mathbf{v}$ indicates local expansion (+) or contraction (−). Brain pulsation is a periodic process with period T_{cc}. Hence, at the end of the cycle, the displacement has to return to its initial state: $\mathbf{u}(0)=\mathbf{u}(T_{\text{cc}})$. Furthermore, since $\mathbf{v}=\frac{\partial\mathbf{u}}{\partial t}$, the time integral of $\nabla\bullet\mathbf{v}$ over one cardiac cycle has to vanish [74]:

$$\int_0^{T_{\text{cc}}}\nabla\bullet\mathbf{v}(t)\,\mathrm{d}t=\nabla\bullet\mathbf{u}(T_{\mathbf{cc}})-\nabla\bullet\mathbf{u}(0)=0. \tag{4.9}$$

This condition also holds true for each axial derivative of $\mathbf{v}$ and will be used as a normalization criterion to partly eliminate the aforementioned phase offsets.

4.6.2 Materials and methods

All three experiments were performed on a 1.5 T clinical MR scanner (Siemens Sonata, Erlangen, Germany) using the EPI sequence described above. In the second and third experiment, mechanical vibrations with a frequency of 25 Hz were stimulated using

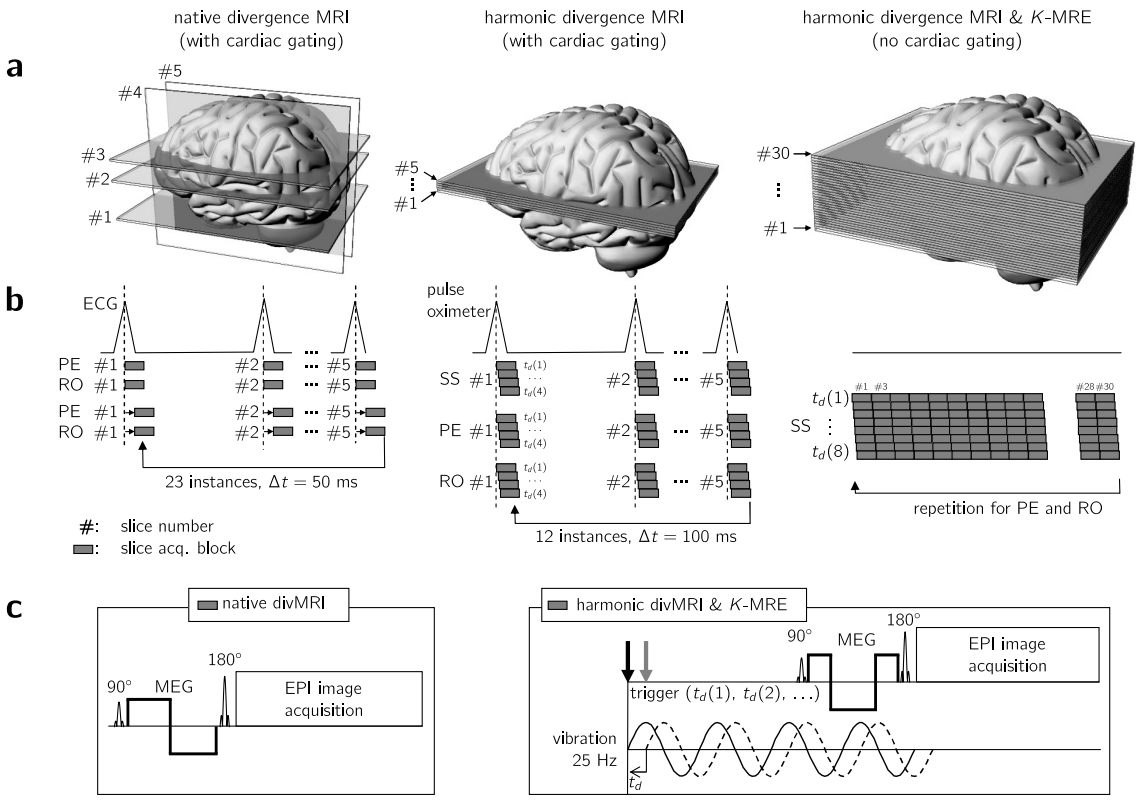

Figure 4.18: Overview over slice positioning (**a**) and sequence timing (**b**, **c**) in the three human brain experiments. Each gray box in **b** represents the acquisition of a single slice. The timing diagram for a single-slice acquisition is shown in row **c**. The diagrams in row **b** should be read left to right, then top to bottom. In the native divergence MRI experiment, motion along the phase-encoding axis is encoded in all five slices. Every slice is measured following the peak in the ECG signal. After those five acquisitions, the same procedure is repeated with motion-encoding along the readout axis. The same procedure is then repeated with a short delay (50 ms) between the ECG peak and the image acquisition to sample a different phase of the cardiac cycle. Altogether, 23 different phases are sampled, in steps of 50 ms. A similar scheme was used for the second experiment, in which all three encoding directions were measured and mechanical vibration was employed. Harmonic excitation requires sampling of several different phases of the wave cycle, indicated by delays (between the trigger pulse and the MEG) $t_d(1)$ through $t_d(4)$. All four wave phases were sampled for one encoding direction before the motion-encoding axis was toggled. The whole procedure was repeated with 12 different delays (in steps of 100 ms) between the ECG peak and image acquisition. In the third experiment, no physiological gating was used, allowing the whole measurement to be performed without any intermediate delays.

the loudspeaker-based setup shown in fig. 4.17. In all three studies, images were

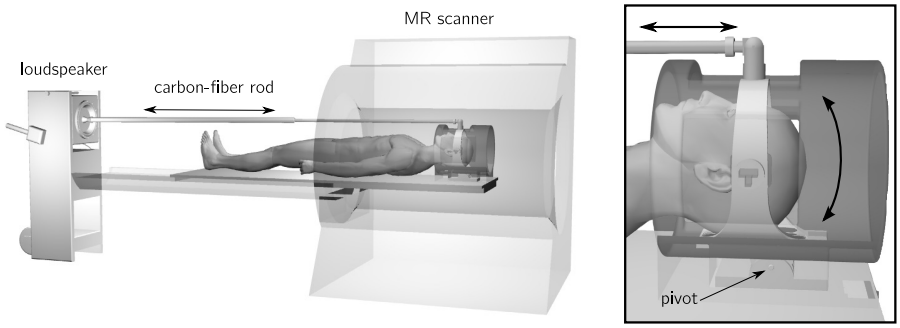

Figure 4.17: Experimental setup for cerebral MRE. Vibration is transferred from the loudspeaker to the head cradle via a telescopic carbon-fiber rod and converted from linear to a "nodding" motion, as indicated by the double-ended arrows. The close-up on the right shows the head cradle (light gray) inside the MR head coil (dark gray).

acquired with an isotropic spatial resolution of $2 \times 2 \times 2$ mm^3 and two signal averages for improved SNR. A diagram of the timing and slice positioning of all experiments is presented in fig. 4.18.

i) Native pulsation

This study was conducted on six healthy male volunteers (mean age 33.7 years, range 25—50 years) with no history of cardiac or neuronal disease. An MR compatible three-channel ECG (electro-cardiogram) was attached to the left chest and connected to the physiological trigger input of the MR scanner. Three transverse (orthogonal to the head–feet direction) and two sagittal (orthogonal to the left–right direction) slices were selected based on a 3D time-of-flight (TOF) angiography scan [58], as illustrated in fig. 4.19. The transverse slices were placed at the pons, the genu of the corpus callosum, and the centrum semiovale, respectively. The sagittal slices were positioned symmetrically through the basal ganglia. The spatial resolution for all slices was $2 \times 2 \times 2$ mm^3.

For each slice, only the two in-plane motion components were encoded in consecutive measurements. During each cardiac cycle, a single image of one slice was recorded. The delay between the QRS complex in the ECG signal (indicating the beginning of systolic cardiac contraction) and the sequence start was increased from 0 ms in steps of 50 ms up to 1.1 seconds, such that slightly more than a full cardiac cycle was covered. A single cycle ($N = 1$) of an MEG waveform with 0^{th} gradient

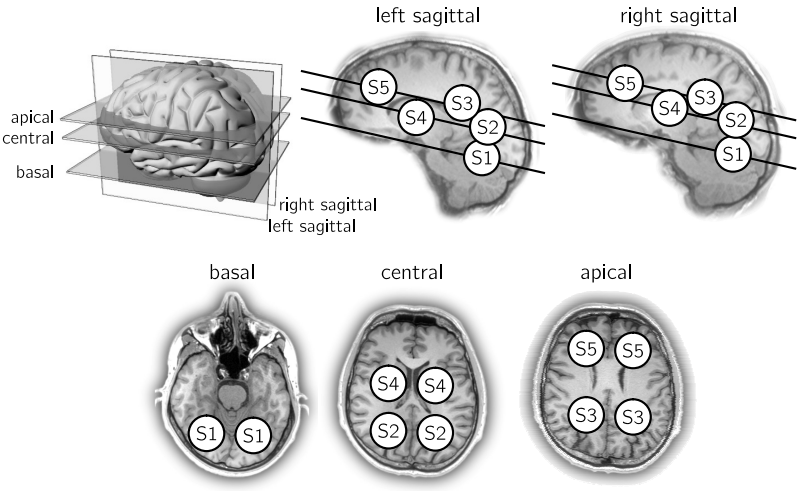

Figure 4.19: Placement of the sagittal and transverse slices in the cerebral pulsation study.

moment nulling (i.e. without flow compensation), an amplitude of $A = 15$ mT/m and a duration of $T = 20$ ms was used for encoding the in-plane motion field. The echo time for a single-shot acquisition of one slice was 116 ms.

No external vibration was used in this experiment, differentiating the technique from MR-Elastography. Instead of the displacement field $\mathbf{u}$, the *displacement velocity field* $\mathbf{v} = \frac{\partial}{\partial t}\mathbf{u}$ was calculated from images acquired using phase-contrast MRI.

The MR-derived signal phase, $\exp(\mathrm{i}\phi_j)$, was filtered with a 9×9 Gaussian kernel with a standard deviation of 1.5 pixels. Spatial derivatives of the phase were calculated via eq. (4.4) and converted to velocities according to eq. (4.8). The phase offset ϕ_0 in eq. (4.8) introduces a velocity offset v_0, which would adversely affect the following data analysis. In order to eliminate this offset, the duration of the cardiac cycle, T_{cc} for every subject was determined visually by screening the temporal variation of $v_i(t)$ for periodicity (which was feasible since more than one cardiac cycle had been sampled). The condition imposed by eq. (4.9) was then enforced by subtracting the mean of each axial derivative over one cardiac cycle:

$$\frac{\partial v_i}{\partial r_i}(t) \quad \longrightarrow \quad \frac{\partial v_i}{\partial r_i}(t) - \frac{1}{T_{\mathrm{cc}}} \int_0^{T_{\mathrm{cc}}} \frac{\partial v_i}{\partial r_i}(t)\,\mathrm{d}t\,. \tag{4.10}$$

Ten small circular regions of interest (ROIs) were selected in the two sagittal slices (five per slice) and the three transverse slices (two in the inferior slice, four in each of the

two superior slices) along the intersection of sagittal and transverse slices as shown in fig. 4.19. Axial spatial derivatives of the displacement velocity field **v** were averaged within those regions of interest, and finally the averaged velocity field divergence was calculated according to

$$\nabla \bullet \mathbf{v} = \frac{\partial v_1}{\partial r_1}^{(\text{trans})} + \frac{1}{2}\left(\frac{\partial v_2}{\partial r_2}^{(\text{trans})} + \frac{\partial v_2}{\partial r_2}^{(\text{sag})} \right) + \frac{\partial v_3}{\partial r_3}^{(\text{sag})}, \tag{4.11}$$

where (trans) and (sag) indicate whether the quantity was derived from a transverse or sagittal slice. The resulting averages of the individual derivatives and the divergence were plotted versus the delay between the QRS complex and the sequence start. The ROIs in the left hemisphere were found to have a very similar temporal variation as their counterparts in the right hemisphere (e.g. S1 in the left and right hemisphere). Data was therefore averaged in every volunteer over pairs of symmetrically placed ROIs, such that five data series, corresponding to the regions S1–S5, were obtained for each subject. Since the cardiac interval and the time of travel of the pulse wave from the heart to the brain can vary between individuals, these resultant curves were normalized to a standardized time axis (in units of percent of the cardiac period) to facilitate inter-subject comparisons. The origin of the new time axis represents the arrival of the arterial pulse wave (APW) in the brain, which was obtained as the peak position of $\nabla \bullet \mathbf{v}$ in each ROI. The period of the cardiac cycle corresponds to the peak-to-peak interval. This was possible because the sampling interval was 1.1 seconds, longer than the duration of a cardiac cycle in all subjects. The arrival time and period were then used to re-sample the data by linear interpolation, such that one cycle was covered by 20 equidistant points.

ii) Cardiac-gated MRE

The experiment was performed on a group of eight healthy male volunteers, with a mean age of 32.4 years, spanning a total range of 25–51 years. A block of 5 contiguous slices, without gap, was positioned through the corpus callosum and aligned with the genu-splenium axis, as shown in fig. 4.18. The spatial resolution was $2 \times 2 \times 2$ mm^3. Cardiac gating was achieved by placing a pulse oximeter on the left index finger of the volunteer. Measurement were performed at twelve points of the cardiac cycle with a temporal separation of 100 ms. For each of these instances, a total of 60 image slices (five slices, three displacement field components, four wave propagation phases) were acquired. The echo time and repetition time were 116 ms and 225 ms,

respectively. An MEG waveform with first-order gradient moment nulling (the green waveform in fig. 2.7A) with a duration of 50 ms and an amplitude of 25 mT/m was deployed.

Post-processing of the data consisted of spatial low-pass filtering, using the same parameters as for experiment (i), and calculating spatial derivatives $\frac{\partial \phi_j}{\partial r_j}$ using the gradient unwrapping method (eq. (4.4)). Temporal Fourier transform was performed along the wave phases to separate the 25 Hz oscillation from other motion effects encoded by the MEG. The values were scaled from radians to actual displacements using eq. (2.30). Volumetric strain $\nabla \bullet \mathbf{u}$ was calculated as the sum of the axial derivatives, and its magnitude was averaged over the entire parenchyma within the central three slices of the block. Ventricles and CSF-filled spaces were excluded. As in experiment (i), the time course of $|\nabla \bullet \mathbf{u}|$ was re-mapped to a normalized time axis, the origin of which coinciding with the arrival of the arterial pulse wave in the brain.

iii) MRE and abdominal muscle contraction

The experiment was performed with the same parameters as experiment (ii), but without physiological gating. Eight healthy male volunteers with a mean age of 35.8 years, between 25 and 51 years, participated. Each volunteer was subjected to two measurements, first in a relaxed state as the baseline, and then with maximum contraction of the abdominal muscles (abdominal muscle contraction, AMC). The latter had the effect of increasing cerebral venous blood pressure by hindering venous return of blood from the brain.

A block consisting of 30 contiguous slices through the central brain was aligned with the genu-splenium axis, as indicated in fig. 4.18. As in experiments (i) and (ii), the spatial resolution was $2 \times 2 \times 2$ mm^3.

The MEG waveform was comprised of one cycle with first-order gradient moment nulling (green line in fig. 2.7A), with a duration of 40 ms and an amplitude of 25 mT/m. The echo time and repetition time were 116 ms and 272 ms, respectively. For each slice, eight wave propagation phases and three orthogonal projections of the displacement field were acquired.

Since post-processing for this experiment necessitated the actual displacement field, rather than only its spatial derivatives, gradient unwrapping, as performed in (i) and (ii), was not eligible. Instead, Flynn's two-dimensional phase unwrapping algorithm

[24] was deployed, and unwrapped phases were converted to displacements according to eq. (2.30). The displacement fields were then smoothed using a Gaussian kernel as described in (i), and temporal Fourier transform along the wave propagation steps was performed to extract the oscillatory component. In addition to the analysis of volumetric strain, spatial maps of the shear modulus μ and the compression modulus K were obtained from direct inversion of the wave equation (eq. (2.63)). In a final step, the real and imaginary parts of the parameter maps and the volumetric strain amplitude $|\nabla \bullet \mathbf{u}|$ were averaged over the entire brain parenchyma contained in the imaging slices, excluding CSF.

4.6.3 Results

i) Native pulsation

In all volunteers, dilatation was detected between 50 and 100 ms after systole, marking the arrival of the pulse wave in the brain. The time-resolved values of $\nabla \bullet \mathbf{v}$, averaged over all six subjects, are shown in fig. 4.20a. Positive and negative values represent expansion and compression, respectively.

The values of $\nabla \bullet \mathbf{v}$ at 0 % and 50 % of the cardiac cycle, e.g. systole (cardiac contraction) and diastole (relaxation), are compared in fig. 4.20b. Each column comprises six data points, one from each subject representing $\nabla \bullet \mathbf{v}$ at those two time points, averaged over one pair of symmetric ROIs. The boxes extend from the 25^{th} to the 75^{th} percentile, whiskers indicate the total range, and crosses mark outliers. For each of the ROI pairs S1–S5, a two-sided Student's t-test was performed to assess statistically significant differentiation of systole and diastole. Significance is indicated by * ($p < 0.05$) and ** ($p < 0.001$), respectively. The peak value of $\nabla \bullet \mathbf{v}$, averaged over all subjects, was $(11.8 \pm 5.8) \cdot 10^{-4}$ s^{-1}. The average minimum value was $(-6 \pm 2.4) \cdot 10^{-4}$ s^{-1}.

To assess global motion of the brain driven by cardiac pulsation, the axial derivatives were averaged over all subjects and all ROIs. The resultant data are shown in fig. 4.20c. Positive values indicate dilatation along a given Cartesian axis, whereas negative values represent compression. The bold line corresponds to the globally averaged velocity field divergence, i.e. it is the sum of the uniaxial derivatives (as given by eq. (4.11)), as well as the average of the curves shown in fig. 4.20a. The velocity field divergence, $\nabla \bullet \mathbf{v}$, was integrated with respect to time to obtain information about the volumetric strain induced by the pulsation. The result is shown in fig. 4.20d. Note

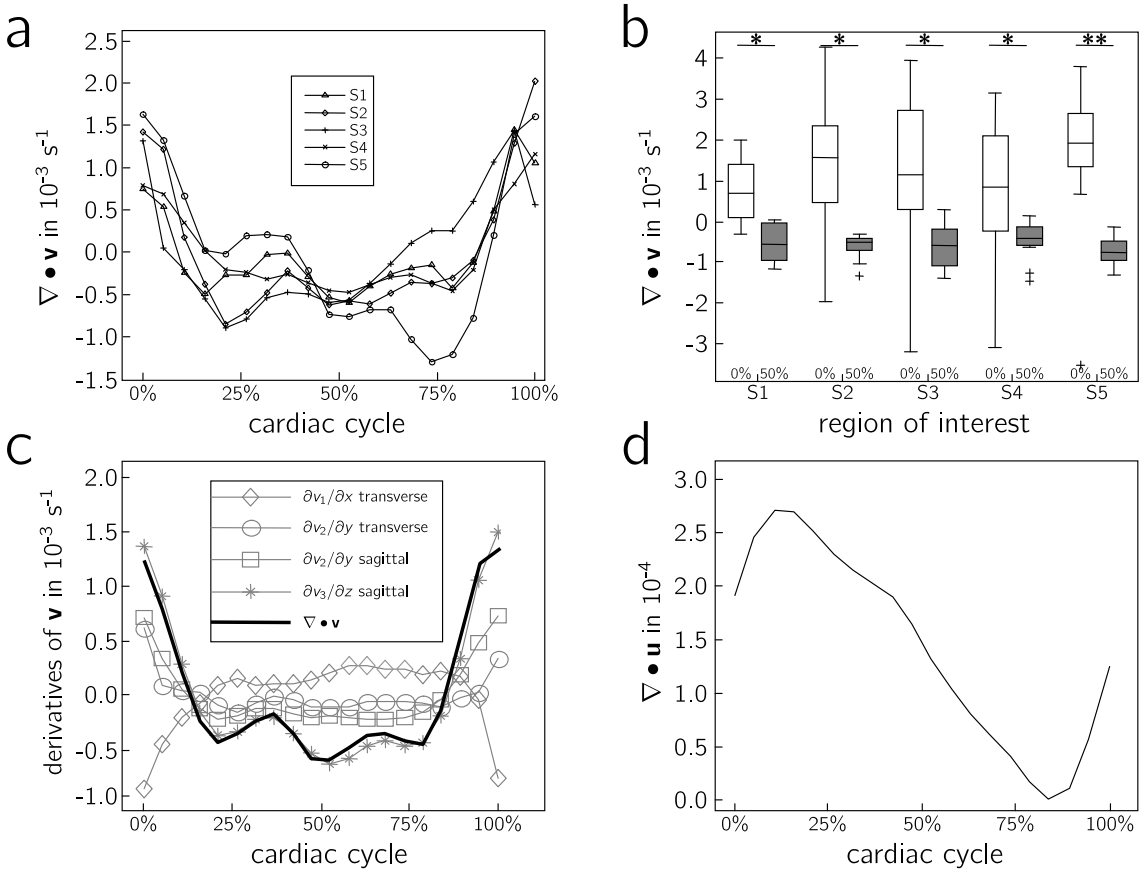

Figure 4.20: Results from the cerebral pulsation study. **a**: Temporal variation of $\nabla \bullet \mathbf{v}(t)$ over the cardiac cycle. Each curve represents mean strain values in one of the regions demarcated in fig. 4.19, averaged over all six volunteers and the two hemispheres. **b**: Variation of $\nabla \bullet \mathbf{v}$ in the regions S1-S5 at the arrival of the arterial pulse wave (0 %, white) and in diastole (50 % of the cardiac cycle, gray). The data are averaged over all subjects. Each column comprises one data point from each of the six volunteers. The boxes extend from the 25$^{\text{th}}$ to the 75$^{\text{th}}$ percentile, crosses mark outliers, whiskers indicate the full data range. The median of each column is indicated by the horizontal line. Significant changes between the two time points are indicated by * ($p < 0.05$) and ** ($p < 0.001$). **c**: Temporal variation of the axial in-plane derivatives, averaged over all ROIs and all volunteers. The bold line, representing $\nabla \bullet \mathbf{v}$, corresponds to the average of all curves shown in (a). **d**: Time integral of the $\nabla \bullet \mathbf{u}$ curve in (c), corresponding to volumetric strain $\nabla \bullet \mathbf{u}$. Note that an arbitrary offset can be added to the curve, since the integration constant is undetermined.

that the constant of integration remains undetermined, allowing an arbitrary offset to be added.

ii) Cardiac-gated MRE

The time course of $|\nabla \bullet \mathbf{u}|$ induced by 25 Hz vibrations over the cardiac cycle is presented for one volunteer in fig. 4.21a. The spatially averaged dilatation reaches it maximum approximately 600 to 700 ms after the pulse wave in the finger[4]. Maps of $|\nabla \bullet \mathbf{u}|$ in the central slice at 200 ms and 600 ms are shown as inlays. These maps appear relatively homogeneous. The same data for all volunteers after normalization of the time axis is shown in fig. 4.21b. Vibration-induced volumetric strain, $|\nabla \bullet \mathbf{u}|$, reaches its maximum amplitude at approximately 20 % of the cardiac cycle. The minimum strain amplitude, averaged over all volunteers, was $(1.2 \pm 0.3) \cdot 10^{-4}$. This value will be considered the baseline. Average peak strain was $(2.7 \pm 1.1) \cdot 10^{-4}$, approximately 2.2 times higher than the baseline. Furthermore, fig. 4.21b illustrates that the time courses of vibration-induced strain amplitudes and native volumetric strain from (i) agree well.

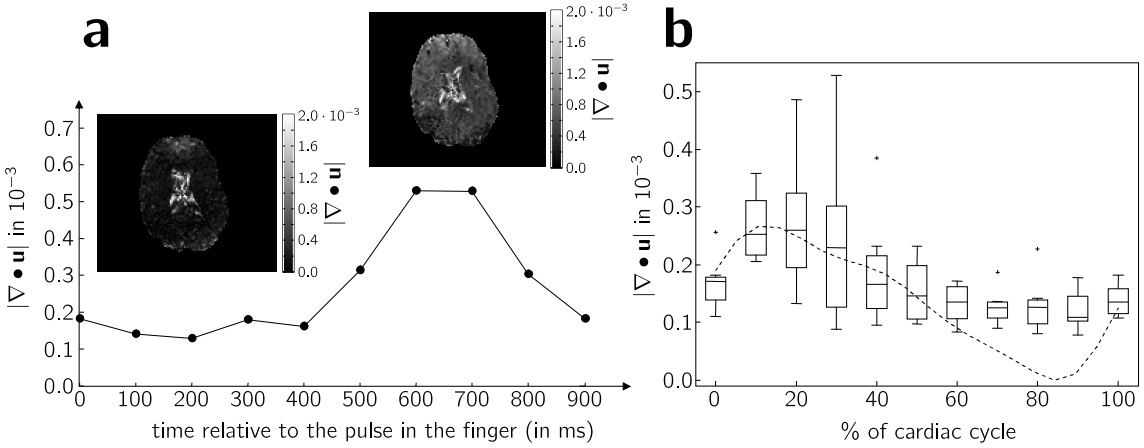

Figure 4.21: Harmonic volumetric strain in the brain relative to the arterial pulse wave (APW). **a**: $|\nabla \bullet \mathbf{u}|$ over the cardiac cycle in one volunteer. The two divergence maps shown represent volumetric strain at 100 ms and 600 ms relative to the finger pulse. **b**: Variation of $|\nabla \bullet \mathbf{u}|$ in eight volunteers relative to cardiac systole. Due to normalization of the time axis, 0 % corresponds to approximately 400 ms in **a**. The dashed line is the time-integrated curve from fig. 4.20d.

[4] More precisely, since the pulse wave travels longer from the heart to the finger than to the brain, the delay refers to the time between the arrival of one pulse wave in the finger to the arrival of the next pulse wave in the brain.

iii) Abdominal muscle contraction

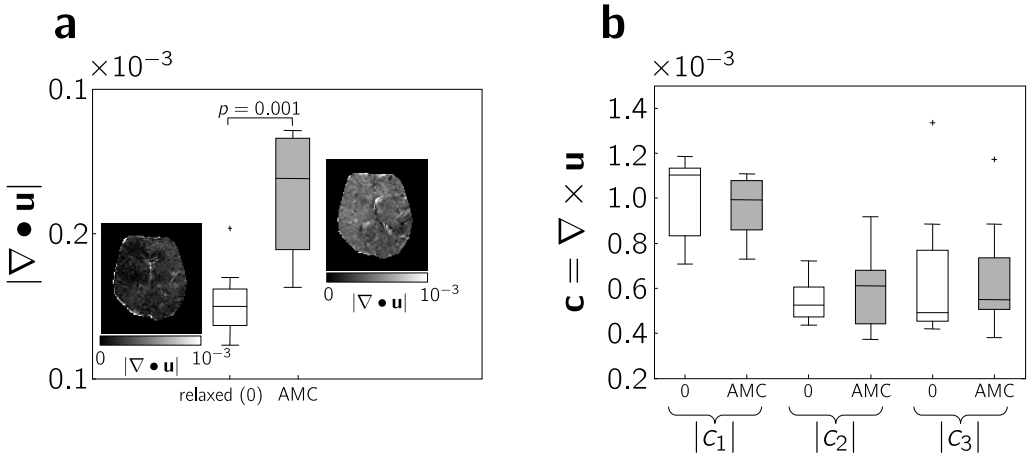

Figure 4.22: Harmonic volumetric strain measured in the brain with compression-sensitive MRE under abdominal muscle contraction (AMC) and in relaxation (0). **a**: Magnitude of the divergence of the harmonic displacement field. **b**: Shear strain, for comparison, represented by the components of the curl of the displacement field. The maps in **a** present results in a single volunteer, relaxed and with AMC, whereas the box plots represent data from eight individuals.

Figure 4.22 presents the amplitude of induced oscillating volumetric strain in all volunteers for the two physiological states, rest and abdominal muscle contraction. The rise of the strain during AMC is clearly visible. Maps of $|\nabla \bullet \mathbf{u}|$ in one volunteer during the two states are displayed as inlays. These strain maps are relatively flat and do not delineate anatomical boundaries (apart from the ventricles, which were excluded from the data analysis). The averaged volumetric strain at rest was $(1.5 \pm 0.3) \cdot 10^{-4}$, and $(2.2 \pm 0.4) \cdot 10^{-4}$ in the AMC state, an increase by a factor of approximately 1.5 ($p = 0.0013$). As a reference, the same comparison was performed for one volunteer in an additional measurement without motion-encoding gradients. In that case, recorded strain levels were about 20-fold lower, and no variation of $|\nabla \bullet \mathbf{u}|$ between the two states was detected. Shear strain, as quantified by $|\mathbf{c}| = |\nabla \times \mathbf{u}|$, was found to be insensitive to the two states, as shown in fig. 4.22b.

In contrast to compression-sensitive MRE, where the magnitude of the complex divergence, $|\nabla \bullet \mathbf{u}|$, is averaged over a region of interest and information about the complex phase is lost, direct inversion of the wave field (eq. (2.63)) yields complex moduli μ and K for each voxel. Their real parts correspond to the reversible elastic component of tissue response to deformation, whereas the imaginary part quanti-

fies the viscous, dissipative properties. The changes of these parameters are plotted in fig. 4.23.

The group-averaged values of the complex shear modulus μ are in good agreement with previously published human brain data acquired at 25 Hz vibration frequency, using 2D MRE instead of 3D MRE (using only the in-plane components of the displacement field) [87]. The real and imaginary part of μ were insensitive toward AMC ($p = 0.959$ and $p = 0.776$, respectively). The direct inversion for the compression modulus resulted in $\mathrm{Re}(K) = (13.59 \pm 5.49)$ kPa (relaxed) and $\mathrm{Re}(K) = (9.50 \pm 2.35)$ kPa (AMC), and very similar values for the imaginary part, with $\mathrm{Im}(K) = (13.83 \pm 5.23)$ kPa (relaxed) and $\mathrm{Im}(K) = (9.79 \pm 2.95)$ kPa (AMC). Both $\mathrm{Re}(K)$ and $\mathrm{Im}(K)$ were lower during AMC in seven out of eight subjects; however, this was statistically not significant ($p = 0.065$ and 0.059, respectively). The estimates for K were used to calculated the magnitude of the induced oscillating pressure according to eq. (2.54), resulting in $|\tilde{P}| = (2.96 \pm 1.20)$ Pa and $|\tilde{P}| = (3.06 \pm 0.74)$ Pa for relaxation and for AMC, respectively. The difference between these values is statistically insignificant ($p = 0.746$).

The most important results from all three brain experiments are summarized in table 4.2.

4.6.4 Discussion

Figure 4.20a illustrates that the arrival of the cardiac pulse wave in the brain causes a global expansion. In the poroelastic model it is assumed that brain parenchyma constitutes the matrix, whereas the blood contained in arterioles and capillaries acts as the fluid phase. Global volume fractions for the whole brain are: 80 % parenchyma, 10 % blood, 10 % cerebro-spinal fluid (CSF) [77]. CSF contributions are neglected, since most CSF is contained in the ventricles, which were not included in the regions of interest. The expansive motion can be interpreted as follows: The cardiac pulse wave is transmitted to arterioles and capillaries via the large arteries. Small vessels expand in response to the rapid increase of blood pressure. The incompressibility assumption of the poroelastic model then requires that the surrounding brain parenchyma is displaced to warrant constant bulk density of the brain. After the passage of the pressure wave, relaxation occurs, during which the vessels return to their original diameter. This phase is characterized by negative values of $\nabla \bullet \mathbf{v}$, indicating a contractive motion of the parenchyma. This behavior is consistent in all five regions S1–S5. Due to the relatively low temporal resolution of 50 ms, the propagation of the

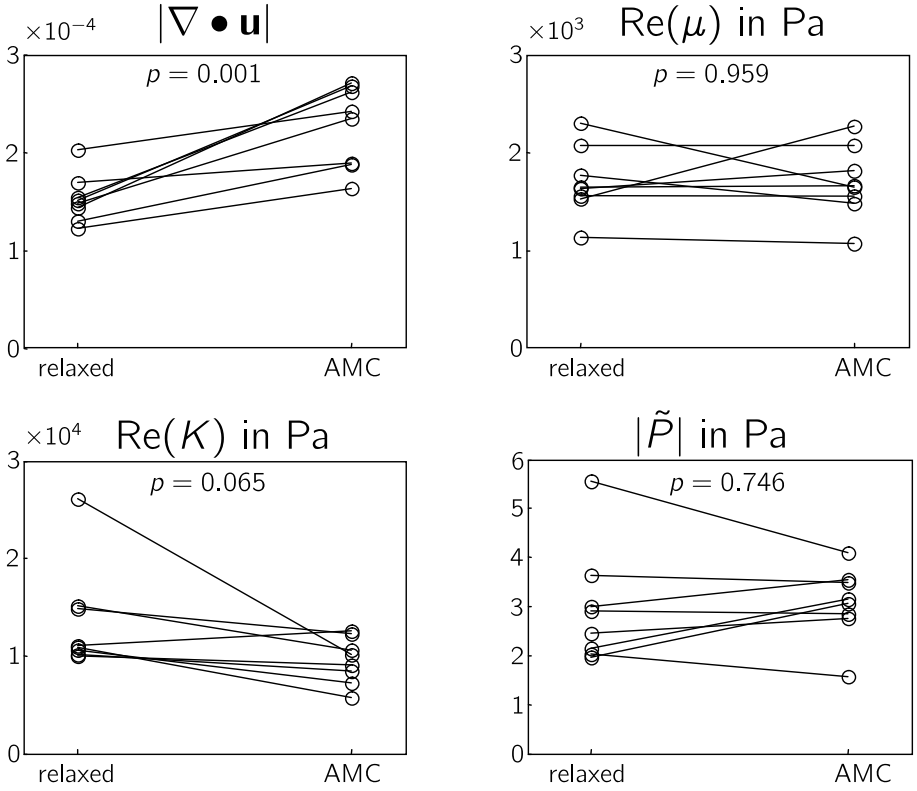

Figure 4.23: Variation of individual parameters obtained from K-MRE in the human brain. The two states correspond to relaxation and abdominal muscle contraction (AMC). Each circle represents the average value in one volunteer, lines connect values from the same volunteer.

pressure wave through the brain could not be tracked by analyzing the relative delays between different regions. Results are summarized in fig. 4.16a, which illustrates the directions of parenchyma motion upon the arrival of the pulse wave. The principal component is directed towards the feet, since this is the only direction that is not obstructed by the cranium. This leads to the funnel-shaped pattern which is consistent with both the data acquired in this study and previous results by Greitz et al. [29] and Weaver et al. [100].

The comparison shown in fig. 4.20b illustrates that the median displacement velocities as well as their variation at the arrival of the systolic pulse wave (0 % of the cardiac cycle) are much larger than during the diastolic relaxation phase (50 %). The differences in $\nabla \bullet \mathbf{v}$ can be explained by the fact that the dilatation is caused by a momentary stimulation, whereas the relaxation is a slow return to a mechanical equilibrium state driven only by internal forces. The high variability of the values in the systolic phase is most likely explained by the fact that every box in the figure summarizes average

	Low pressure state (mean ± SD)	High pressure state (mean ± SD)	p
$\nabla \bullet \mathbf{v}$ (native, APW)	$(-6.0 \pm 2.4) \cdot 10^{-4}$ s^{-1}	$(11.8 \pm 5.8) \cdot 10^{-4}$ s^{-1}	< 0.0001
$\nabla \bullet \mathbf{u}$ (native, APW)	$(0.0 \pm 1.5) \cdot 10^{-4}$ (*)	$(2.8 \pm 1.9) \cdot 10^{-4}$	0.0002
$\lvert\nabla \bullet \mathbf{u}\rvert$ (25 Hz, APW)	$(1.2 \pm 0.3) \cdot 10^{-4}$	$(2.7 \pm 1.1) \cdot 10^{-4}$	< 0.0001
$\lvert\nabla \bullet \mathbf{u}\rvert$ (25 Hz, AMC)	$(1.5 \pm 0.3) \cdot 10^{-4}$	$(2.2 \pm 0.4) \cdot 10^{-4}$	0.0013
Re(μ) (25 Hz, AMC)	1.71 ± 0.35 kPa	1.70 ± 0.37 kPa	0.9588
Im(μ) (25 Hz, AMC)	1.20 ± 0.15 kPa	1.19 ± 0.25 kPa	0.7761
Re(K) (25 Hz, AMC)	13.59 ± 5.49 kPa	9.50 ± 2.35 kPa	0.0649
Im(K) (25 Hz, AMC)	13.83 ± 5.23 kPa	9.79 ± 2.95 kPa	0.0589
$\lvert p\rvert = \lvert K\rvert \cdot \lvert\nabla \bullet \mathbf{u}\rvert$ (25 Hz, AMC)	2.96 ± 1.20 Pa	3.06 ± 0.74 Pa	0.7464

Table 4.2: Main experimental results obtained by compression-sensitive MRI and K-MRE in brain. Values represent the group average ± standard deviation. Low and high pressure states refer to relaxation and arterial pulse wave (APW), or to relaxation and abdominal muscle contraction (AMC), respectively. p refers to the significance level according to Student's t-test. Re(μ), Im(μ), Re(K) and Im(K) refer to the real and imaginary parts of the complex shear modulus and the complex compression modulus, respectively.
(*) Note that the baseline for $\nabla \bullet \mathbf{u}$ in the native pulsation experiment was arbitrarily set to zero.

velocities from all volunteers. The strength of the compression effect is assumed to be correlated with the intensity of cardiac activity, which in turn depends on many factors, such as physical fitness, stress level and emotional state. These properties could not be controlled during the experiment and can thus be expected to vary strongly between the individual subjects in the cohort. Secondly, systole is relatively short compared to diastole, such that the peak of the effect might fall between two sampling points (with a separation of 50 ms) in some measurements, and coincide with a sample point in others.

Figure 4.20c demonstrates that a distortional effect is observable along all three Cartesian directions. The strongest effect occurs along the z (head–feet) direction, which is also reflected in fig. 4.16a. The anterior–posterior component (v_2, along the line from the nose to the back of the head) was measured independently in the sagittal and transverse slices. The two curves (squares and circles in fig. 4.20c) are remarkably similar in terms of their time course and absolute values. The time course of $\nabla \bullet \mathbf{v}$, calculated from the four components according to eq. (4.11), is obviously mainly determined by the motion along the head–feet direction, whereas the other compo-

nents compensate each other.

The time-integrated curve in fig. 4.20d does not provide additional information, but it facilitates comparisons with other studies discussed in this thesis, in which $\nabla \bullet \mathbf{u}$ is assessed directly. The magnitude of $\nabla \bullet \mathbf{u}$ ($\sim 3 \cdot 10^{-4}$) is comparable to values found with external stimulation. However, since intrinsic pulsation occurs at much lower frequencies than stimulated vibration (~1 Hz vs. 25–60 Hz), it contains comparatively little energy.

This study demonstrated that intrinsic pulsation of the brain causes volumetric strain, which can be detected by motion-sensitized acquisition techniques. Findings about tissue motion are consistent with previously published data [29]. Two previous studies by Weaver et al. [100] and Pattison et al. [68] exploited cerebral pulsation as the driving force to perform MR Elastography. However, the processing of their data was focused on the reconstruction of the shear modulus and the pore-pressure distribution, both of which had to be calculated by means of an iterative inversion method based on finite elements. Conversely, in this work, the volumetric strain rate could be readily derived from the measured data without relying on a model-based reconstruction algorithm. Prevost et al. [76] reported moderate compressibility of ex vivo porcine brain in the low frequency range (< 1 Hz), supporting the hypothesis that the brain can undergo significant volumetric strain in the low frequency regime.

At first glance, using intrinsic pulsation rather than externally induced oscillations appears to be less demanding, since no external vibration generator is required. However, the separation of motion information from static phase shifts and through-plane phase gradients – which is achieved by temporal Fourier transform in the case of time-harmonic oscillations – becomes more challenging. Cardiac gating prolongs the scan time significantly (20–30 min vs. 2–4 min for a non-gated measurement). Induced vibrations impose a well-defined time dependence on the tissue, thus permitting inversion of the wave equation.

All pressure values tabulated in table 4.2 relate to the induced oscillating pressure $\tilde{P}$; they do not represent the hydrostatic tissue pressure that an invasive pressure probe would quantify. $|\tilde{P}|$ was found to be virtually unaffected by abdominal muscle contraction. In an effective medium model, a constant compression modulus requires that an increase in strain $|\nabla \bullet \mathbf{u}|$, as observed during AMC, leads to an increase in the oscillation pressure $|\tilde{P}|$ according to eq. (2.54). Since no such rise of $|\tilde{P}|$ was observed, it may be hypothesized that the increase in $|\nabla \bullet \mathbf{u}|$ was instead balanced by a decrease

in the compression modulus itself. In the VST model, this could be caused either by a reduction of the hydrostatic fluid pressure P, or an increase in the fluid volume fraction β. As the purpose of AMC was to increase the venous pressure, a change of the volume fraction is the more likely explanation. Future studies may investigate this aspect by engaging complimentary micro-morphological techniques, such as vessel size imaging [40, 92].

The design of experiment (ii) did not permit the reconstruction of K as a function of the cardiac cycle. More than four wave propagation steps t_d would have been necessary, leading to excessively long scan times. Future research has to investigate the clinical applicability and relevance of compression-sensitive MRI in patients with impaired or imbalanced regulation of cerebral fluid flow, parenchyma pressure vessel diameter, and parenchymal filtration.

In summary, volumetric strain from two different sources could be detected in the human brain. Effects of intrinsic pulsation, as quantified by the divergence of the displacement velocity field, $\nabla\bullet\mathbf{v}$, can be explained by a biphasic effective medium model that accounts for the dilation of fluid spaces. Temporal integration of the displacement velocity yielded pulse-wave-induced volumetric strain of $(2.8\pm1.9)\cdot10^{-4}$, on the same order of magnitude as the harmonic strain amplitude at 25 Hz external stimulation. Under abdominal muscle contraction, an average increase of induced volumetric strain by approximately 45 % was observed. Direct wave inversion resulted in values of $|K|$ on the order of tens of kPa at 25 Hz vibration frequency; this is much lower than what one would expect for a truly monophasic tissue. AMC was found to have a stronger effect on volumetric strain amplitudes than on the compression modulus or the static tissue pressure, so that $|\nabla\bullet\mathbf{u}|$ and $\nabla\bullet\mathbf{v}$ can be regarded as most compression-sensitive parameters accessible through MR Elastography in the human brain. One possible application scenario is non-invasive diagnosis of diseases related to distortions in fluid flow and intracranial pressure regulation, such as hydrocephalus.

5 Discussion

The studies discussed in the previous chapter elucidated different aspects of the technical feasibility and applicability of compression-sensitive MR Elastography. The newly developed MRE sequence, based on the spin echo EPI principle, is superior to established segmented image acquisition strategies in terms of acquisition speed. This benefit can be exploited to either reduce the total examination time for increased patient comfort, or, with the examination time kept constant, more data (e.g. multiple vibration frequencies or a larger 3D volume) than with previous imaging methods can be acquired. EPI has higher hardware requirements than other MR sequences, primarily demanding high gradient performance and duty cycles. However, the sequence was found to perform reliably on a number of different scanners with field strengths between 1.5 and 7 Tesla (Siemens Magnetom Sonata, Magnetom Avanto, Magnetom Trio, Magnetom 7T). The capability to acquire a full image of a single slice in one shot is particularly valuable if physiological triggering, e.g. via ECG or a pulse oximeter, is applied. Segmented sequences typically acquire only a few lines in k-space following each trigger pulse, requiring the final images to be assembled from data collected over multiple heart beats. Image artefacts can arise if organs move between scans, for example due to respiratory motion or bowel activity. This disadvantage is automatically circumvented by using a single-shot sequence.

Despite its advantages, EPI encounters a number of specific issues, especially at field strengths of 3 Tesla and higher. Since an entire two-dimensional k-space is sampled using a single readout train, even slight deviations from the ideal k-space trajectory, which can be caused by imperfections of the gradient hardware, can accumulate and cause severe image artefacts. For the same reason, EPI is particularly sensitive to B_0 field distortions, since they also act as magnetic field gradients and affect the readout k-space trajectory. Those inhomogeneities are usually of minor importance at 1.5 T, but become more prevalent at higher field strengths. Due to the symmetry property of spin echo EPI (the duration of the readout train determines the echo time), echo

times have to be significantly longer than for segmented sampling strategies. This means that the maximum attainable signal amplitude is reduced, due to ongoing T_2 decay. Since T_2 shortens at higher field strengths, this could potentially pose a challenge at 3 Tesla and above. However, in addition to the measurements presented in this work, which were all performed on a 1.5 T scanner, other studies carried out on 3 T and 7 T scanners encountered no issues at either field strength. The sequence has been successfully tested on a 7 Tesla scanner in collaboration with Ralf Lützkendorf and Johannes Bernarding from the Department for Biometry and Medical Informatics at the University of Magdeburg [10]. Despite the sensitivity of EPI toward magnetic field inhomogeneities, the results were superior and their unprecedented spatial resolution of $1 \times 1 \times 1$ mm^3 has inspired the term "high resolution MRE".

The phantom study serves as a verification that compression-sensitive MRE, combining the single-shot EPI sequence with appropriate post-processing of the resultant MR phase images, is actually capable of quantifying volumetric strain. However, with low strain amplitudes and long wave lengths compared to "conventional" shear-waved based MRE, signal noise becomes a severe limitation. To quantify the effect of noise, a numerical simulation was performed for a planar wave with a frequency of 50 Hz traveling through a homogeneous medium with $M = 1$ MPa and a density of 1 g/cm^3. The complex-valued displacement field $\mathbf{u}$ caused by such a wave was calculated, and increasing levels of Gaussian noise were added. The pressure-wave modulus M was then reconstructed from the noisy data using eq. (2.50). Two different methods for the calculation of spatial derivatives were employed: standard symmetric differences, which is routinely used by the `gradient` function in Matlab [59], and the three-dimensional averaging difference scheme suggested by Anderssen and Hegland [2] (see eq. (4.5)). The noise level was defined as $\sqrt{2}\,s/A \cdot 100\,\%$, where s is the standard deviation of the Gaussian noise added to the real and imaginary part of $\mathbf{u}$ and A is the amplitude of $\mathbf{u}$. The reconstructed values of M are plotted as a function of the noise level in fig. 5.1.

It is obvious that symmetric differences possess no noise robustness whatsoever; even small quantities of noise cause a drastic decrease of the reconstructed modulus. The Anderssen-Hegland scheme, on the other hand, also displays a systematic underestimation of the modulus in the presence of noise, but the decrease occurs at a much slower rate. Visual comparison of the experimental wave data to the simulated data suggests that the measurement provided a noise level in the range of 10–15 %,

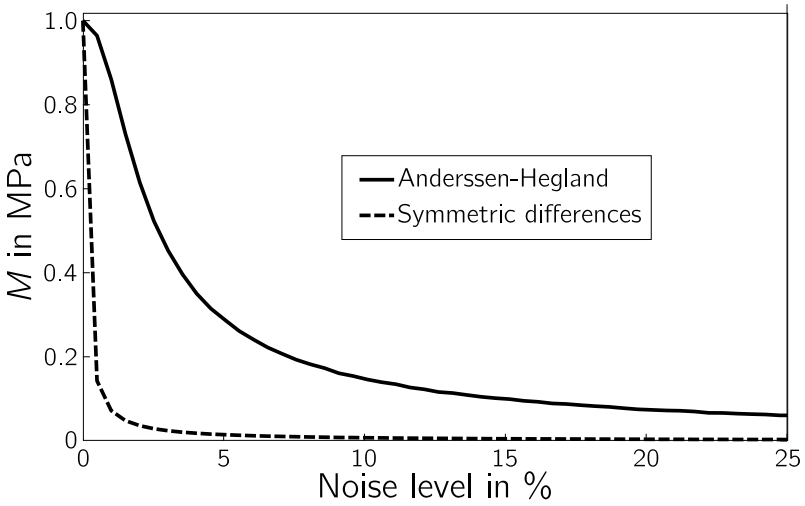

Figure 5.1: Results of numerical simulations to assess the noise sensitivity of the reconstruction of the pressure-wave modulus M. Gaussian noise at different levels was added to the displacement field of a 50 Hz pressure wave traveling through a homogeneous medium with $M = 1$ MPa. Spatial derivatives were either calculated using standard symmetric differences (dashed) or using the scheme published in [2] (see eq. (4.5)).

corresponding to an underestimation of M by 80–90 % of its actual value. As previously discussed, the presence of noise has a higher impact on the third-order spatial derivatives in the denominator of the inverted wave equation eq. (2.50) than on the first-order derivative in the nominator. Following spatial averaging of the magnitude of the complex data prior to the inversion, noise tends to increase the denominator more than the nominator, thus resulting in small values for the modulus.

Several strategies could be proposed to remedy modulus underestimation. Noise levels can be decreased by repeating the measurement and averaging the data prior to processing. However, the signal-to-noise ratio is proportional to the square root of the measurement time [17], such that a single repetition of the measurement would decrease the noise level by a factor $\sqrt{2} \approx 1.41$, whereas the scan time would double. Patient comfort considerations therefore limit the viability of this strategy. Since the SNR is also proportional to the volume of a single voxel, reducing the image resolution can contribute to an increase in signal quality. The disadvantage of a coarser image resolution manifests itself in the numerical calculation of spatial derivatives, which require a narrow spacing between sampling points. Balancing those conflicting demands and finding a local optimum of signal quality within the viable measurement parameter space could improve the data quality in future studies.

The first in vivo application of the novel technique described here to the human lung proved the EPI-based MRE sequence capable of providing sufficient image quality even in difficult-to-image organs if certain compromises are accepted. Since short echo times are crucial to pulmonary imaging, motion encoding sensitivity had to be sacrificed in favor of an echo time reduction. A total of twelve repetitions for signal averaging had to be performed. However, because of the high acquisition speed of the sequence, this was still possible within an acceptable scan time. Data evaluation was focused on the distribution of the volumetric strain amplitude. Inversion of the pressure wave equation was not attempted, as it would have encountered the same noise-related issues as discussed above. Inspiration and expiration were found to be clearly distinguishable based on spatially averaged values of $|\nabla \bullet \mathbf{u}|$ in seven out of nine volunteers. However, the variability of strain amplitudes between individuals hindered quantitative comparisons. This issue does not arise in conventional MRE, wherein the distribution of elastic moduli is recovered either from inversion of the wave equation or an iterative finite elements model reconstruction. Being a homogeneous linear differential equation, the wave equation is invariant under scaling of the wave amplitude. If quantitative values are desired in a study that does not rely on inversion of the wave equation, other means of handling different strain amplitudes would need to be considered. A possible solution for future applications might be to include a reference region in the imaging volume as a normalization region for the strain. If different physiological states are investigated in each individual, taking the ratios of the strain in those states for each subject can establish a quantitative marker, as shown in section 4.4.3.

Compression-sensitive MRE in a poroelastic context was performed on the ovine liver. By using an ex vivo organ it became possible to adjust the pressure conditions during the measurement and to repeat the examinations at several well-defined levels. The results clearly indicate that volumetric strain, in contrast to shear strain, is a pressure-sensitive quantity. However, since ex vivo tissue lacks any self-regulatory mechanisms that might exist in living tissue, the results from the experiment alone do not permit any conclusions on the response of actual liver tissue to instantaneous pressure changes to be drawn. Secondly, the pressure in the experiment was increased within a few seconds, whereas in hepatic portal hypertension, pressure build-up is a slow and steady process. As a disease, portal hypertension is accompanied by structural changes in the vascular tissue of the liver, causing a partial obstruction of blood flow. These effects could not be emulated in the experiment. Neverthe-

less, the findings are consistent with the results reported in [35], which saw a decrease in volumetric strain in human patients with portal hypertension after pressure had been relieved by means of a TIPS intervention.

Ultimately, the brain pulsation study demonstrated that volumetric strain can be quantified even in the absence of external stimulations. The passage of the cardiac pulse wave through the brain proved to be sufficiently strong to have a measurable effect in terms of brain parenchyma displacement. This finding agrees well with data published by Pattison et al. [68] and Weaver et al. [100]. The reconstructed principal directions of parenchyma motion over the cardiac cycle confirmed the results of Greitz et al. [29]. The cardiac-gated MRE study and the abdominal muscle contraction study indicated that compression-sensitive MRE possesses sensitivity to pressure changes on time scales much shorter than those associated with chronic diseases such as hepatic hypertension and normal pressure hydrocephalus. These results demonstrated for the first time that compression-sensitive MRE might be a promising instrument for elucidating the complex interaction patterns between cerebro-spinal fluid pressure and brain parenchyma.

The responses of different organs to pressure alterations were found to diverge. Although an increase in stimulated volumetric strain with increased hydrostatic pressure was found in the IGC phantom, the lung and the brain, the opposite effect was observed in both the ex vivo ovine liver and the in vivo human liver. Our interpretation is that there is not a single universal model that predicts the response of organic tissue to static pressure in general. The source of the pressure must be considered – internal gas pressure in the lung, arterial pulsation in the brain, venous blood pressure in the liver – as well as the particular architecture of an organ. Whereas arteries are surrounded by muscles that can actively change the vessel diameter and thereby contribute to pressure regulation, veins do not possess such a mechanism and are purely passive. Consequently, pressure autoregulation mechanisms in different organs may depend on the number and size of arteries and veins they are attached to.

In conclusion, this thesis presents a number of experiments that confirm the viability of compression-sensitive MRE in different human organs and assesses its sensitivity towards intrinsic or externally controlled pressure states. It lays the foundation for future research into clinical applications of this novel technique, with the ultimate goal of non-invasive pressure quantification.

6 Future perspectives

The single-shot MRE EPI sequence has proven its potential and suitability in numerous studies performed by the Elastography group at the Charité. In addition to the studies described in this work, various other examinations have been performed with the sequence, and it has fully replaced prior MRI sequences based on FLASH and balanced SSFP principles. Since data acquisition is strictly decoupled from image post-processing, the sequence is not limited to compression-sensitive MRE, but can equally be used for shear-wave MRE or related applications.

Currently, there are three major fields of application for compression-sensitive MRE:

1. *Volumetric strain as a marker of physiological state:* This was the main objective of this thesis. As discussed earlier, volumetric strain amplitudes depend on a number of parameters (physique, amplifier output level, vibration frequency, coupling strength), some of which are difficult to control during the experiment. Consequently, strain amplitudes are not comparable between different individuals. However, if the measurement is repeated with identical settings on the same person in different physiological states (e.g. inspiration vs. expiration or several phases of the cardiac cycle), those parameters can be assumed to remain constant, such that strain amplitudes acquired in different states are indicative of physiological changes. Methods for normalizing volumetric strain require further development. For instance, if the region of interest can be chosen to include not only the affected organ but also some tissue that does not undergo the same physiological changes, the averaged strain amplitude from that region could potentially be used as a normalization factor.

2. *Elastic modulus reconstruction:* Inversion of the wave equation as a means for deriving the pressure field has been discussed in this work. As a result, the P-wave modulus M is obtained, which can be converted to the compression mod-

ulus K if the shear modulus μ is also known, e.g. from inversion of the shear wave field. However, the data analysis performed in this work showed that a high noise sensitivity is a major obstacle for this technique. Pressure field inversion requires third-order spatial derivatives. Since pressure waves have minor curvature, noise has a stronger impact on the inversion of the wave equation than in shear-wave based MRE. As discussed in the previous section, adaptions of the measurement protocol might lead to higher signal-to-noise ratios at the cost of increased scan times and/or reduced spatial resolution.

3. *Non-invasive pressure quantification:* An image-based procedure for pressure measurements would be an immensely helpful tool for diagnosis, staging and therapy screening in many clinical situations. Pattison et al. showed the general feasibility of calculating pore-pressure distribution maps [68] using a finite element iterative solving algorithm. However, no verification of the pressure data was presented in their work. To obtain quantitative pore pressure values, poroelastic wave equations have to be solved [8], which depend not only on the shear modulus μ and the first Lamé parameter λ, but also on several material constants that characterize flow resistance and the coupling strength between the two phases. The high number of parameters renders solving the equation challenging and it remains to be investigated if some or all of them can be replaced with empirical constants. Furthermore, these equations also rely on third-order derivatives of the displacement field, leading to the same level of noise sensitivity as discussed for the wave equation.

The clinical relevance of each of these applications will have to be evaluated. The TIPS patient study discussed in section 4.5.4 indicated the potential of volumetric strain analysis to differentiate between different pressure states in the liver. More studies on other pathologies will have to follow to complete our understanding and to establish clinical scenarios for the application of compression-sensitive MRE.

Contributions

The following list denotes contributions from colleagues to the work described in this thesis:

- *Sebastian Papazoglou* contributed theoretical background for the inversion of the wave equation and provided eq. (2.51).
- *Frauke Beyer* performed the rheometer experiments described in section 4.3.2 and optimized the recipe for phantoms with gas-filled inclusions.
- *Jing Guo, Rolf Reiter* and *Thomas Kröncke* conducted the study on patients with hepatic portal hypertension before and after TIPS placement.

Nomenclature

Greek symbols

β	porosity (volume fraction of the fluid or gas phase)
γ	gyromagnetic ratio of a proton ($\gamma = 2\pi \cdot 42.58$ MHz/T)
μ	shear modulus
$\boldsymbol{\epsilon}$	strain tensor
$\boldsymbol{\sigma}$	stress tensor
$\boldsymbol{\mu}$	magnetic moment of a single proton
Ω	Mechanical vibration frequency
ω_0	Larmor frequency / spin precession frequency due to $\mathbf{B}_0$
ϕ	precession phase of a spin / phase of the complex MR signal from a voxel

Latin symbols

$\hat{\mathbf{n}}_i$	unit vector along the i-th Cartesian axis
$\hat{\mathbf{x}}$, $\hat{\mathbf{y}}$, $\hat{\mathbf{z}}$	unit vectors along the x, y and z direction
$\mathbf{B}_0$	static magnetic field of the MR scanner (aligned with the z-axis)
$\mathbf{M}$	total magnetization vector
$\mathbf{M}_0$	resultant equilibrium magnetization

$\mathbf{M}_{\parallel}$	longitudinal magnetization component
$\mathbf{M}_{\perp}$	transverse magnetization component
$\mathbf{u}(x,y,z)$ or $\mathbf{u}(\mathbf{r})$	displacement field
$\mathbf{v}(x,y,z)$ or $\mathbf{v}(\mathbf{r})$	displacement velocity field
$\tilde{P}$	oscillating pressure
K	compression/bulk modulus
P	gas/hydrostatic pressure
p	p-value of statistical significance tests

Abbreviations

TE	Echo time
TR	Repetition time
APW	Arterial pulse wave
CSF	Cerebro-spinal fluid
ECG	Electrocardiogram
EPI	Echo-planar imaging (MRI sequence)
FFT	Fast Fourier transform
FLASH	Fast low-angle shot (MRI sequence)
HVPG	Hepatic venous pressure gradient
IGC	Isolated gas-filled cavities model
MEG	Motion-encoding gradient
NPH	Normal Pressure Hydrocephalus

PC-MRI	Phase-contrast MRI
ROI	Region of interest
SNR	Signal-to-noise ratio
SSFP	Steady-state free precession (MRI sequence)
TTL	Transistor-transistor logic
VST	Vascular soft tissue model

Appendix A

A.1 Proof that eq. (2.29) is sinosoidal

Section 2.2.1 uses the fact that

$$\phi(\varphi) = \gamma\, \mathbf{u}_0 \bullet \mathbf{G}_0 \cdot \int_0^T \sin(\Omega t + \varphi) \cdot \sin(\omega_G t)\, \mathrm{d}t$$

is a sinusoidal function with respect to φ. As a proof, it will be shown that

$$g(\varphi) = \int_{t_0}^{t_1} \sin(t + \varphi) \cdot f(t)\, \mathrm{d}t$$

is sinusoidal for an any real-valued integrable function $f(t)$ and arbitrary limits $t_0 \neq t_1$.

Proof: Taking the second derivative of g with respect to φ yields

$$\begin{aligned} \frac{\mathrm{d}^2 g}{\mathrm{d}\varphi^2} &= \frac{\partial^2}{\partial \varphi^2} \int_{t_0}^{t_1} \sin(t + \varphi) \cdot f(t)\, \mathrm{d}t \\ &= -\int_{t_0}^{t_1} \sin(t + \varphi) \cdot f(t)\, \mathrm{d}t \\ &= -g(\varphi), \end{aligned} \tag{A.1}$$

which is a second-order differential equation with two linearly independent real-valued solutions $\sin(\varphi)$ and $\cos(\varphi)$, both of which are sinusoidal. They constitute a complete basis of the solution space, such that any solution to eq. (A.1) is a linear combination of these, and therefore is sinusoidal itself. ■

A.2 Proof for eq. (2.34)

To be shown:

$$\sum_{j=1}^{3} \frac{\partial u_i}{\partial r_j} \delta r_j = \frac{1}{2} \sum_{j=1}^{3} \left(\frac{\partial u_i}{\partial r_j} + \frac{\partial u_j}{\partial r_i} \right) \delta r_j + \frac{1}{2} ((\nabla \times \mathbf{u}) \times \delta \mathbf{r})_i \tag{A.2}$$

Proof: The cross product can be expressed in index notation as

$$(\mathbf{a} \times \mathbf{b})_i = \sum_{j,k=1}^{3} \epsilon_{ijk} a_j b_k \tag{A.3}$$

with the totally antisymmetric *Levi-Civita tensor* ϵ_{ijk}. Translating the last term in eq. (A.2) to this notation yields

$$\begin{aligned} \frac{1}{2} ((\nabla \times \mathbf{u}) \times \delta \mathbf{r})_n &= \frac{1}{2} \sum_{i,m=1}^{3} \underbrace{\sum_{j,k=1}^{3} \epsilon_{ijk} \frac{\partial u_k}{\partial r_j}}_{(\nabla \times \mathbf{u})_i} \epsilon_{nim} \delta r_m \\ &= \frac{1}{2} \sum_{i,j,k,m=1}^{3} \epsilon_{ijk} \epsilon_{imn} \frac{\partial u_k}{\partial r_j} \delta r_m. \end{aligned} \tag{A.4}$$

In the second step, the fact that ϵ_{abc} is invariant under cyclic permutations of the indices was used: $\epsilon_{abc} = \epsilon_{bca} = \epsilon_{cab}$. Equation (A.4) can be further simplified by contracting the two $\boldsymbol{\epsilon}$ tensors over the common index i:

$$\sum_{i=1}^{3} \epsilon_{ijk} \epsilon_{imn} = \delta_{jm} \delta_{kn} - \delta_{jn} \delta_{km}. \tag{A.5}$$

Substituting eq. (A.5) into eq. (A.4) yields

$$\begin{aligned} \frac{1}{2} ((\nabla \times \mathbf{u}) \times \delta \mathbf{r})_n &= \frac{1}{2} \sum_{j,k,m=1}^{3} \left(\delta_{jm} \delta_{kn} - \delta_{jn} \delta_{km} \right) \frac{\partial u_k}{\partial r_j} \delta r_m \\ &= \frac{1}{2} \sum_{m=1}^{3} \left(\frac{\partial u_n}{\partial r_m} \delta r_m - \frac{\partial u_m}{\partial r_n} \delta r_m \right) \end{aligned} \tag{A.6}$$

After performing the index substitution $n \to i$ and $m \to j$, eq. (A.6) can be substituted

into the right hand side of eq. (A.2):

$$\begin{aligned}
&\frac{1}{2}\sum_{j=1}^{3}\left(\frac{\partial u_i}{\partial r_j}+\frac{\partial u_j}{\partial r_i}\right)\delta r_j+\frac{1}{2}((\nabla\times\mathbf{u})\times\delta\mathbf{r})_i \\
=&\frac{1}{2}\sum_{j=1}^{3}\left(\frac{\partial u_i}{\partial r_j}+\frac{\partial u_j}{\partial r_i}+\frac{\partial u_i}{\partial r_j}-\frac{\partial u_j}{\partial r_i}\right)\delta r_j \\
=&\sum_{j=1}^{3}\frac{\partial u_i}{\partial r_j}\delta r_j
\end{aligned}$$

■

List of Figures

List of Tables

Bibliography

[1] K. Aki and P. G. Richards. *Quantitative Seismology*. University Science Books, Sausalito, 2nd edition, 2002.

[2] R. S. Anderssen and M. Hegland. For Numerical Differentiation Dimensionality Can be a Blessing. *Mathematics of Computation*, 68(227):1121–41, 1999.

[3] M. A. Bernstein, K. F. King, and X. J. Zhou. *Handbook of MRI Pulse Sequences*. Elsevier Academic Press, 2004.

[4] G. P. Berry, J. C. Bamber, C. G. Armstrong, N. R. Miller, and P. E. Barbone. Towards an acoustic model-based poroelastic imaging method: I. Theoretical foundation. *Ultrasound in Medicine and Biology*, 32(4):547–67, Apr. 2006.

[5] G. P. Berry, J. C. Bamber, N. R. Miller, P. E. Barbone, N. L. Bush, and C. G. Armstrong. Towards an acoustic model-based poroelastic imaging method: II. experimental investigation. *Ultrasound in Medicine and Biology*, 32(12):1869–85, Dec. 2006.

[6] M. A. Biot. General Theory of Three-Dimensional Consolidation. *Journal of Applied Physics*, 12(2):155–64, 1941.

[7] M. A. Biot. Theory of Elasticity and Consolidation for a Porous Anisotropic Solid. *Journal of Applied Physics*, 26(2):182–85, 1955.

[8] M. A. Biot. Theory of Propagation of Elastic Waves in a Fluid-Saturated Porous Solid. I. Low-Frequency Range. *The Journal of the Acoustical Society of America*, 28(2):168–78, 1956.

[9] M. A. Biot. Theory of Propagation of Elastic Waves in a Fluid-Saturated Porous Solid. II. Higher Frequency Range. *The Journal of the Acoustical Society of America*, 28(2):179–91, 1956.

[10] J. Braun, J. Guo, R. Lützkendorf, J. Stadler, S. Papazoglou, S. Hirsch, I. Sack, and J. Bernarding. High-resolution mechanical imaging of the human brain by three-dimensional multifrequency magnetic resonance elastography at 7T. *Neuroimage*, 90:308–14, 2014.

[11] D. J. Bryant, J. A. Payne, D. N. Firmin, and D. B. Longmore. Measurement of Flow with NMR Imaging Using a Gradient Pulse and Phase Difference Technique. *Journal of Computer Assisted Tomography*, 8(4):588–93, 1984.

[12] P. L. Chambré. Speed of a Plane Wave in a Gross Mixture. *The Journal of the Acoustical Society of America*, 26(3):329–31, 1954.

[13] M. Decramer, W. Janssens, and M. Miravitlles. Chronic obstructive pulmonary disease. *Lancet*, 379(9823):1341–51, Apr. 2012.

[14] M. A. Dresner, G. H. Rose, P. J. Rossman, R. Muthupillai, A. Manduca, and R. L. Ehman. Magnetic Resonance Elastography of Skeletal Muscle. *Journal of Magnetic Resonance Imaging*, 13(2):269–76, 2001.

[15] C. L. Dumoulin and H. R. Hart. Magnetic Resonance Angiography. *Radiology*, 161(3):717–20, Dec. 1986.

[16] C. L. Dumoulin, S. P. Souza, M. F. Walker, and W. Wagle. Three-Dimensional Phase Contrast Angiography. *Magnetic Resonance in Medicine*, 9(1):139–49, Jan. 1989.

[17] W. A. Edelstein, G. H. Glover, C. J. Hardy, and R. W. Redington. The Intrinsic Signal-to-Noise Ratio in NMR Imaging. *Magnetic Resonance in Medicine*, 3(4):604–18, Aug. 1986.

[18] T. Elgeti, J. Rump, U. Hamhaber, S. Papazoglou, B. Hamm, J. Braun, and I. Sack. Cardiac Magnetic Resonance Elastography: Initial Results. *Investigative Radiology*, 43(11):762–72, 2008.

[19] D. R. Enzmann and N. J. Pelc. Brain Motion: Measurement with Phase-Contrast MR Imaging. *Radiology*, 185(3):653–60, 1992.

[20] T. Ernst, R. Kreis, and B. D. Ross. Absolute Quantitation of Water and Metabolites in the Human Brain. 1. Compartments and Water. *Journal of Magnetic Resonance B*, 102(1):1–8, 1993.

[21] J. P. Felmlee, P. J. Rossman, R. Muthupillai, A. Manduca, V. Dutt, and R. L. Ehman. Magnetic Resonance Elastography of the Brain: Preliminary In Vivo Results. In *Proceedings of the 5th Annual Meeting of ISMRM*, page 683, Vancouver, 1997.

[22] M. Fog. Cerebral circulation II. Reaction of pial arteries to increase in blood pressure. *Archives of Neurology & Psychiatry*, 109(1):109–18, 1939.

[23] G. Garcia-Tsao, R. J. Groszmann, R. L. Fisher, H. O. Conn, C. E. Atterbury, and M. Glickman. Portal Pressure, Presence of Gastroesophageal Varices and Variceal Bleeding. *Hepatology*, 5(3):419–24, 1985.

[24] D. C. Ghiglia and M. D. Pritt. *Two-Dimensional Phase Unwrapping: Theory, Algorithms, and Software*. John Wiley & Sons, 1998.

[25] K. Golenhofen. *Basislehrbuch Physiologie*. Elsevier Urban & Fischer, 4th edition, 2006.

[26] K. F. Graff. *Wave Motion in Elastic Solids*. Dover Publications, New York, 1st edition, 1991.

[27] M. A. Green, L. E. Bilston, and R. Sinkus. In vivo brain viscoelastic properties measured by magnetic resonance elastography. *NMR in Biomedicine*, 21(7):755–64, 2008.

[28] D. Greitz. Radiological assessment of hydrocephalus: new theories and implications for therapy. *Neurosurgical Review*, 27(3):145–65, 2004.

[29] D. Greitz, R. Wirestam, A. Franck, B. Nordell, C. Thomsen, and F. Stahlberg. Pulsatile brain movement and associated hydrodynamics studied by magnetic resonance phase imaging. *Neuroradiology*, 34(5):370–80, 1992.

[30] E. M. Haacke, R. W. Brown, M. R. Thompson, and R. Venkatesan. *Magnetic Resonance Imaging: Physical Principles and Sequence Design*. John Wiley & Sons, New York, 1999.

[31] H. Haken and H. C. Wolf. *Atom- und Quantenphysik*. Springer, 8th edition, 2004.

[32] U. Hamhaber, I. Sack, S. Papazoglou, J. Rump, D. Klatt, and J. Braun. Three-dimensional analysis of shear wave propagation observed by in vivo magnetic resonance elastography of the brain. *Acta Biomaterialia*, 3(1):127–37, Jan. 2007.

[33] L. G. Hanson. Is Quantum Mechanics Necessary for Understanding Magnetic Resonance? *Concepts In Magnetic Resonance*, 32A(5):329–40, 2008.

[34] S. Hirsch, F. Beyer, J. Guo, S. Papazoglou, H. Tzschätzsch, J. Braun, and I. Sack. Compression-sensitive magnetic resonance elastography. *Physics in Medicine and Biology*, 58(15):5287–99, Aug. 2013.

[35] S. Hirsch, J. Guo, R. Reiter, E. Schott, R. Somasundaram, J. Braun, I. Sack, T. J. Kroencke, and C. Büning. Towards Compression-Sensitive Magnetic Resonance Elastography of the Liver: Sensitivity of Harmonic Volumetric Strain to Portal Hypertension. *Journal of Magnetic Resonance Imaging*, 39(2):298–306, Feb. 2014.

[36] S. Hirsch, O. Posnansky, S. Papazoglou, T. Elgeti, J. Braun, and I. Sack. Measurement of vibration-induced volumetric strain in the human lung. *Magnetic Resonance in Medicine*, 69(3):667–74, Mar. 2013.

[37] L. Huwart, F. Peeters, R. Sinkus, L. Annet, N. Salameh, L. C. ter Beek, Y. Horsmans, and B. E. Van Beers. Liver fibrosis: non-invasive assessment with MR elastography. *NMR in Biomedicine*, 19(2):173–9, May 2006.

[38] M. Kaczmarek, R. P. Subramaniam, and S. R. Neff. The hydromechanics of hydrocephalus: steady-state solutions for cylindrical geometry. *Bulletin of Mathematical Biology*, 59(2):295–323, 1997.

[39] J. Kemper, R. Sinkus, J. Lorenzen, C. Nolte-Ernsting, A. Stork, and G. Adam. MR elastography of the prostate: initial in-vivo application. *RöFo: Fortschritte auf dem Gebiete der Röntgenstrahlen und der Nuklearmedizin*, 176(8):1094–99, 2004.

[40] V. G. Kiselev, R. Strecker, S. Ziyeh, O. Speck, and J. Hennig. Vessel Size Imaging in Humans. *Magnetic Resonance in Medicine*, 53(3):553–63, 2005.

[41] D. Klatt, P. Asbach, J. Rump, S. Papazoglou, R. Somasundaram, J. Modrow, J. Braun, and I. Sack. In Vivo Determination of Hepatic Stiffness Using Steady-State Free Precession Magnetic Resonance Elastography. *Investigative Radiology*, 41(12):841–48, 2006.

[42] D. Klatt, U. Hamhaber, P. Asbach, J. Braun, and I. Sack. Noninvasive assessment of the rheological behavior of human organs using multifrequency MR

elastography: a study of brain and liver viscoelasticity. *Physics in Medicine and Biology*, 52(24):7281–94, Dec. 2007.

[43] E. E. Konofagou, T. P. Harrigan, J. Ophir, and T. A. Krouskop. Poroelastography: Imaging the Poroelastic Properties of Tissues. *Ultrasound in Medicine and Biology*, 27(10):1387–97, 2001.

[44] S. A. Kruse, M. A. Dresner, P. J. Rossman, J. P. Felmlee, C. R. Jack, and R. L. Ehman. Palpation of the Brain using Magnetic Resonance Elastography. In *Proceedings of the 7th Annual Meeting of ISMRM*, page 258, Philadelphia, 1999.

[45] S. A. Kruse, R. C. Grimm, D. S. Lake, A. Manduca, and R. L. Ehman. Fast EPI Based 3D MR Elastography of the Brain. In *Proceeding of the 14th Annual Meeting of ISMRM*, page 3385, Seattle, 2006.

[46] W. M. Lai, D. Rubin, and E. Krempl. *Introduction to Continuum Mechanics*. Butterworth Heinemann Ltd, 3rd edition, 1993.

[47] L. D. Landau and E. M. Lifschitz. *Theory of elasticity*. Pergamon Press, Oxford, 3rd edition, 1986.

[48] E. Lee, J.-Z. Wang, and R. Mezrich. Variation of lateral ventricular volume during the cardiac cycle observed by MR imaging. *American Journal of Neuroradiology*, 10(6):1145–49, 1989.

[49] R. Leiderman, P. E. Barbone, A. A. Oberai, and J. C. Bamber. Coupling between elastic strain and interstitial fluid flow: ramifications for poroelastic imaging. *Physics in Medicine and Biology*, 51(24):6291–313, Dec. 2006.

[50] R. M. Lerner, S. R. Huang, and K. J. Parker. "Sonoelasticity" Images Derived From Ultrasound Signals in Mechanically Vibrated Tissues. *Ultrasound in Medicine and Biology*, 16(3):231–39, 1990.

[51] D. N. Levine. The Pathogenesis of Normal Pressure Hydrocephalus: A Theoretical Analysis. *Bulletin of Mathematical Biology*, 61(5):875–916, 1999.

[52] Z.-P. Liang and P. C. Lauterbur. *Principles of Magnetic Resonance Imaging*. IEEE Press, Piscataway, NJ, 2000.

[53] J. Lorenzen, R. Sinkus, D. Schrader, M. Lorenzen, C. Leussler, M. Dargatz, and P. Röschmann. Darstellung von Tumoren der weiblichen Brust mit MR-Elastographie. *RöFo: Fortschritte auf dem Gebiete der Röntgenstrahlen und der Nuklearmedizin*, 173:12–17, 2001.

[54] P. Mansfield. Multi-planar image formation using NMR spin echoes. *Journal of Physics C: Solid State Physics*, 10(3):L55–L58, 1977.

[55] Y. K. Mariappan, K. J. Glaser, and R. L. Ehman. Magnetic Resonance Elastography: A Review. *Clinical Anatomy*, 23(5):497–511, 2010.

[56] Y. K. Mariappan, K. J. Glaser, R. D. Hubmayr, R. L. Ehman, and K. P. McGee. MR Elastography of Human Lung Parenchyma: Feasibility of Echo-Planar and Respiratory-Triggered Echo-Planar Imaging. In *Proceedings of the 20th Annual Meeting of ISMRM*, page 3970, Melbourne, 2012.

[57] Y. K. Mariappan, K. J. Glaser, R. D. Hubmayr, A. Manduca, R. L. Ehman, and K. P. McGee. MR Elastography of Human Lung Parenchyma: Technical Development, Theoretical Modeling and In Vivo Validation. *Journal of Magnetic Resonance Imaging*, 33(6):1351–61, June 2011.

[58] T. J. Masaryk, M. T. Modic, J. S. Ross, P. M. Ruggieri, G. A. Laub, G. Lenz, E. M. Haacke, W. R. Selman, M. Wiznitzer, and S. Harik. Intracranial circulation: preliminary clinical results with three-dimensional (volume) MR angiography. *Radiology*, 171(3):793–9, June 1989.

[59] MathWorks. Matlab, 2009.

[60] P. J. McCracken, A. Manduca, J. Felmlee, and R. L. Ehman. Mechanical Transient-Based Magnetic Resonance Elastography. *Magnetic Resonance in Medicine*, 53(3):628–39, 2005.

[61] B. Mokri. The Monro-Kellie hypothesis: Applications in CSF volume depletion. *Neurology*, 56(12):1746–8, June 2001.

[62] M. C. Murphy, J. Huston 3rd, C. R. Jack Jr., K. J. Glaser, A. Manduca, J. P. Felmlee, and R. L. Ehman. Decreased Brain Stiffness in Alzheimer's Disease Determined by Magnetic Resonance Elastography. *Journal of Magnetic Resonance Imaging*, 34(3):494–8, 2011.

[63] R. Muthupillai, D. J. Lomas, P. J. Rossman, J. F. Greenleaf, A. Manduca, and R. L. Ehman. Magnetic Resonance Elastography by Direct Visualization of Propagating Acoustic Strain Waves. *Science*, 269(5232):1854–7, 1995.

[64] J. Ophir, I. Céspedes, H. Ponnekanti, Y. Yazdi, and X. Li. Elastography: A Quantitative Method for Imaging the Elasticity of Biological Tissues. *Ultrasonic Imaging*, 13(2):111–134, 1991.

[65] S. Papazoglou, J. Braun, U. Hamhaber, and I. Sack. Two-dimensional waveform analysis in MR elastography of skeletal muscles. *Physics in Medicine and Biology*, 50(6):1313–25, 2005.

[66] S. Papazoglou, S. Hirsch, J. Braun, and I. Sack. Multifrequency inversion in magnetic resonance elastography. *Physics in Medicine and Biology*, 57(8):2329–46, Apr. 2012.

[67] K. J. Parker, S. R. Huang, R. A. Musulin, R. M. Lerner, and Musulin. Tissue Response to Mechanical Vibrations for "Sonoelastic Imaging". *Ultrasound in Medicine and Biology*, 16(3):241–46, 1990.

[68] A. J. Pattison, I. M. Perreard, J. B. Weaver, and K. D. Paulsen. Poroelastic MRE reconstructions of brain acquired with intrinsic activation. In *Proceedings of the 18th Annual Meeting of ISMRM*, page 3404, Stockholm, 2010.

[69] R. D. Penn and A. Linninger. The Physics of Hydrocephalus. *Pediatric Neurosurgery*, 45(3):161–74, 2009.

[70] P. R. Perriñez, F. E. Kennedy, E. E. W. Van Houten, J. B. Weaver, and K. D. Paulsen. Modeling of Soft Poroelastic Tissue in Time-Harmonic MR Elastography. *IEEE Transactions on Biomedical Engineering*, 56(3):598–608, Mar. 2009.

[71] P. R. Perriñez, F. E. Kennedy, E. E. W. Van Houten, J. B. Weaver, and K. D. Paulsen. Magnetic Resonance Poroelastography: An Algorithm for Estimating the Mechanical Properties of Fluid-Saturated Soft Tissues. *IEEE Transactions on Medical Imaging*, 29(3):746–55, 2010.

[72] P. R. Perriñez, A. J. Pattison, F. E. Kennedy, J. B. Weaver, and K. D. Paulsen. Contrast detection in fluid-saturated media with magnetic resonance poroelastography. *Medical Physics*, 37(7):3518–26, 2010.

[73] D. B. Plewes, I. Betty, S. N. Urchuk, and I. Soutar. Visualizing tissue compliance with MR imaging. *Journal of Magnetic Resonance Imaging*, 5(6):733–8, 1995.

[74] B. P. Poncelet, V. J. Wedeen, R. M. Weisskoff, and M. S. Cohen. Brain Parenchyma Motion: Measurement with Cine Echo-Planar MR Imaging. *Radiology*, 185(3):645–51, 1992.

[75] M. Poustchi-Amin, S. A. Mirowitz, J. B. Brown, R. C. McKinstry, and T. Li. Principles and Applications of Echo-planar Imaging: A Review for the General Radiologist. *Radiographics*, 21(3):767–79, 2001.

[76] T. P. Prevost, A. Balakrishnan, S. Suresh, and S. Socrate. Biomechanics of brain tissue. *Acta Biomaterialia*, 7(1):83–95, Jan. 2011.

[77] S. S. Rengachary and R. G. Ellenbogen. *Principles of Neurosurgery*. Elsevier Mosby, Edinburgh, 2nd edition, 2005.

[78] C. Ripoll, R. Groszmann, G. Garcia-Tsao, N. Grace, A. Burroughs, R. Planas, A. Escorsell, J. C. Garcia-Pagan, R. Makuch, D. Patch, D. S. Matloff, and J. Bosch. Hepatic Venous Pressure Gradient Predicts Clinical Decompensation in Patients With Compensated Cirrhosis. *Gastroenterology*, 133(2):481–8, Aug. 2007.

[79] B. Robert, R. Sinkus, J.-L. Gennisson, and M. Fink. Application of DENSE-MR-elastography to the human heart. *Magnetic Resonance in Medicine*, 62(5):1155–63, Nov. 2009.

[80] A. J. Romano, M. Scheel, S. Hirsch, J. Braun, and I. Sack. In vivo waveguide elastography of white matter tracts in the human brain. *Magnetic Resonance in Medicine*, 68(5):1410–22, Jan. 2012.

[81] P. H. Rossier, A. Bühlmann, and K. Wiesinger. *Physiologie und Pathophysiologie der Atmung*. Springer-Verlag, 1956.

[82] O. Rouvière, R. Souchon, G. Pagnoux, J.-M. Ménager, and J.-Y. Chapelon. Magnetic resonance elastography of the kidneys: feasibility and reproducibility in young healthy adults. *Journal of Magnetic Resonance Imaging*, 34(4):880–6, Oct. 2011.

[83] J. Rump, D. Klatt, J. Braun, C. Warmuth, and I. Sack. Fractional encoding of harmonic motions in MR elastography. *Magnetic Resonance in Medicine*, 57(2):388–95, Feb. 2007.

[84] J. Rump, D. Klatt, S. Papazoglou, U. Hamhaber, J. Braun, and I. Sack. Desynchronized motion encoding in rapid steady-state free precession MR elastography. In *Proceedings of the 14th Annual Meeting of ISMRM*, Seattle, 2006.

[85] R. Rzedzian, P. Mansfield, M. Doyle, D. Guilfoyle, B. Chapman, R. E. Coupland, A. Chrispin, and P. Small. Real-time Nuclear Magnetic Resonance Clinical Imaging in Pediatrics. *Lancet*, 322(8362):1281–2, 1983.

[86] I. Sack, J. Rump, T. Elgeti, A. Samani, and J. Braun. MR elastography of the human heart: noninvasive assessment of myocardial elasticity changes by shear wave amplitude variations. *Magnetic Resonance in Medicine*, 61(3):668–77, Mar. 2009.

[87] I. Sack, K.-J. Streitberger, D. Krefting, F. Paul, and J. Braun. The influence of physiological aging and atrophy on brain viscoelastic properties in humans. *PlosOne*, 6(9):e23451, 2011.

[88] R. F. Schmidt and G. Thews, editors. *Physiologie des Menschen*. Springer-Verlag, 27th edition, 1997.

[89] F. Schmitt, M. K. Stehling, and R. Turner. *Echo-Planar Imaging*. Springer, 1998.

[90] M. Soellinger, A. K. Rutz, S. Kozerke, and P. Boesiger. 3D cine displacement-encoded MRI of pulsatile brain motion. *Magnetic Resonance in Medicine*, 61(1):153–62, Jan. 2009.

[91] S. Stoquart-ElSankari, P. Lehmann, A. Villette, M. Czosnyka, M.-E. Meyer, H. Deramond, and O. Balédent. A phase-contrast MRI study of physiologic cerebral venous flow. *Journal of Cerebral Blood Flow & Metabolism*, 29(6):1208–15, Apr. 2009.

[92] I. Troprès, S. Grimault, A. Vaeth, E. Grillon, C. Julien, J. F. Payen, L. Lamalle, M. Decorps, and M. Décorps. Vessel Size Imaging. *Magnetic Resonance in Medicine*, 45(3):397–408, 2001.

[93] B. Tully and Y. Ventikos. Coupling Poroelasticity and CFD for Cerebrospinal Fluid Hydrodynamics. *IEEE Transactions on Biomedical Engineering*, 56(6):1644–51, 2009.

[94] B. Tully and Y. Ventikos. Cerebral water transport using multiple-network poroelastic theory: application to normal pressure hydrocephalus. *Journal of Fluid Mechanics*, 667:188–215, 2011.

[95] K. Uffmann, C. Abicht, W. Grote, H. H. Quick, and M. E. Ladd. Design of an MR-Compatible Piezoelectric Actuator for MR Elastography. *Concepts in Magnetic Resonance*, 15(4):239–54, 2002.

[96] P. van Dijk. Direct Cardiac NMR Imaging of Heart Wall and Blood Flow Velocity. *Journal of Computer Assisted Tomography*, 8(3):429–36, 1984.

[97] M. S. Vavilala, L. A. Lee, and A. M. Lam. Cerebral blood flow and vascular physiology. *Anesthesiology Clinics of North America*, 20(2):247–64, 2002.

[98] M. E. Wagshul, J. J. Chen, M. R. Egnor, E. J. McCormack, and P. E. Roche. Amplitude and phase of cerebrospinal fluid pulsations: experimental studies and review of the literature. *Journal of Neurosurgery*, 104(5):810–9, May 2006.

[99] M. E. Wagshul, P. K. Eide, and J. R. Madsen. The pulsating brain: A review of experimental and clinical studies of intracranial pulsatility. *Fluids and Barriers of the CNS*, 8(5), Jan. 2011.

[100] J. B. Weaver, A. J. Pattison, M. D. McGarry, I. M. Perreard, J. G. Swienckowski, C. J. Eskey, S. S. Lollis, and K. D. Paulsen. Brain mechanical property measurement using MRE with intrinsic activation. *Physics in Medicine and Biology*, 57(22):7275–87, Oct. 2012.

[101] A. B. Wood. *A textbook of sound*. G. Bell and Sons ltd, London, 1930.

Selbstständigkeitserklärung

Hiermit versichere ich, Sebastian Hirsch, dass ich alle zum Erstellen der Arbeit verwendeten Hilfen und Hilfsmittel angegeben und die Arbeit selbstständig verfasst habe.

Berlin, den _____ Unterschrift: _____

Sebastian Hirsch

Publikationsliste

Theoretical background, experiments and results described in this work were published in the following articles in peer-reviewed journals:

1. S. Hirsch, O. Posnansky, S. Papazoglou, T. Elgeti, J. Braun, and I. Sack. Measurement of vibration-induced volumetric strain in the human lung. *Magnetic Resonance in Medicine*, 69(3):667–74, 2013.

2. S. Hirsch, F. Beyer, J. Guo, S. Papazoglou, H. Tzschätzsch, J. Braun, and I. Sack. Compression-sensitive magnetic resonance elastography. *Physics in Medicine and Biology*, 58(15):5287–99, 2013.

3. S. Hirsch, D. Klatt, F. B. Freimann, M. Scheel, J. Braun, and I. Sack. In vivo measurement of volumetric strain in the human brain induced by arterial pulsation and harmonic waves. *Magnetic Resonance in Medicine*, 70(3):671–83, 2013.

4. S. Hirsch, J. Guo, R. Reiter, S. Papazoglou, T. J. Kroencke, J. Braun, and I. Sack. MR Elastography of the Liver and the Spleen Using a Piezoelectric Driver, Single-Shot Wave-Field Acquisition, and Multifrequency Dual Parameter Reconstruction. *Magnetic Resonance in Medicine*, 71(1):267–77, 2014.

5. S. Hirsch, J. Guo, R. Reiter, E. Schott, R. Somasundaram, J. Braun, I. Sack, T. J. Kroencke, and C. Büning. Towards Compression-Sensitive Magnetic Resonance Elastography of the Liver: Sensitivity of Harmonic Volumetric Strain to Portal Hypertension. *Journal of Magnetic Resonance Imaging*, 39(2):298–306, 2014.

The author also contributed to the following published peer-reviewed articles:

1. T. Elgeti, H. Tzschätzsch, S. Hirsch, D. Krefting, D. Klatt, T. Niendorf, J. Braun, and I. Sack. Vibration-synchronized magnetic resonance imaging for the detection of myocardial elasticity changes. *Magnetic Resonance in Medicine*, 67(4):919-24, 2012.

2. S. Papazoglou, S. Hirsch, J. Braun, and I. Sack. Multifrequency inversion in magnetic resonance elastography. *Physics in Medicine and Biology*, 57(8):2329-46, 2012.

3. O. Posnansky, J. Guo, S. Hirsch, S. Papazoglou, J. Braun, and I. Sack. Fractal network dimension and viscoelastic powerlaw behavior: I. A modeling approach based on a coarse-graining procedure combined with shear oscillatory rheometry. *Physics in Medicine and Biology*, 57(12):4023-40, 2012

4. J. Guo, O. Posnansky, S. Hirsch, M. Scheel, M. Taupitz, J. Braun, and I. Sack. Fractal network dimension and viscoelastic powerlaw behavior: II. An experimental study of structure-mimicking phantoms by magnetic resonance elastography. *Physics in Medicine and Biology*, 57(12):4041-53, 2012.

5. A. J. Romano, M. Scheel, S. Hirsch, J. Braun, and I. Sack. In vivo waveguide elastography of white matter tracts in the human brain. *Magnetic Resonance in Medicine*, 68(5):1410-22, 2012.

6. A. J. Romano, J. Guo, T. Prokscha, T. Meyer, S. Hirsch, J. Braun, I. Sack, and M. Scheel. In vivo waveguide elastography: Effects of neurodegeneration in patients with amyotrophic lateral sclerosis. *Magnetic Resonance in Medicine*, 2013 (in press). DOI: 10.1002/mrm.25067

7. J. Guo, S. Hirsch, A. Fehlner, S. Papazoglou, M. Scheel, J. Braun, and I. Sack. Towards an elastographic atlas of brain anatomy. *PLoS ONE*, 8(8):e71807, 2013.

8. J. Braun, J. Guo, R. Lützkendorf, J. Stadler, S. Papazoglou, S. Hirsch, I. Sack, and J. Bernarding. High-resolution mechanical imaging of the human brain by three-dimensional multifrequency magnetic resonance elastography at 7T. *Neuroimage*, 90:308–14, 2014.

9. T. Prokscha, J. Guo, S. Hirsch, J. Braun, I. Sack, T. Meyer, and M. Scheel. Diffusion Tensor Imaging in Amyotrophic Lateral Sclerosis-Increased Sensitivity with Optimized Region-of-Interest Delineation. *Clinical Neuroradiolgy*, 24(1):37-42, 2014.

Some topics from or related to this work were presented at international conferences, either as a talk (T) or a poster (P):

1. S. Hirsch, D. Klatt, S. Papazoglou, K.-J. Streitberger, J. Braun, and I. Sack. Cerebral MR elastography for measuring poroelastic properties of the brain. *Proceedings of the 19th Scientific Meeting, International Society for Magnetic Resonance in Medicine*, 42, Montréal, Canada, 2011 (T).

2. S. Hirsch, T. Elgeti, D. Klatt, J. Braun, and I. Sack. Single-Shot Cardiac MR Elastography. *Proceedings of the 19th Scientific Meeting, International Society for Magnetic Resonance in Medicine*, 3495, Montréal, Canada, 2011 (P).

3. S. Hirsch, T. J. Kroencke, J. Guo, R. Reiter, S. Papazoglou, I. Sack, and J. Braun. In Vivo Measurement of Volumetric Strain for the Assessment of Intrahepatic Pressure Alterations. *Proceedings of the 11th International Tissue Elasticity Conference*, 47, Deauville, France, 2012 (T).

4. S. Hirsch, F. Beyer, J. Guo, S. Papazoglou, H. Tzschätzsch, A. Fehlner, I. Sack, J. Braun. Compression Sensitive Magnetic Resonance Elastography. *Proceedings of the 11th International Tissue Elasticity Conference*, 48, Deauville, France, 2012 (T).

5. S. Hirsch, F. Beyer, S. Papazoglou, J. Guo, J. Braun, and I. Sack. Magnetic Resonance Elastography for the Measurement of the Bulk Modulus in Compressible Materials. *Proceedings of the 21st Scientific Meeting, International Society for Magnetic Resonance in Medicine*, 2440, Salt Lake City, USA, 2013 (P).

6. S. Hirsch, T. J. Kroencke, J. Guo, R. Reiter, S. Papazoglou, P. Asbach, J. Braun, I. Sack. Sensitivity of Intrahepatic Volumetric Strain Measured by MR Elastography to the Alteration of Portal Pressure in Patients with Transjugular Intrahepatic Portosystemic Shunt. *Proceedings of the 21st Scientific Meeting, International Society for Magnetic Resonance in Medicine*, 4076, Salt Lake City, USA, 2013 (P).

Berlin, den _____ Unterschrift: _____

Sebastian Hirsch